Inaugural dissertation

for

obtaining the doctoral degree

of the

Combined Faculty of Mathematics, Engineering and Natural Sciences

of the

Ruprecht - Karls - University

Heidelberg

Presented by

Kim Hoa Ho, M.Sc.

born in: Ho Chi Minh City, Vietnam

Oral examination: 12.06.2024

The development and tumorigenesis of choroid plexus

Referee: Prof. Dr. rer. nat. Gudrun Rappold

Dr. Annarita Patrizi

Contents

Declaration

My Doctoral research was conducted from June 2019 to June 2024 under the supervision of Dr. Annarita Patrizi in the Division of Neuronal Signaling and Morphogenesis at the German Cancer Research Center (DKFZ) in Heidelberg, Germany.

The majority of data from the cilia project has been published in the preprint:

Kim Hoa Ho, Valentina Scarpetta, Chiara Salio, et al. 2023. "Intrinsic microtubule destabilization of multiciliated choroid plexus epithelial cells during postnatal lifetime." *bioRxiv* 2023.01.10.523428; doi: https://doi.org/10.1101/2023.01.10.523428

and the publication:

Kim Hoa Ho, Adrien Candat, Valentina Scarpetta, et al. 2023. "Choroid plexuses carry nodal-like cilia that undergo axoneme regression from early adult stage." *Developmental Cell* 58 (23): 2641-2651.e6. https://doi.org/10.1016/j.devcel.2023.10.003.

Data from the tumor project has been submitted and currently under revision for publication.

List of figures

Figure ..... **Page**

List of tables

Table ..... Page

Abbreviation

aCPP	Atypical choroid plexus papilloma
BBB	Blood-brain barrier
BCSFB	Blood-cerebrospinal-fluid barrier
BrdU	Bromodeoxyuridine
CADD	Combined Annotation Dependent Depletion
cDNA	Complementary DNA
ChP	Choroid plexus
CNV	Copy number variation
CPC	Choroid plexus carcinoma
CPP	Choroid plexus papilloma
Cre	Cre recombinase enzyme
CreER	Cre recombinase fused with tamoxifen-responsive estrogen receptor (ERT2)
CRISPR	Clustered Regularly Interspaced Short Palindromic Repeats
CSF	Cerebrospinal fluid
Ctrl	Control
dChP	Diencephalic choroid plexus
DEG	Differentially expressed gene
DMEM	Dulbecco's Modified Eagle Medium
DMSO	Dimethyl sulfoxide
***E** (followed by a number)*	Embryonic day
EdU	5-ethynyl-2 deoxyuridine
EGFP	Enhanced Green Fluorescent Protein
FACS	Fluorescence-Activated Cell Sorting
FBS	Fetal Bovine Serum
FFPE	Formalin-Fixed Paraffin-Embedded
GFP	Green Fluorescent Protein
GO	Gene Ontology
GT	Geltrex
H&E	Hematoxylin and eosin
hChP	Hindbrain choroid plexus

hiPSC	Human induced pluripotent stem cell
IF	Immunofluorescence
IFN	Interferon
IHC	Immunohistochemistry
IHF	Immunohistofluorescence
IL	Interleukin
Indel	Insertion-Deletion
i.p.	Intraperitoneal
IPA	Ingenuity Pathway Analysis
kb	Kilobase
kDa	Kilodalton
KO	Knock-out
LOEUF	Loss-of-function observed over expected upper bound fraction
LoF	Loss of function
mcc	Multi-ciliated cell
mcd	Multi-ciliated cell at disengagement phase
MNP	Molecular neuropathology
MTT	3-(4,5-dimethylthiazol-2-yl)-2,5-diphenyltetrazolium bromide
NEAA	Non-essential Amino Acid
***P** (followed by a number)*	Postnatal day
PBS	Phosphate-buffered saline
PCR	Polymerase chain reaction
PFA	Paraformaldehyde
PVDF	Polyvinylidene fluoride
RT	Room temperature
RT-qPCR	Quantitative reverse transcription polymerase chain reaction
sc	Single cilium
SEM	Standard error of the mean
sgRNA	Single guide RNA
snRNA	Single-nucleus RNA
SNP	Single-nucleotide polymorphism

SNV	Single-nucleotide variant
ssTEM	Serial section transmission electron microscopy
SV	Structural variant
tChP	Telencephalic choroid plexus
TEM	Transmission electron microscopy
V-SVZ	Ventricular-subventricular zone
WB	Western Blot
WGS	Whole-genome sequencing
WT	Wild type

Abstract

The choroid plexus (ChP) is a specialized secretory tissue located within all brain ventricles, playing diverse crucial roles in brain development, homeostasis, and intercommunication between the brain and the body. ChP is also implicated in various neuropathologies like Alzheimer's, Huntington's diseases, and multiple sclerosis, etc. Consequently, a more profound understanding of both the normal development and the disruption of ChP functions could be greatly advantageous in addressing neurological and extra-cranial diseases. Despite growing research interest, the ChP remains underexplored, hindering advancements in understanding and treating associated disorders. One of the pathological conditions of the ChP is choroid plexus tumors (CPT), which are rare tumors that tend to occur with increased frequency and malignancy in young patients. The aggressive type of CPT is linked to p53 mutations in around 50% cases; nevertheless, common driver mutations for all CPT forms remain unidentified. The research and treatment of CPT are challenged by the absence of valid experimental models, insights into the disease mechanism, and consequently, candidates for targeted therapy. Limited literature suggests a potential link between CPT and ChP cilia, but apart from the fact that ChP epithelial cells are multiciliated, little is known regarding the formation and maintenance of these cilia during normal development, impeding efforts to establish a correlation between cilia and CPT. In my PhD research, I led and conducted two main projects: (i) investigating the tumorigenesis and *in vitro* modeling of CPT, and (ii) characterizing the biogenesis and maintenance of ChP cilia, aiming to fill crucial gaps in our understanding of these processes.

To investigate CPT tumorigenesis, I first analyzed genomic and transcriptomic data from CPT patients and discovered that large-scale chromosomal instability events of the CPT genomes cause a constitutive activation of Wnt/β-catenin signaling in human CPTs. These data were validated in CPT patient samples using molecular and histopathological methods. Next, I inhibited Wnt/β-catenin signaling pharmacologically and showed that CPT-derived cells depend on autocrine Wnt/β-catenin for survival. Additionally, constitutive Wnt/β-catenin pathway activation, either through knock-out of the negative regulator APC or overexpression of the ligand WNT3A, induced tumorigenic properties in 2D *in vitro* models of choroid plexus cells. To enhance tumor modeling using human cells and replicate its 3D architecture and interactions with other cell types, I used ChP

organoids derived from human induced pluripotent stem cells (hiPSCs). Systematic hyper-activation of Wnt/β-catenin pathway in ChP organoids led to reduced differentiation of choroid plexus epithelial cells, rendering them increasingly susceptible to tumor development. Remarkably, CRISPR-Cas9 knock-out of APC in choroid plexus organoids was sufficient to induce oncogenic transformation, resulting in neoplasm with features resembling supratentorial pediatric high-risk choroid plexus tumors. In summary, this project identifies Wnt/β-catenin signaling as a critical driver of CPT oncogenesis and provides the first 3D *in vitro* model for future pathological and therapeutic studies of CPT.

To study the ChP cilia, I used a combination of super-resolution-microscopy approaches and mouse genetics, tracking cilia progression from embryogenesis when the ChP first emerges until senescence. I was able to provide fundamental understanding on ChP ciliogenesis, showing that their cilia are built on a gradient of events which are spatio-temporally regulated. ChP cilia appear prenatally since early tissue morphogenesis, commencing with atypical centriole amplification and culminating in the assembly of numerous nodal-like 9+0 cilia displaying both primary and motile characteristics. Unexpectedly, I found that adult ChP cilia undergo axoneme resorption through a tubulin destabilization process, which is partially controlled by the microtubule-severing enzyme spastin and could be mitigated by polyglutamylation levels. I also demonstrated that human ChP cilia experience the same process, suggesting a conserved ciliary resorption mechanism in mammals.

The results of the two projects not only contribute to the progress in studies on each topic independently but also provide the foundation for integrating them together, aiming to provide a more comprehensive picture of ChP cilia, its tumor, and the overall biology of the ChP.

Zusammenfassung

Der Plexus choroideus (ChP) ist ein spezialisiertes Sekretionsgewebe, das sich in allen Hirnventrikeln befindet und verschiedene entscheidende Rollen bei der Entwicklung des Gehirns, der Homöostase und der Kommunikation zwischen dem Gehirn und dem Körper spielt. ChP ist auch an verschiedenen Neuropathologien wie Alzheimer, Chorea Huntington und Multipler Sklerose usw. beteiligt. Folglich könnte ein tieferes Verständnis sowohl der normalen Entwicklung als auch der Störung der ChP-Funktionen bei der Behandlung anderer neurologischer und außerkranialer Krankheiten von großem Vorteil sein. Trotz des wachsenden Forschungsinteresses ist der ChP nach wie vor wenig erforscht, was Fortschritte beim Verständnis und bei der Behandlung der damit verbundenen Erkrankungen behindert. Einer der pathologischen Zustände des ChP sind Aderhautplexustumore (CPT), seltene Tumoren, die bei jungen Patienten besonders häufig und bösartig auftreten. Die aggressive Form der CPT ist in etwa 50 % der Fälle mit p53-Mutationen verbunden; allerdings sind die gemeinsamen Treibermutationen für alle CPT-Formen noch nicht identifiziert. Die Erforschung und Behandlung der CPT wird dadurch erschwert, dass es keine validen experimentellen Modelle, keine Erkenntnisse über den Krankheitsmechanismus und folglich auch keine Kandidaten für eine gezielte Therapie gibt. Die begrenzte Literatur deutet auf einen möglichen Zusammenhang zwischen CPT und ChP-Zilien hin, aber abgesehen von der Tatsache, dass ChP-Epithelzellen vielzilliert sind, ist wenig über die Bildung und Erhaltung dieser Zilien während der normalen Entwicklung bekannt, was die Bemühungen um einen Zusammenhang zwischen Zilien und CPT erschwert. Im Rahmen meiner Doktorarbeit habe ich zwei Hauptprojekte geleitet und durchgeführt: (i) Untersuchung der Tumorigenese und In-vitro-Modellierung von CPT und (ii) Charakterisierung der Biogenese und Erhaltung von ChP-Zilien mit dem Ziel, entscheidende Lücken in unserem Verständnis dieser Prozesse zu schließen.

Zur Untersuchung der CPT-Tumorgenese analysierte ich zunächst genomische und transkriptomische Daten von CPT-Patienten und entdeckte, dass groß angelegte chromosomale Instabilitätsereignisse der CPT-Genome eine konstitutive Aktivierung der Wnt/β-Catenin-Signalgebung in menschlichen CPTs verursachen. Diese Daten wurden in CPT-Patientenproben mit molekularen und histopathologischen Methoden validiert. Als Nächstes habe ich die Wnt/β-Catenin-Signalübertragung pharmakologisch gehemmt und

gezeigt, dass von CPT abgeleitete Zellen zum Überleben auf autokrines Wnt/β-Catenin angewiesen sind. Darüber hinaus induzierte die konstitutive Aktivierung des Wnt/β-Catenin-Signalwegs, entweder durch Knock-out des negativen Reglers APC oder durch Überexpression des Liganden WNT3A, tumorigene Eigenschaften in 2D-in-vitro-Modellen von Aderhautplexuszellen. Um die Tumormodellierung mit menschlichen Zellen zu verbessern und die 3D-Architektur und die Interaktionen mit anderen Zelltypen nachzubilden, habe ich ChP-Organoide verwendet, die aus menschlichen induzierten pluripotenten Stammzellen (hiPSCs) stammen. Die systematische Hyperaktivierung des Wnt/β-Catenin-Signalwegs in ChP-Organoiden führte zu einer verminderten Differenzierung der Epithelzellen des Plexus choroideus, was sie zunehmend anfällig für die Tumorentwicklung machte. Bemerkenswerterweise reichte der CRISPR-Cas9-Knock-out von APC in Aderhautplexus-Organoiden aus, um eine onkogene Transformation zu induzieren, die zu einem Neoplasma mit Merkmalen führte, die supratentoriellen pädiatrischen Aderhautplexus-Hochrisikotumoren ähneln. Zusammenfassend lässt sich sagen, dass dieses Projekt den Wnt/β-Catenin-Signalweg als kritischen Treiber der CPT-Onkogenese identifiziert und das erste 3D-In-vitro-Modell für zukünftige pathologische und therapeutische Studien von CPT bereitstellt.

Um die ChP-Zilien zu untersuchen, habe ich eine Kombination aus Super-Resolution-Mikroskopie und Mausgenetik verwendet und die Entwicklung der Zilien von der Embryogenese, wenn die ChP zum ersten Mal auftauchen, bis zur Seneszenz verfolgt. Ich konnte ein grundlegendes Verständnis der Zilienbildung bei ChP gewinnen und zeigen, dass ihre Zilien auf einem Gradienten von Ereignissen aufbauen, die räumlich und zeitlich reguliert sind. ChP-Zilien entstehen pränatal seit der frühen Gewebemorphogenese, beginnend mit einer atypischen Zentriolenamplifikation und gipfelnd in der Bildung zahlreicher knotenartiger 9+0-Zilien, die sowohl primäre als auch bewegliche Eigenschaften aufweisen. Unerwartet fand ich heraus, dass adulte ChP-Zilien durch einen Tubulin-Destabilisierungsprozess eine Axonem-Resorption erfahren, die teilweise durch das Mikrotubuli-abspaltende Enzym Spastin kontrolliert wird und durch den Polyglutamylierungsgrad abgeschwächt werden kann. Ich habe auch gezeigt, dass menschliche ChP-Zilien denselben Prozess durchlaufen, was auf einen konservierten ziliären Resorptionsmechanismus bei Säugetieren hindeutet.

Die Ergebnisse der beiden Projekte tragen nicht nur zu den Fortschritten bei, die in den Studien zu den einzelnen Themen erzielt wurden, sondern bilden auch die Grundlage für die Integration der beiden Projekte, um ein umfassenderes Bild der ChP-Zilien, ihres Tumors und der Gesamtbiologie des ChP zu erhalten.

1. Introduction

1.1. Choroid plexus

1.1.1. Choroid plexus morphology and composition

Choroid plexus (ChP) was initially described by Galen of Pergamon around 300 BC as a highly vascularized tissue situated within the brain ventricles; however, it was not until 1664 that Thomas Willis suggested its role in secreting cerebrospinal fluid (CSF) into brain ventricles [1]. Historically, the term "Choroid plexus" (from Latin: chorion–delicate, plexus–knot) was defined by its vasculature. The ChP in lateral, third and fourth ventricles are also called telencephalic (tChP), diencephalic (dChP) and hindbrain (hChP) choroid plexus, respectively (Fig. 1). Specialized ChP epithelial cells also forms the blood-CSF barrier (BCSFB), which is often considered a more permeable counterpart to the blood-brain barrier (BBB). ChP presence in the brain has been reported in multiple species including human, rabbit, sheep, mouse, rat, *Monodelphis domestica* (South American gray short-tailed opossum), chick, frog, zebrafish, lamprey and elasmobranchs (sharks, rays, skates, and sawfish) [2], [3], showing that ChP is an evolutionarily conserved structure. Nevertheless, some other species like amphioxus and hagfish do not have ChP [2].

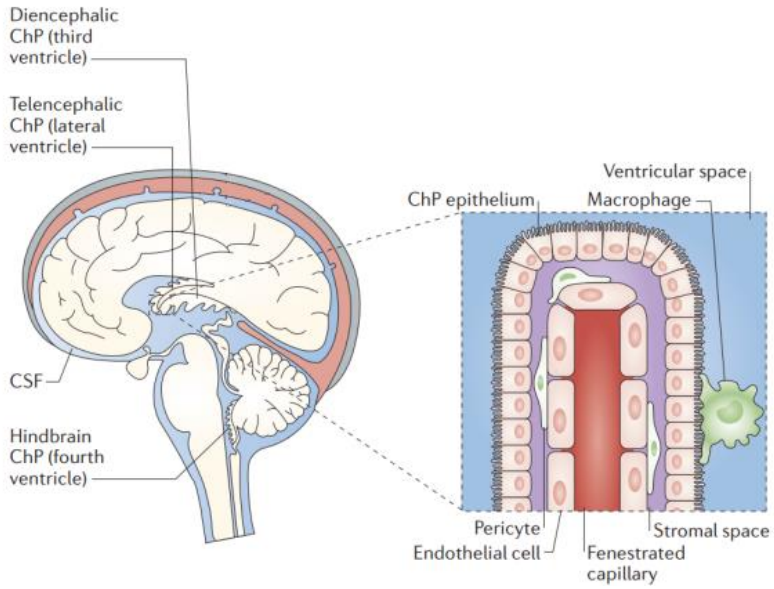

Figure 1: Gross morphology of the mammalian brain and the choroid plexuses in four ventricles *(modified from Lun et al. 2015* [4]*)*

The whole ChP structure is folded and protrudes into the fluid-filled ventricles (Fig. 1). ChP is comprised of multiple cell types, of which 61% - 69% is epithelial cells [5]; it also contains mesenchymal (mural and fibroblast), endothelial, immune, neuronal and glial cells [6] (Fig. 2). The gross structure of the four ChPs are rather similar: a monolayer of cuboidal epithelial cells joined by tight junctions at the apical side, above the adherens junctions and desmosomes [7], encasing mesenchymal tissue with fenestrated blood vessels [2]. The tight junctions play a fundamental role in regulating BCSFB permeability and integrity. The apical surface is considerably increased by the presence of microvilli [2] and it also features a tight cluster of short multiple cilia [8] (Fig. 2). Despite similar composition and organization of ChPs across ventricles, their epithelial and fibroblast cells displayed differential gene expression profiles among each other and across the lifespan [4][6].

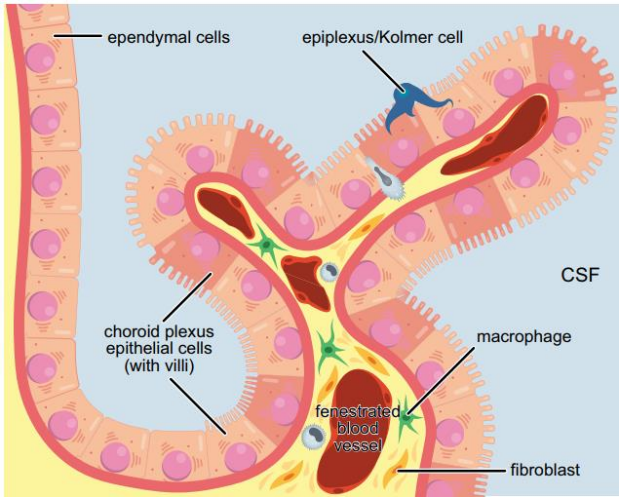

Figure 2: The composition of choroid plexus tissue *(adapted from Saunders et al. 2022)*

1.1.2. Choroid plexus development

Studies from murine and avian systems showed that ChP cell fate was determined since early development [4]. In mouse brain, ChP specification takes place after the closure of the neural tube, between embryonic day 8.5 (E8.5) and E9.5 [9], which is 2-3 days before anatomical appearance of the ChP [9], [10]. The ChP epithelium is derived from neuroepithelial cells of the roof plate – the multipotent stem cells of the nervous system, while stromal cells are suggested to come from head mesenchymal cells [10], [11]. In human, the hChP appears at around gestation week 6th, tChP at week 7th and dChP at week 8th [12]. Similarly, in mouse, hChP is the first to develop with its morphological appearance starting from E10.5 – E12.5, 2-3 days after fate specification; tChP appears

around 24 hours later [9]. Rodent ChP is constructed on a treadmill of proliferating cells entering the ChP at the region proximal to the brain parenchyma. Most tChP epithelial cells are generated at E10.5 and evenly distributed along the tissue. From E14.5, proliferating cells of tChP are mainly present within the first 0.25 mm tissue attached to the ventricle wall; most mature ChP cells are postmitotic with very few remains proliferative after birth [8], [13].

The ChP epithelium derives from proliferative pseudostratified progenitor domains along the roof plate neuroepithelium [11]. Obvious candidates to control the development of the ChP epithelial cells are signaling molecules secreted by the cortical hems (the signaling center located adjacent to tChP with organizer potential), including Bone morphogenetic proteins (BMPs) and WNT ligands [14], [15], [16]. Specifically, tChP is derived from the BMP/WNT/MSX-rich cortical hem while hChP arises from WNT1/GDF7/LMX1A-positive upper and lower rhombic lip [17], [18] (Fig. 3). All ChP progenitor domains, however, share in their expression profiles high levels of Rspo2-3 genes encoding R-spondins – enhancers of the Wnt/β-catenin signaling [6].

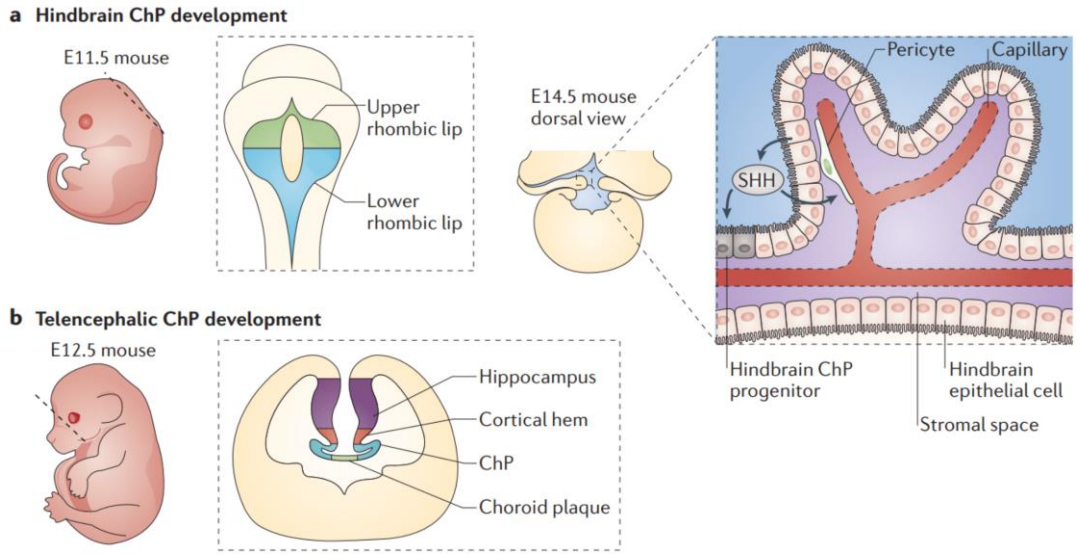

Figure 3: Progenitor domains of the hChP and tChP *(modified from Lun et al. 2015*[4]*)*

Recent studies have shown that WNT5A has important roles in regulating ChP epithelial morphogenesis in all ventricles. In mice of systemic knock-out or overexpression of WNT5A, ChP significantly reduces its size and complexity and fail to expand into the ventricles [19], [20]. In a study focusing on the tChP, *Lmx1a-Cre* was used to excise exon 3 of β-catenin gene, resulting in the stabilized expression of this protein and inducing constitutive activation of the Wnt/β-catenin pathway. This led to the loss of ChP epithelial

identity and a transformation into neuronal identity in both mouse and organoid models [21]. These studies demonstrate the important role of Wnt signaling in the development and morphogenesis of ChP.

1.1.3. The functions of choroid plexus – cerebrospinal fluid system

One crucial function of the ChP is to produce CSF. In adult human, the CSF volume in the brain is 140 – 160 ml and is replaced about 3-4 times per day, which makes a total volume of CSF produced each day averagely 600 ml [22], [23], [24]. Around 80% of this CSF volume is secreted by the ChP [25]. CSF composition is relatively similar to plasma; however, it is not an ultrafiltrate of the plasma, but rather actively secreted and regulated by the ChP [26], [27]. Traditionally, CSF is known to provide mechanical support for the brain (the brain's weight is reduced >60% as it "floats" in CSF); to serve as a "sink" for the dilution and disposal of brain's waste from metabolism and synaptic activities; and to be an important route for nutrition distribution in the central nervous system (CNS) [26].

The ChP-CSF system is also an important component in regulating adult neurogenesis in both the ventricular-subventricular zone (V-SVZ) and the sub-granular zone of the hippocampus [4]. Both embryonic and adult CSF has been shown to support adult neural stem cells thanks, in part, to the combination of factors distributed by the CSF, including interleukin-1β (IL-1β) [28], neurotrophin 3 (NT3) [29] and SLIT [30]. In experiments of mouse behaviors, blockade of type I interferon (IFN-I) signaling in the aged brain partially restore cognitive function and hippocampal neurogenesis, re-establish a ChP profile that is IFN-II-dependent and lost in aging [31]. Silva-Vargas et al. [32] showed that tChP is a key component of the adult V-SVZ (ventricular-subventricular zone) niche and that functional effects of tChP secretome change with aging. Secreted factors from the tChP maintains V-SVZ stem cell quiescence and regulates multiple aspects of adult stem cells and their progenies, affecting these cells regardless of whether they are in direct contact with CSF or not. Specifically, tChP secretome promotes the recruitment of quiescent and activated neural stem cells, mainly through the effect of BMP5 and IGF, which are particularly enriched in young rather than old tChP.

ChP-CSF system also regulates critical periods – the time window in early postnatal stage when the development and maturation of the brain is heavily influenced by environmental experience. The homeodomain transcription factor OTX2 is synthesized

and secreted by the ChP and speculated to be distributed throughout the brain by CSF. It is taken up by parvalbumin-positive GABA-ergic interneurons in the forebrain and regulates interneuron maturation, therefore determining the timing of critical period to establish visual acuity [33]. Additionally, CSF serotonin level is reduced at birth, which can be accelerated in pre-term birth, has an important role in sensory map formation [34].

CSF has been shown to contain biomarkers of circadian rhythmicity and plays critical roles in relaying output of diurnal clocks to brain areas of target. Specifically, CSF contains circadian cues for drowsiness [35] and satiety [36], as well as factors released from the hypothalamus to mediate circadian rhythmicity of locomotion [37]. Additionally, ChP expresses functional odorant and taste receptors, which aid in monitoring the composition of CSF, blood and interstitial fluid, subsequently control brain fluid composition and safeguard the central nervous system [38], [39].

ChP surface area, which takes into account the microvilli, provides a large surface for ion and compound transports across the ChP. Particularly, the total apical surface of all ChPs in 30-day-old rat is around 75 cm^2, which is around up to 50% surface area of all cerebral capillaries [40]. Ion transportation has a major role in CSF secretion: the osmotic gradient of Na^+, K^+, Cl^-, HCO_3^- determines the transport of H_2O [41]. As far as we know, the apical membrane contains more transporters compared to the basolateral membrane [39]. The main ion transporters are listed in Table 1:

Table 1: Ion transporters on the ChP [39]

Location	Type	Transporter name
Apical membrane	K^+ channel	Kv1.3, Kv1.1, Kir7.1
	Na^+-HCO_3^- cotransporter	NBCe2
	Na^+-K^+-$2Cl^-$ cotransporter	NKCC1
	K^+-Cl^- cotransporter	KCC4
	Na^+/H^+ exchanger	NHE1
	Cl^- channel	VRAC and Clir
	Na^+-K^+-ATPase	-
	Aquaporin	AQP1
Basolateral membrane	K^+-Cl^- cotransporter	KCC3
	Na^+-HCO_3^- cotransporters	NBCn1, NCBE/ NBCn2
	Cl^-/HCO_3^- exchanger	AE2
	Glucose transporter-1	GLUT1
	Aquaporin	AQP1

NKCC1 is located at the apical membrane of ChP epithelia and could co-transport water in an ion-mediated manner. NKCC1 has been shown to secrete as much as 50% of ChP CSF [27] and mediate CSF clearance to reduce CSF K^+ concentration at perinatal stage [42] and post-hemorrhagic hydrocephalus [43]. AQP1 is expressed on both sides of ChP epithelial cells, but its level was much higher on the apical surface [44] and it is responsible for around 20% – 25% CSF production [45].

Selective transport of molecules across the ChP by specific transmembrane proteins is essential for the exchanges of metabolites and xenobiotics between CSF and blood. These transporters are mainly comprised of ATP-binding cassette (ABC) transporter and solute carrier (SLC) super-families [39]. There are two main types of ChP ABCs: multidrug resistance-related proteins (MRPs) and multidrug transporter P-glycoprotein (PgP). MRPs transport metabolic waste and harmful substance out of the CNS [46]. PgP, together with organic anion transporting polypeptide (Oatp), keeps the concentration of certain drugs in CSF at a low subtherapeutic level [39]. SLC transporters also have protective roles to BCSFB: SLC29A4 removes serotonin, dopamine and histamine from CSF, terminating neurotransmitter signaling [41].

In summary, the ChP-CSF is a sophisticated system that plays multipe important roles in the normal development and homeostasis of the CNS, suggesting its involvement in a wide range of pathological conditions.

1.1.4. The roles of choroid plexus – cerebrospinal fluid system in neuropathology

Recent experimental and clinical studies have revealed the critical role of the ChP in the pathophysiology of numerous CNS diseases such as infection, neurodegenerative disorders, stroke and autoimmnune diseases. Many pathogens (viruses, bacteria, fungi and parasites) can access the CNS via different routes such as infection into the cells, paracellular transport through a loosened tight junction or exploitation of infected phagocytic host cells [39]. Pathogen infection through the BCSFB is typically followed by chemokine secretion, leading to immune cell trafficking across the ChP epithelium and ultimately CNS inflammation [47].

ChP also responses to hemorrhagic stroke by inflammatory reactions: the degradation of blood components (heme, fibrinogen, intracellular structures) creates damage-

associated molecular patterns (DAMPs), which then triggers inflammation. A type of hemorrhagic stroke - subarachnoid hemorrhage - also causes an increase macrophage quantity on ChP apical surface [48]. The enhanced inflammation alters tight junction proteins and subsequently lead to hypersecretion of CSF [49], [50], [51].

ChP responses to ischemia with functional impairment, apoptosis, and/or necrosis of its epithelial cells, varying according to the severity of the underlying ischemic event [39]. Ischemic injury to the ChP results in heightened permeability of the BCSFB to inulin, demonstrating the impact of ChP ischemic injury on BCSFB function [52]. After ischemia, ChP epithelial cells can produce neurotoxic and inflammatory molecules, which cause neuronal damage, especially in the hippocampus [53]. On the other hand, transplanted ChP could induce the secretion of growth factors, providing neuroprotective effects [54].

Mounting evidence indicates that the ChP undergoes morphological and molecular changes that contribute to the progression and pathophysiology of neurodegenerative disorders. In Alzheimer's disease, the presence of β-amyloid is associated with immune response, leading to capillary damage and interstitial fibrosis [55]. The expression of interferons in ChP is altered in Alzheimer's disease model, affecting the recruitment of immune cells to the CNS [56]. It is also proven that β-amyloid induces the secretion of pro-inflammatory cytokines and matrix metalloproteinases, down-regulating the expressions of tight junction proteins and leading to BCSFB alteration [57]. ChP is also involved in the clearance of β-amyloid from CSF [58]. Recent translational studies have shown that Alzheimer's disease treatment could be assisted with viral vectors targeting β-amyloid synthesis in ChP [39]; or β-amyloid could be degraded with ChP transplantation [59].

Multiple sclerosis is characterized by white matter's inflammatory lesions, accompanied by an increased presence of lymphocytes and macrophages. ChP is the site where lymphocytes enter CSF, followed by increased IgG production. T-cells regulate the trafficking of immune cells across the BCSFB via the production of IFN-γ, cytokines and chemokines [39]. The increase of microRNA-155 and -326 in multiple sclerosis contributes to the loss of tight junction proteins, which leads to the disruption of BCSFB and subsequent penetrance of immune cells and autoantibodies into the CNS [60].

1.2. Choroid plexus tumors

Choroid plexus tumors (CPTs) are rare intracranial neoplasms, which account for up to 20% of pediatric cancers occurring in <1-year-old children [61]. According to the World Health Organization (WHO) classification, CPTs are categorized as choroid plexus papilloma (CPP), atypical choroid plexus papilloma (aCPP) and choroid plexus carcinoma (CPC)[62]. In histopathological examination, CPP remains the ChP papillary structure comprising of fibrovascular core surrounded by a monolayer of cuboidal to columnar epithelium; cells' nuclei are basal, monomorphic, round or oval, while the cytoplasm is abundant and eosinophilic; mitotic activity is rare and there is no necrosis or invasion; CPP differs from normal ChP at cell crowding and elongation in the papilloma. When CPP presents with a few limited malignant features, the tumor is diagnosed as aCPP. As the aggressive type, CPC is characterized with a blurred or lost papillary architecture of ChP, increased cell density, mitotic figures, nuclear pleomorphism and necrosis (Fig. 4) [63].

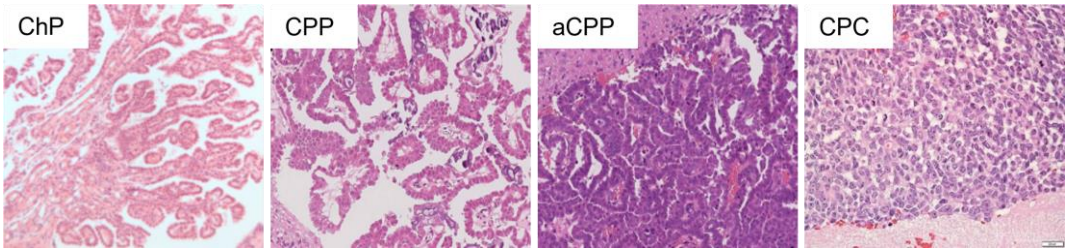

Figure 4: Histological images of normal ChP, CPP, aCPP and CPC *(Images are from The International Society for Paediatric Neurosurgery*[64]*)*

CPP occurs in both children and adults with rather favorable outcomes, although risks of recurrence and dissemination cannot be entirely excluded. CPC occurs primarily in young children and are aggressive with a dissemination rate of 12-30% and 5-year survival rate of 26-73% [65], [66]. While complete tumor resection proves effective in some cases, patients' outcome can be negatively affected by perioperative morbidity due to young age, the tumor's intraventricular location and impairment of CSF drainage [66]. Due to limited understanding of its pathogenesis, no CPT-specific chemotherapeutic drugs are currently available. Likewise, only limited clinical studies have been carried out to develop a treatment paradigm selective for CPT. CPT-SIOP-2000 – the largest and only randomized trial for CPT to date [67] – achieved certain success in developing an irradiation and chemotherapy guideline for CPT generally, but nearly 50% of CPC

patients still passed away within 5 years despite intensive treatment. Therefore, a more specific and effective target for CPT treatment is still in high demand.

CPT genomes are characterized by large and frequent chromosomal instability events [68], [69], [70], [71]. Specifically, CPPs are mainly described as hyperdiploid [68], [71], whereas CPCs are a mix of hyper-, hypodiploid and acquired uniparental disomy [69], [71]. Copy-number analyses also showed increased frequency of chromosome-wide gain in CPP while both chromosomal gain and loss can occur in CPC [71], [72]. It is still unknown whether these chromosomal instability events are the driver of CPT tumorigenesis, or they are the consequences of another unidentified upstream mechanism, and how these events contribute to the aggressiveness of each type of tumors. On the other hand, CPC is generally associated with Li-Fraumeni syndrome (LFS) – a cancer predisposing condition caused by pathogenic/deleterious germline mutations in the TP53 tumor suppressor gene caused by germline mutations on TP53. Targeted DNA sequencing of CPCs have detected both somatic and germline TP53 mutations in 50% and 44.4% of patients, respectively [73]. In contrast, TP53 mutations were absent in most CPP and aCPP [72]. However, TERT promoter mutations were identified in 18% CPT adult cases, mainly including CPP and aCPP [72]. Therefore, most CPTs, both in children and adult, lack recurrent genetic driver mutations.

Recently, *in vivo* studies demonstrated that the ablation of popular well-known tumor suppressor genes or sustained expression of proto-oncogene is sufficient to induce CPTs in mice. Specifically, Tong *et al.* [74] electroporated Cre recombinase into the ventricles of E12.5 embryos to knock-out *Tp53, Rb, Pten*, generating CPC and identifying concurrently gained oncogenes in human and mouse, including *TAF12, NFYC, RAD54L*. On the other hand, sustained expression of *Notch1* by *Math1-Cre* or *Lmx1a-Cre* in mice lead to the development of CPP, driven by abnormal activation of Notch and Sonic Hedgehog (SHH) signaling [75]. In addition, multiple studies inducing *c-Myc* overexpression/stabilization alone or in combination with *Tp53* knock-out also lead to CPTs in mice. Specifically, expression of stabilized *c-Myc* and deletion of *Tp53* driven by the tamoxifen-inducible *Otx2-CreER* can lead to CPC within 150 days after birth [76]. Over-expression of *c-Myc* alone driven my *Nestin-Cre* lead to either CPP [77] or CPC [78], speculated to depend on the level of *c-Myc* over-expression. Similarly, under the control of *Atoh1-Cre, hGFAP-Cre* or *Blbp-Cre*, *c-Myc* over-expression alone causes CPP, and when

coupled with *Tp53* knock-out causes CPC [79]. Although these mouse models all developed tumors at the ChP, they bear limited resemblance to human tumors in genetic [74] and transcriptomic [77] profiles; they also develop tumors in later stage of life of 13 – 28 weeks [77], [79], which is particularly late for models of CPC. It is still undetermined which of these models recapitulate most faithfully the biology of human CPT. Therefore, **a widely accepted mechanism driving human CPT initiation and pathogenesis remains largely unexplored, which is the main focus of my PhD research**.

1.3. Multiciliated cells of the choroid plexus

1.3.1. Introduction to cilia and ciliogenesis of multiciliated cells

Most vertebrate cells typically carry either a singular non-motile (referred to as 'primary') cilium or multiple cilia. Specialized cells also carry cilia that are actively motile, such as cilia of the embryonic node, trachea, ependyma and sperm. While immotile cilia play a crucial role in transducing signals from the surrounding environment or neighboring cells, motile cilia are responsible for propelling cells (such as sperm cells) or facilitating the movement of extracellular fluids (for instance, in clearing mucus and debris from the lung) [80].

Structurally, cilium is an organelle typically consisting of microtubule-rich structures of a basal body located inside the cell, and an axoneme protruding from cell apical membrane. The basal body is comprised of nine triplet microtubules. The cilia shaft, known as the axoneme, is primarily characterized by doublet microtubules that extends from the basal body. Furthermore, typical components found in motile cilia includes a central pair of microtubules, nexin-dynein regulatory complex, and axonemal inner and outer dynein arms, which generate ciliary movement [81]. A third group of cilia, displaying features intermediate between the two conventionally identified groups, is cilia at the embryonic node. Embryonic node is crucial for the establishment of the left-right asymmetry within the body plan. Termed as "nodal cilia", these cilia exhibit a 9+0 configuration with dynein arms, enabling a rotational motion, differing from the planar beating observed in motile cilia present in other tissues [82] (Fig. 5).

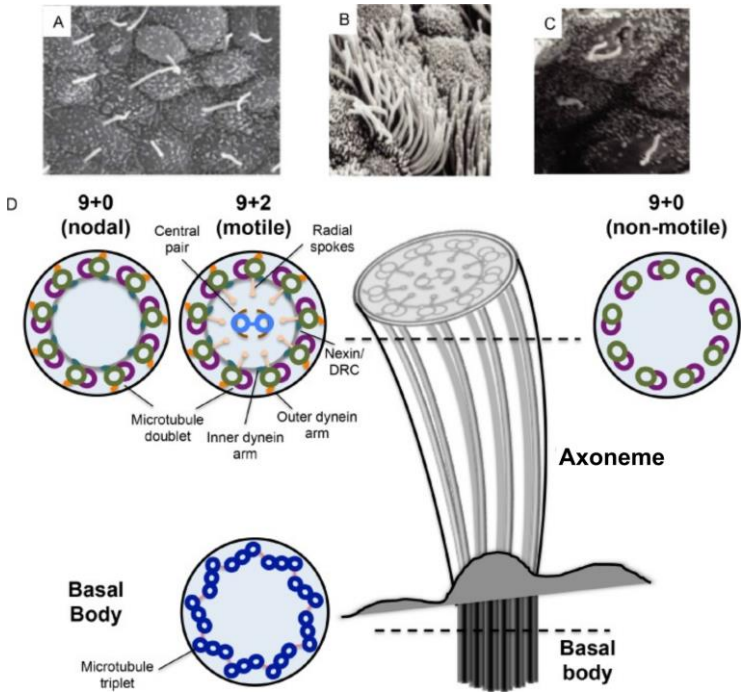

Figure 5: Structure of motile and non-motile cilia. A. *Scanning electron image of mouse single motile nodal cilium.* ***B.*** *Scanning electron image of multiple motile cilia in the mammalian trachea.* ***C.*** *Non-motile primary cilia in renal tubule epithelia.* ***D.*** *Schematic representation of a cilium structure, with cross sections at the axoneme showing the microtubule arrangements in the nodal (9 + 0 motile), motile (9 + 2) and primary (9 + 0 non-motile) cilia, which is extended from the basal body at the apical side within the cell. DRC, dynein regulatory complex (Modified from Praveen et al. 2015* [82]*)*

Similar to the adjacent ependymal cells lining the ventricle, ChP epithelial cells are multiciliated [83], [84]. Multiciliated cells are mainly generated during embryonic development, existing for years in the brain, or undergo continuous renewal across lifespan, particularly in the respiratory and reproductive system. Various intercellular signaling pathways collaborate in determining the differentiation of precursor cells into multiciliated cell lineages. Detailed signaling mechanism for multiciliated fate determination is mainly based on studies of lung and ependymal cells. In human airways, Notch1 pathway inhibition by microRNAs miR-34 and miR-449 is required to suppress the proliferation of progenitor cells and to specify their differentiation into multicilated fate [85]. The most upstream activator of the transcriptional program for multiciliation is geminin coiled-coil domain-containing protein 1 (GEMC1), followed by multicilin (MCIDAS) [85]. Multicilin facilitates the activation of crucial genes essential for multiciliogenesis by interacting with transcription factors E2F4 or E2F5 and their coactivator, DP1 [86] (the E2F4 or E2F5–DP1–multicilin complex is called the EDM

complex). Multicilin also regulates the expressions of RFX2 and FOXJ1. FOXJ1 is a master regulator of motile cilia transcriptional program; it also cooperates with RFX family of transcription factors to induce the expression of key cilium genes; additionally, it is involved in the docking of basal bodies at cell apical surface. FOXJ1 can also be directly activated by GEMC1 and MYB – another core component of multiciliation program [80]. p73 – a p53 homologue – was recently discovered to be downstream of the multicilin – E2F network and to function as a regulator of centriole docking and ciliation [87] (Fig. 6).

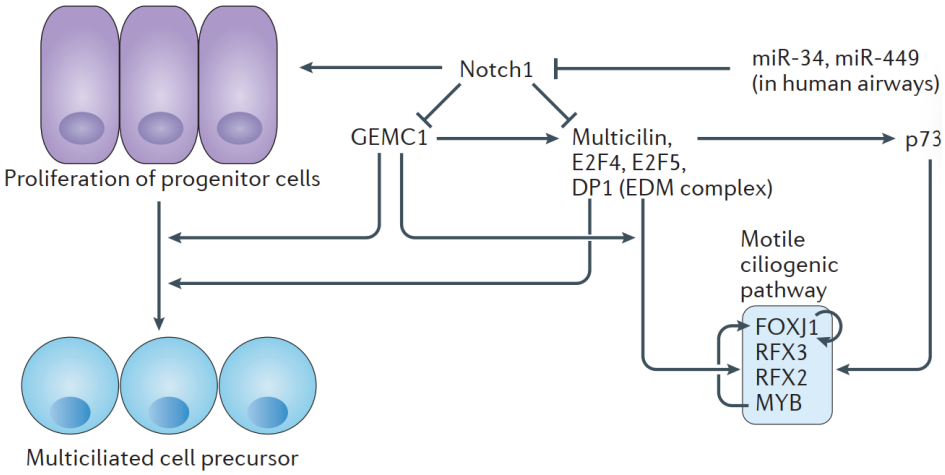

Figure 6: Signaling pathway in fate determination of multiciliated cells *(adapted from Spassky and Meunier 2017* [80]*)*

Multiciliation starts with the amplification of centrioles to generate basal bodies. Both centrioles of the centrosome are considered to be equally capable of generating new centrioles, with their symmetrical duplication being essential for maintaining cell division homeostasis. However, multiciliated cells of the lung and ependyma do not adhere to the conventional duplication process; instead, they mainly produce their centrioles around the electron-dense structures known as deuterosomes. While the mother centriole directly contributes the procentriole formation (centriolar pathway), the daughter centriole contributes to deuterosome generation, consequently giving rise to more than 90% centriole production (deuterosome pathway) [88]. Deuterosome is expressed in response to the formation of the EDM complex and is a spherical-shaped aggregates of DEUP1 protein. Concomitant to DEUP1 expression, the levels of other components of the cascade, such as CEP152, PLK4 and SAS6, are also increased during multiciliated cell precursor differentiation [80]. Generally, the amplification of centrioles takes place through three phases: (i) amplification phase, where multiple deuterosomes

carrying procentrioles are successively generated from the proximal side of the centrosomal daughter centriole. Within this phase, procentrioles also emerge directly from each centrosomal centriole; (ii) growth phase, which starts after finishing deuterosome production and reaching the final centriole number; in this stage, all procentrioles expand and lengthen from centrosome and deuterosome bases; (iii) disengagement phase, where all centrioles detach simultaneously from their centrosome and deuterosome bases to relocate to the apical membrane for motile cilia nucleation (Fig. 7) [80].

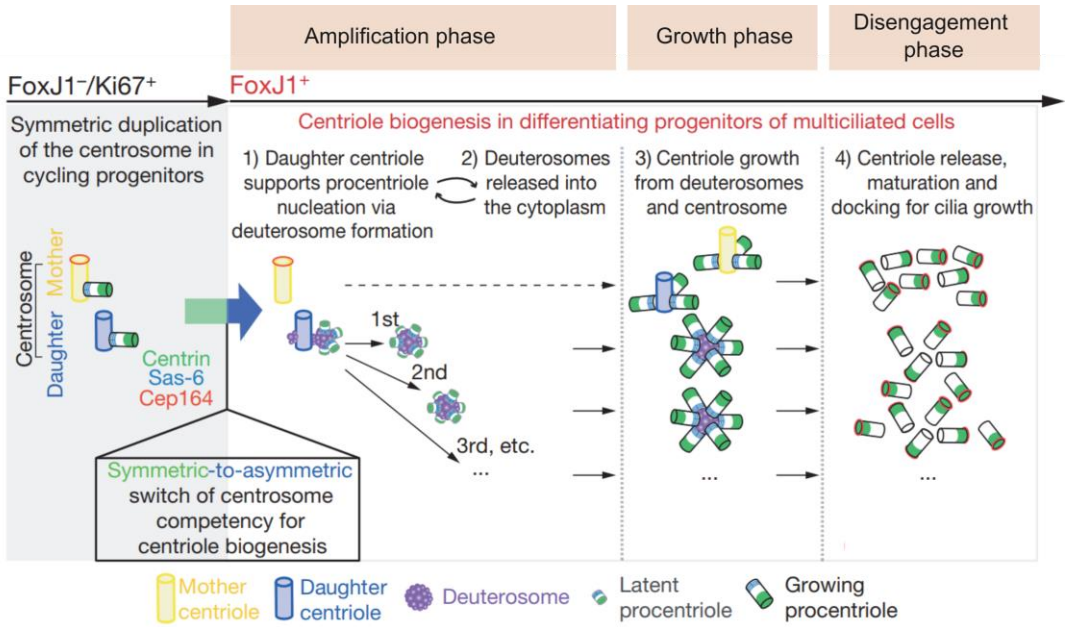

Figure 7: Centriole amplification in ependymal multiciliated cells *(Modified from Al Jord et al. 2015* [88]*)*

Upon simultaneous migration to the apical side of the cell, centrioles dock at the plasma membrane, where they become basal bodies and nucleate motile cilia. Upon the growth of axoneme from each basal body, cilia undergo the last step of maturation to generate unidirectional movement, which is polarization on planar plane – a step regulated by the PCP (Planar cell polarity) pathway [80].

1.3.2. Multiciliated cells of the choroid plexus

Except for the acknowledged fact that choroid plexus cells are multiciliated, literature on the development of ChP cilia is rather scarce and controversial. Early electron microscopy studies reported the presence of 9+2 axonemes in cilia across various species, such as

humans [89] and pigs [90]. However, most of these investigations categorized the ChP as part of the ependymal layer, overlooking potential distinctions between these two cell populations. Recent research in zebrafish has demonstrated that ChP cilia display a 9+2 conformation and are capable of generating directional fluid flow, features highly similar to ependymal cilia [91]. Nevertheless, earlier studies showed that murine ChP cilia exhibit diverse configurations, ranging from 9+0 to 9+1 and 9+2 with the majority is 9+0 structure [92]. Additionally, proteomic analysis of swine ChP cilia identifies 396/868 proteins shared with the proteome of 9+0 photoreceptor cilia, whereas 152/868 is in common with the proteome of 9+2 cilia and flagella [92]. The same research group also reported that in mouse ChP, from embryonic day 13 (E13), the proportion of cells carrying motile cilia increases with time and peaks at to postnatal day 2 (P2), then decrease until 0 at P14. Cilia beating frequency increases from E15 to P2 and plateaus until P10, before diminishing at P14. The majority of ChP cilia was observed to exhibit back-and-forth movement, but a minority shows rotational movement. The ratio of cells with cilia showing rotational movement is highest at E17, then decreases with time and no longer observed after P10. However, even at the peak of P2, the authors demonstrated that ChP cilia movement is insufficient to generate fluid flow [93]. Altogether, these data suggest that ChP cilia is an atypical and sophisticated type of cilia, which is different from those found in the neighboring ependymal cells. Therefore, it is necessary to enhance our comprehension of ChP cilia development, structure, and maintenance.

1.4. Choroid plexus tumors and cilia

Available literature appears to suggest a connection among CPT, ChP cilia, and the disruption of developmental processes. CPT can be detected as early as the third trimester of human pregnancy and nearly 50% of childhood CPT are diagnosed within the first year of life [94]. Therefore, it is likely that CPT has a developmental origin [95]. Multiciliation on the apical surface of ChP epithelial cells is a key feature of ChP differentiation [2] and multiciliated fate determination in ChP takes place since early embryogenesis [93]. Interestingly, Li et al. 2016 [75] reported that while normal human ChP epithelial cells are multiciliated (carrying multiple cilia on apical surface), CPP cells are either a mix of multi- and mono-ciliated cells or all mono-ciliated (carrying only one solitary cilium) cells, and CPC cells are entirely mono-ciliated. They also developed a CPT

mouse model by inducing the sustained expression of *Notch1*, which then lead to unregulated cell proliferation associated with Sonic Hedgehog signaling and the suppression of multiciliated differentiation. Shannon et al. 2018 [78] created a CPT mouse model by over-expression of *Myc*, which results in tumor development with reduced proportion of multiciliated cells and increased presence of cells with a single cilium. A further mechanistic study reveals that NOTCH-driven signaling cascade suppresses multiciliation in CPT cells through the inhibition of GMNC and MCIDAS – early master transcriptional regulators of multiciliation fate. Consequently, *Gmnc-Mcidas* overexpression in mice rescues multiciliation phenotype and suppresses the proliferation of tumor cells [96]. This suggests a fate changing (at early embryonic stage) or fate reversal (at later embryonic/perinatal stage) for tumors to appear in young children and for tumor cells to carry a single cilium.

Additionally, hydrocephalus is the most common presentation of CPT (about 70% cases) along with symptoms like intracranial hypertension, macrocephaly (head circumference is abnormally large), and developmental delay. Hydrocephalus may persist even after tumor removal [97]. Experimental research has increasingly established a stronger connection between cilia and hydrocephalus. An earlier study has shown that in $Tg737^{orpk}$ mutant mice, which is a hypomorphic mutant of a ciliary IFT (intraflagellar transport) component, ChP cells carries cilia with an abnormal bulb-like structure at the cilia tip and develops hydrocephalus through a mechanism relating to increased intracellular cAMP and cAMP-regulated chlorine transport [83]. A recent study on mouse models has found that mast cells located at ChP are increased in number and activated upon brain tumor metastasis and caused hydrocephalus through a cascade of events that involves the disruption of ChP cilia on both the proportion of multiciliated cells and cilia length [98]. These findings strengthen the link between cilia and CPT through the manifestation of hydrocephalus.

It is logical to **examine the pathology of CPT through the lens of developmental signaling in relation to cilia.** However, the normal development of ChP cilia, much like CPT itself, remains an under-studied area, highlighting the need for thorough investigations.

1.5. Scope of the thesis

CPTs are rare tumor with increased frequency and malignancy in children. The scarcity of this tumor often deters scientific inquiry into its underlying mechanisms and optimal treatment strategies. However, this scarcity does not alleviate the suffering of affected young patients, many of whom could potentially gain numerous additional years of life compared to those diagnosed with adult tumors. My PhD project began with a primary focus on **unraveling the aetiology of CPT and developing a novel experimental model for studying this condition**. To achieve this goal, I conducted my research with the following strategy:

- Identify the target signaling pathway/genes through analyses of gene expression and whole-genome sequencing data from human tumor samples; verify bioinformatic findings with human tumor biopsies using histopathological and molecular techniques
- Demonstrate the dependence of cancer cells on the target pathway/genes for survival and proliferation using available pharmacological compounds and methods
- Assess tumorigenic effects of the target pathway/gene on a 2D *in vitro* model of ChP cell line
- Develop a 3D *in vitro* model of CPT by genetic engineering of ChP organoids

Additionally, ChP cilia are implicated in the pathogenesis of CPT and the manifestation of hydrocephalus. However, as normal development of ChP cilia remained elusive, there is a lack of a reliable foundation for designing experiments and interpretating data when investigating abnormal ciliary presentation in pathological conditions like CPT. Therefore, I carried out the second project in my PhD study to **characterize the biogenesis and maintenance of mouse ChP cilia during normal development**. This goal was achieved through the experimental plan to:

- Monitor the proliferation and differentiation of ChP epithelial cells from the beginning of morphogenesis to senescence using *in vivo* tracking and microscopy methods

- Monitor cilia formation and maintenance across the lifetime with multiple high-resolution microscopic techniques to match ciliogenesis with other developmental characteristics of the cells
- Identify mechanisms involved in the maintenance of ChP cilia in postnatal stage with the use of genetically modified mouse model

2. Constitutive activation of Wnt/β-catenin initiates choroid plexus tumors

2.1. Results

2.1.1. CPT patients carry multiple genomic and transcriptomic changes related to Wnt/β-catenin signaling

To identify signaling pathways that could drive CPT initiation, I analyzed published gene expression microarray data containing both healthy ChP and CPP (GSE14098, 8 ChP, 7 CPP samples) [99]. Differentially expressed genes (DEGs) analysis identified 7784 genes with at least two-fold increased or decreased expression (logFC ≥ 1 or logFC ≤ -1 respectively) in CPP. Ingenuity Pathway Analysis (IPA) tool identified "Wnt/β-catenin signaling" as one of a few significantly activated pathways in tumors (Fig. 8A). Wnt/β-catenin signaling is essential for the morphogenesis and development of the ChP [20], [21] and it is known to be a prevalent pathogenic mechanism of many epithelial cancers [100]. To understand how Wnt/β-catenin signaling is altered in CPT, I generated a gene ontology (GO) list, Wnt2GOs, by merging the two GOs "Canonical Wnt pathway" and "Regulation of canonical Wnt", then using this gene list to subset the DEG list. This resulted in 450 statistically significant genes ($p < 0.05$), of which 90 were up-regulated and 131 were down-regulated (Fig. 8B). Up-regulated genes included ligand *WNT2B*, receptor *FZD2*, positive regulator *EGR1* [101] and feedback inhibitor *WIF1* [102]. On the other hand, down-regulated genes were mainly negative regulators of the pathway, such as *APC, SFRP1, SOSTDC1, CYLD, SIAH1* (Fig. 8B).

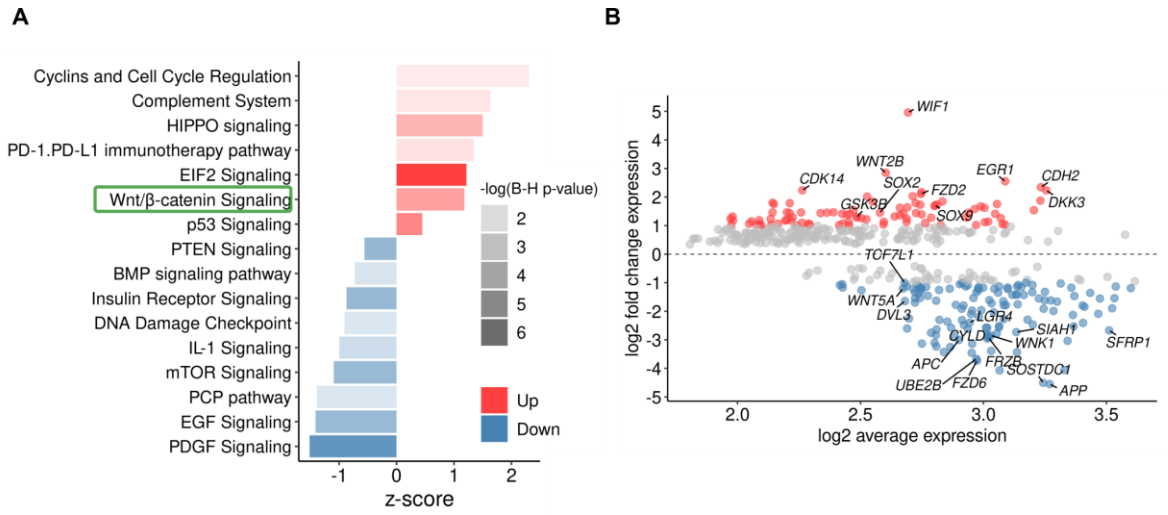

Figure 8. Transcriptomic analysis shows Wnt/β-catenin signaling is activated in human choroid plexus tumors (CPTs). A, *Top IPA (ingenuity pathway analysis) pathways of gene expression microarray data enriched in choroid plexus papilloma (CPP, n = 7) versus healthy choroid plexus (ChP, n = 8). P-value of the enriched term is reflected by the color shade of the bar.* ***B,*** *MA plot of Wnt2GOs list genes filtered from the microarray data. Genes up-regulated in CPP ($p < 0.05$ and log_2[fold change] ≥ 1, n = 90 genes) are highlighted in red; genes down-regulated in CPP ($p < 0.05$ and log_2[fold change] ≤ -1; n = 131 genes) are highlighted in blue. Selected genes are labeled.*

Next, I performed a targeted genomic analysis of the Wnt/β-catenin signaling pathway. I analyzed whole genome sequencing (WGS) data of 15 tumors (12 CPPs and 3 CPCs) and matched blood samples acquired from the CBTTC (Children's Brain Tumor Tissue Consortium) database (Table 13). I analyzed somatic and germline SVs (Structural Variants), SNVs (Single Nucleotide Variants) and Indels (Insertions/Deletions) using in-house analysis pipelines [103] (Fig. 9A, 11A). To examine the extent to which Wnt/β-catenin signaling genes are affected by SV variants, I used the Wnt2GOs gene list to subset the SV list, which resulted in multiple somatic and germline SV events on every chromosome (Fig. 9B, 10A). Although only a few SVs were found directly in Wnt/β-catenin genes, their sizes are rather large (around 300 bp) (Fig. 9C), potentially disrupting genes expression levels. Many somatic and germline SVs are located upstream or downstream of Wnt/β-catenin signaling genes. These SVs include deletion, duplication, inversion and translocation with average size of around 1 Kb and could be larger than 100 Mb (Fig. 9D-E, 10B-C). The majority of SVs, although not located right at the Wnt/β-catenin pathway genes, still occurred within 2 Kb – 5 Mb distance (Fig. 9D-E, 10B-C), where containing probable regulatory elements [104], [105], thus potentially

affecting the expression of Wnt/β-catenin pathway genes. Some of these genes have SVs (located within 5 Mb distance) in up to 20% - 40% tumor samples (Fig. 2F-G, 3D-E).

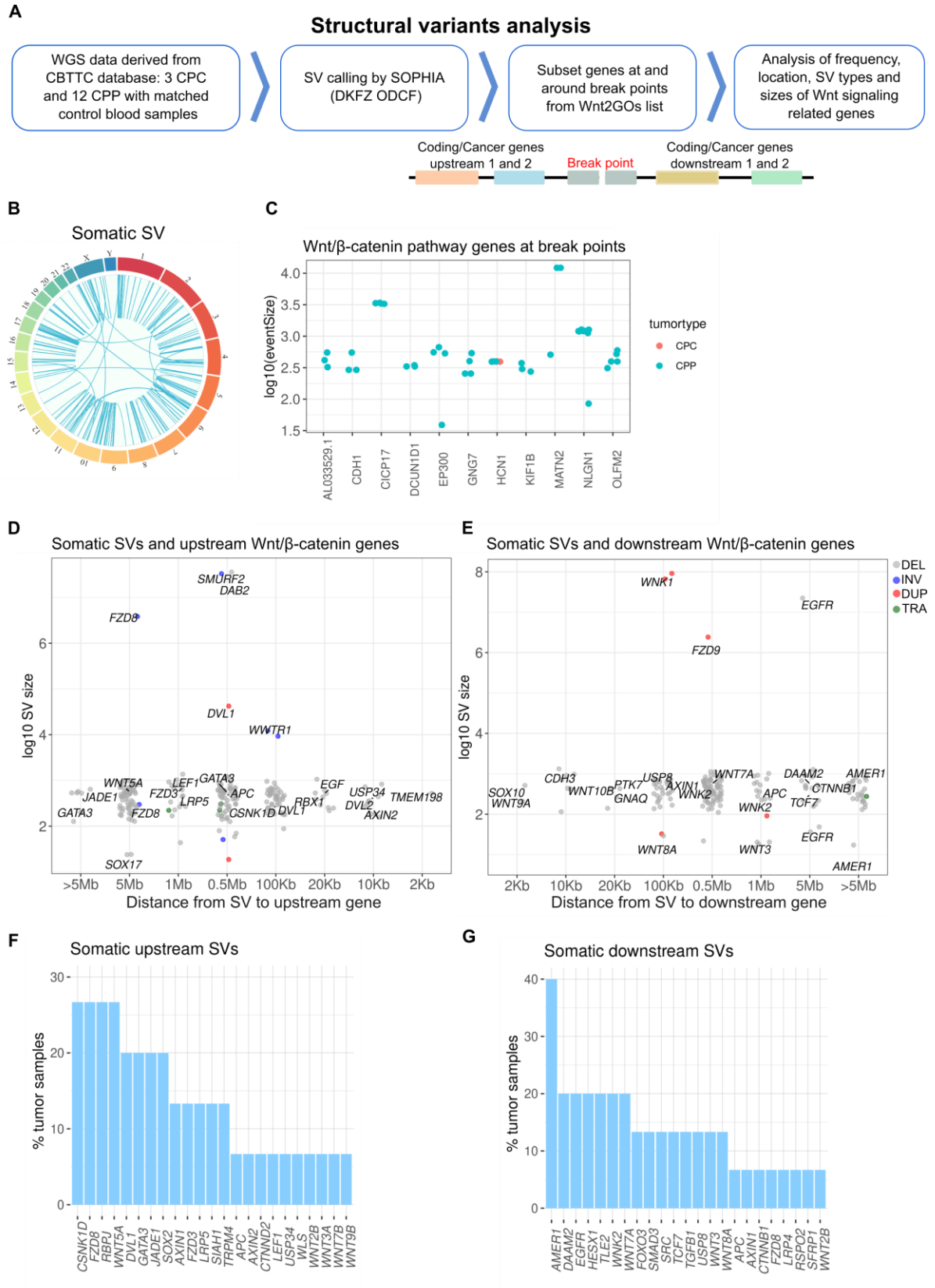

Figure 9. Analyses of somatic structural variants (SVs) on genes of Wnt/β-catenin signaling pathway in human choroid plexus tumors (CPTs). A, *SV analysis pipeline.* ***B,*** *Circos plots show chromosomal distribution of somatic SVs relating to Wnt/β-catenin signaling genes.* ***C,*** *SVs directly occur at genes of Wnt/β-catenin pathway.* ***D,*** *Somatic SVs with their sizes and distances to upstream Wnt/β-catenin signaling genes.* ***E,*** *Somatic SVs with their sizes and distances to downstream Wnt/β-catenin signaling genes. DEL: deletion, DUP: duplication, INV: inversion, TRA: translocation.* ***F,*** *The percentage of CPT samples carrying somatic SVs upstream of Wnt/β-catenin signaling genes.* ***G,*** *The percentage of CPT samples carrying somatic SVs downstream of Wnt/β-catenin signaling genes.*

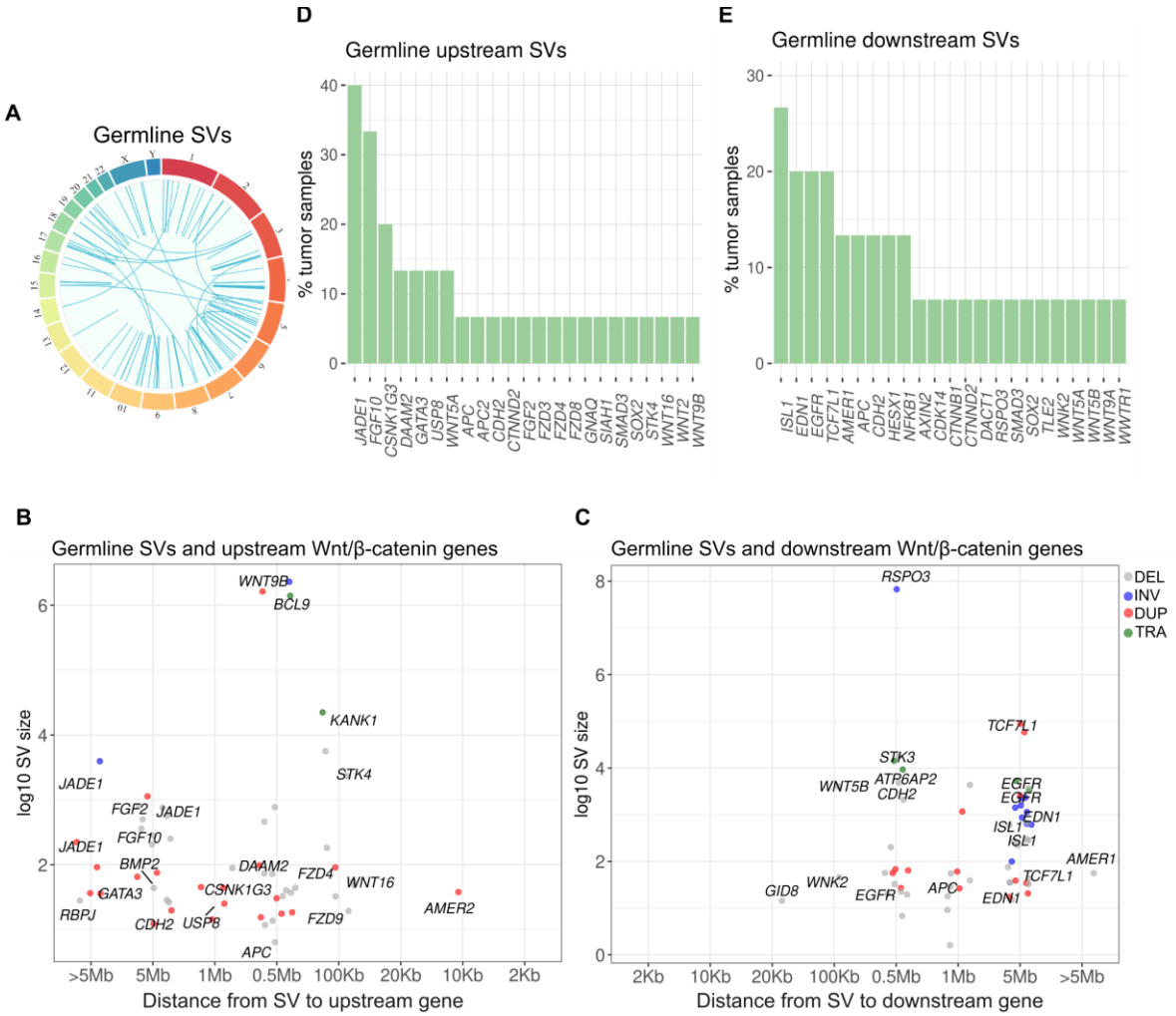

Figure 10. Analyses of germline structural variants (SVs) on genes of Wnt/β-catenin signaling pathway in human choroid plexus tumors (CPTs). A, *Circos plots show chromosomal distribution of germline SVs relating to Wnt/β-catenin signaling genes.* ***B,*** *Germline SVs with their sizes and distances to upstream Wnt/β-catenin signaling genes.* ***C,*** *Germline SVs with their sizes and distances to downstream Wnt/β-catenin signaling genes. DEL: deletion, DUP: duplication, INV: inversion, TRA: translocation.* ***D,*** *The percentage of CPT samples carrying germline SVs upstream of Wnt/β-catenin signaling genes.* ***F,*** *The percentages of CPT samples carrying germline SVs downstream of Wnt/β-catenin signaling genes.*

Because SVs could induce nearby SNVs within a region of 1-10 Mb [106], [107], I next examined SNVs occurrence on Wnt/β-catenin genes. Using the same WGS data, I focused on genes in the Wnt2GOs list carrying SNVs and Indels. To exclude normal polymorphisms, I applied a cutoff threshold ≤ 1% for minor allele frequency [108], [109], and identified varied numbers of somatic and germline SNVs/Indels on Wnt/β-catenin pathway genes in all samples (Fig. 4B, 5A). I uncovered 588 somatic SNV/Indel variants, of which 49.5% were novel. 68% somatic variants were intronic, followed by 11% of non-coding transcript variants (Fig. 4C). Non-coding somatic SNVs have been proved to underlie the tumorigenesis of various cancers [110], [111], [112] and play a major role in shaping the transcriptome of children brain cancers [113]. I also identified 149 germline variants and the majority of them were existing variants (93.3%). Germline variants belonged to a broader category including missense (25%), downstream gene (19%) and intron (14%) variants (Fig. 5B). While somatic variants attract more investigations as cancer drivers, germline variants may predispose patients to tumorigenesis. This is particularly relevant in the case of childhood CPTs, which often occur in <1-year-old children [94]. Indeed, a recent pan-cancer study reported around 6% childhood cancer patients carry a causative germline variant [114]. Genes with high somatic variant frequencies include *CTNND2* (80%), *CDK14* (46.67%), *FGF10, GSK3B, LRP6* (each 33.3%) (Fig. 3D). Genes with high germline variant frequencies include *TCF7L1* and *WNK2* (each 33.3%), *APC, DVL1, DVL2, EGF* (each 20%) (Fig. 5C). Multiple *WNT* ligand genes had somatic and/or germline variants although with low frequency (<20%) (Fig. 3D, 5C). Of note, these variants were not recurrent within the studied cohort, which is in agreement with previous studies reporting the lack of driver genes in CPT [72].

In addition to frequency, it is important to assess if those variants are benign or pathogenic. VEP tool allows for the interpretation and prediction of variants' biological meanings and potential pathogenicity through a range of algorithms. LOEUF (loss-of-function observed/expected upper bound fraction) [115] score measures genes' intolerance to LoF (Loss of Function) variations. LoF includes stop-gained, frameshift and essential splice variants; they are on average deleterious and therefore typically maintained at low frequency in human population. In this study, I used LOUEF score of 0.2 as cutoff, which mean >80% probability that those genes belong to the class of LoF-haploinsufficient genes [115]. Wnt/β-catenin pathway genes that are LoF-haploinsufficient and carry (i) somatic SNV/Indel variants include *CTNND2, PRICKLE1,*

USP34 (Fig. 11E), (ii) germline SNV/Indel variants include *APC, USP34, WNK2* (Fig. 12D). CADD (Combined Annotation Dependent Depletion) scores the predicted deleteriousness of SNVs/Indels [116]. CADD scores are often Phred-scaled; variants with CADD-Phred 10 or 20 are predicted to be among the 10% or 1% most deleterious substitutions that can occur in the human genome. Multiple variants of well-known Wnt/β-catenin pathway genes were predicted with CADD-Phred scores above 10, including *LGR4, DVL3, LRP6, DKK2* (somatic, Fig. 11F), *WLS, APC, CTNNB1, DVL2* (germline, Fig. 12E), suggesting the disruption of these genes by their variants. SIFT and PolyPhen predict the effect of amino acid substitution on protein structure and function. The lower SIFT score, or the higher PolyPhen score, indicates higher intolerance. Because most somatic variants in this cancer happened on non-coding regions (Fig. 11C), only a few somatic variants were evaluated with SIFT and PolyPhen (Fig. 11G-H). The amino acid substitutions evaluated to be deleterious by both algorithms occur on *LGR4* (somatic, Fig. 11G-H), *LGR4, DVL2* (germline, Fig. 12F-G).

Finally, I calculated the proportions of SNVs/Indels variants relating to Wnt/β-catenin signaling and to other common oncogenic pathways and found that Wnt/β-catenin signaling is the second most enriched pathway, in both somatic and germline variants (Fig. 11I, 12H).

In summary, bioinformatic data suggested an activation of Wnt/β-catenin signaling in CPT, potentially due to numerous SVs, SNVs and Indels variants affecting the expressions of multiple Wnt/β-catenin signaling genes.

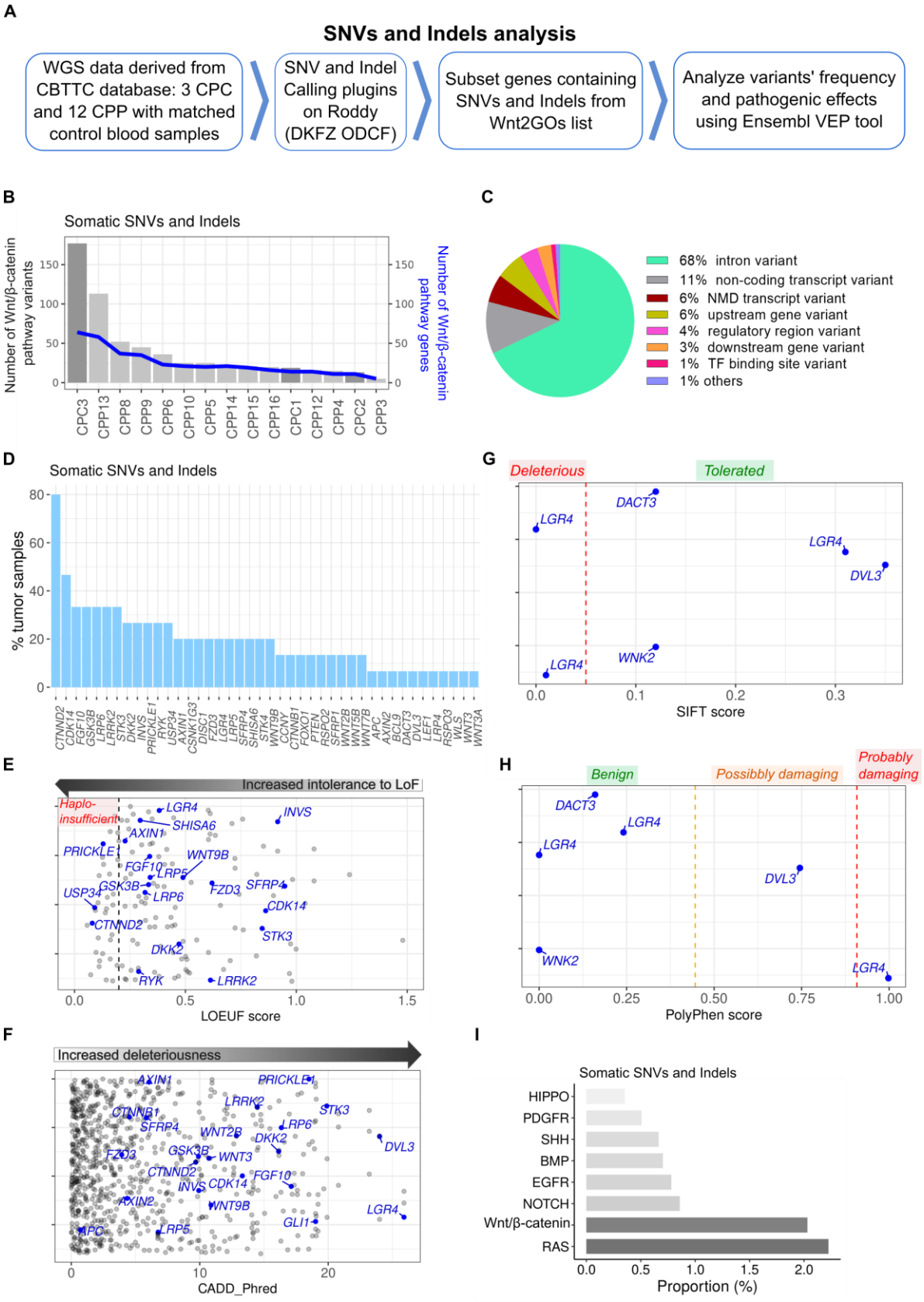

Figure 11: Analyses of somatic single nucleotide variants (SNVs) and insertion/deletion variants (Indels) on genes of Wnt/β-catenin signaling in human choroid plexus tumors (CPTs). A, *SNVs and Indels analysis pipeline.* ***B,*** *The numbers of Wnt/β-catenin signaling genes*

carrying somatic SNV/Indel variants and the number of those variants in each tumor sample. ***C,*** *The composition of germline SNV/Indel variants of CPT samples.* ***D,*** *Frequencies of Wnt/β-catenin signaling genes with somatic SNV and Indel variants.* ***E,*** *LOEUF score evaluating the intolerance to LoF (loss of function) mutations of Wnt/β-catenin signaling genes carrying somatic SNV/Indel.* ***F,*** *CADD-Phred score indicating deleteriousness of somatic SNV/Indel variants on Wnt/β-catenin signaling genes.* ***G-H,*** *SIFT (****G****) and Polyphen (****H****) scores assessing deleteriousness of amino acid substitutions caused by somatic SNV/Indel variants.* ***I,*** *Proportions of genes in common oncogenic pathways that carry somatic SNVs/Indels in at least 50% samples.*

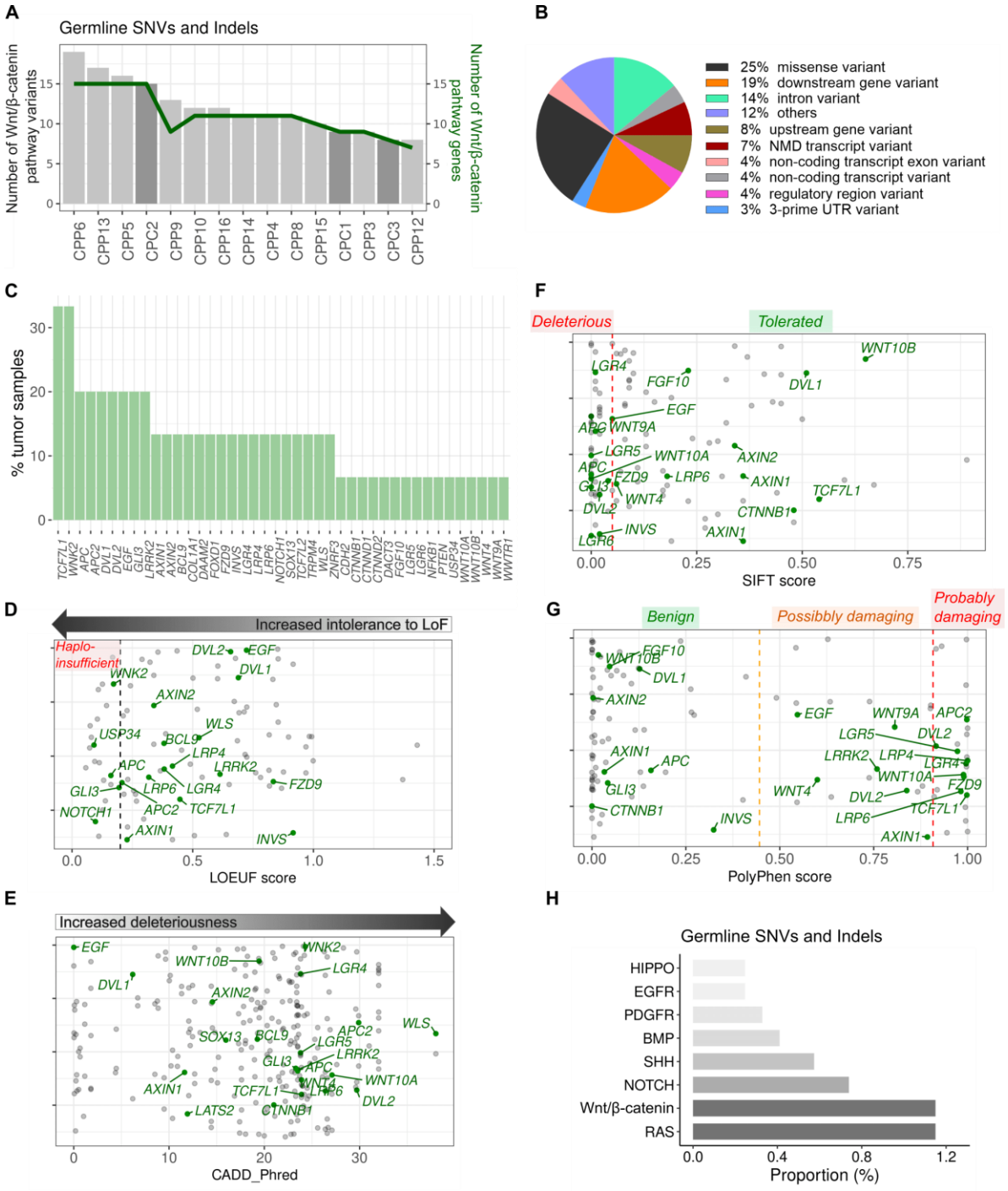

Figure 12: Analyses of germline single nucleotide variants (SNVs) and insertion/deletion variants (Indels) on genes of Wnt/β-catenin signaling in human choroid plexus tumors (CPTs). A, *The numbers of Wnt/β-catenin signaling genes carrying germline SNV/Indel variants and the number of those variants in each tumor sample.* ***B,*** *The composition of germline SNV/Indel variants of CPT samples.* ***C,*** *Frequencies of Wnt/β-catenin signaling genes with germline SNV and Indel variants.* ***D,*** *LOEUF score evaluating the intolerance to LoF (loss of function) mutations of Wnt/β-catenin signaling genes carrying germline SNV/Indel.* ***E,*** *CADD-Phred score indicating deleteriousness of germline SNV/Indel variants on Wnt/β-catenin signaling genes.* ***F-G,*** *SIFT (**F**) and Polyphen (**G**) scores assessing deleteriousness of amino acid substitutions caused by germline SNV/Indel variants.* ***H,*** *Proportions of genes in common oncogenic pathways that carry germline SNVs/Indels in at least 50% samples.*

2.1.2. Wnt/β-catenin signaling is activated in human choroid plexus tumors

The key feature of the activation of Wnt/β-catenin signaling is the stabilization of β-catenin from proteasomal degradation and subsequent translocation into cell's nucleus where it cooperates with TCF/LEF transcription factor to induce the expressions of target genes, such as *AXIN2, MYC, SP5, NOTUM* [117](Fig. 13A). To verify activation of Wnt/β-catenin signaling in CPT, I stained human tumor samples (Table 2) for β-catenin (CTNNB1). Qualitative and quantitative analyses showed a clear increased localization of β-catenin in both cytoplasm and nuclei compartments of CPT, indicating an activation of Wnt/β-catenin signaling (Fig. 13B-D). β-catenin cytoplasmic localization was confirmed with immunofluorescence double staining against β-catenin and TTR (Fig. 13E). This result is concordant with previous β-catenin staining in both human and canine CPTs [118], [119]. RT-qPCR and Western blot analyses of human samples showed consistent results of Wnt/β-catenin signaling activation: i) the mRNA expression and protein levels of the *bona fide* Wnt/β-catenin target gene *AXIN2* were increased (Fig. 13F-H); (ii) total β-catenin protein levels were elevated in CPT samples (Fig. 13G-H), without affecting its mRNA levels (Fig. 13F); iii) the proportion of activated CTNNB1 (unphosphorylated at Ser37/Thr41) (Fig. 13A) over total CTNNB1 was increased, particularly in CPP (Fig. 13I, J); (iv) the mRNA levels of Wnt/β-catenin signaling negative regulators, *APC* and *SFRP1*, were downregulated while *APC*-associated target genes, *SP5* and *NOTUM*, were upregulated (Fig. 13F); and (v) DVL2 protein expression level and the proportion of phosphorylated DVL2 (demonstrated as a shift in DVL2 band) are increased, particularly

in CPP (Fig. 13I, K, L). Due to limited availability of human samples, analyses of DVL2 and activated CTNNB1 proteins were unable to draw conclusive results. These data proved that Wnt/β-catenin signaling is activated in human CPT.

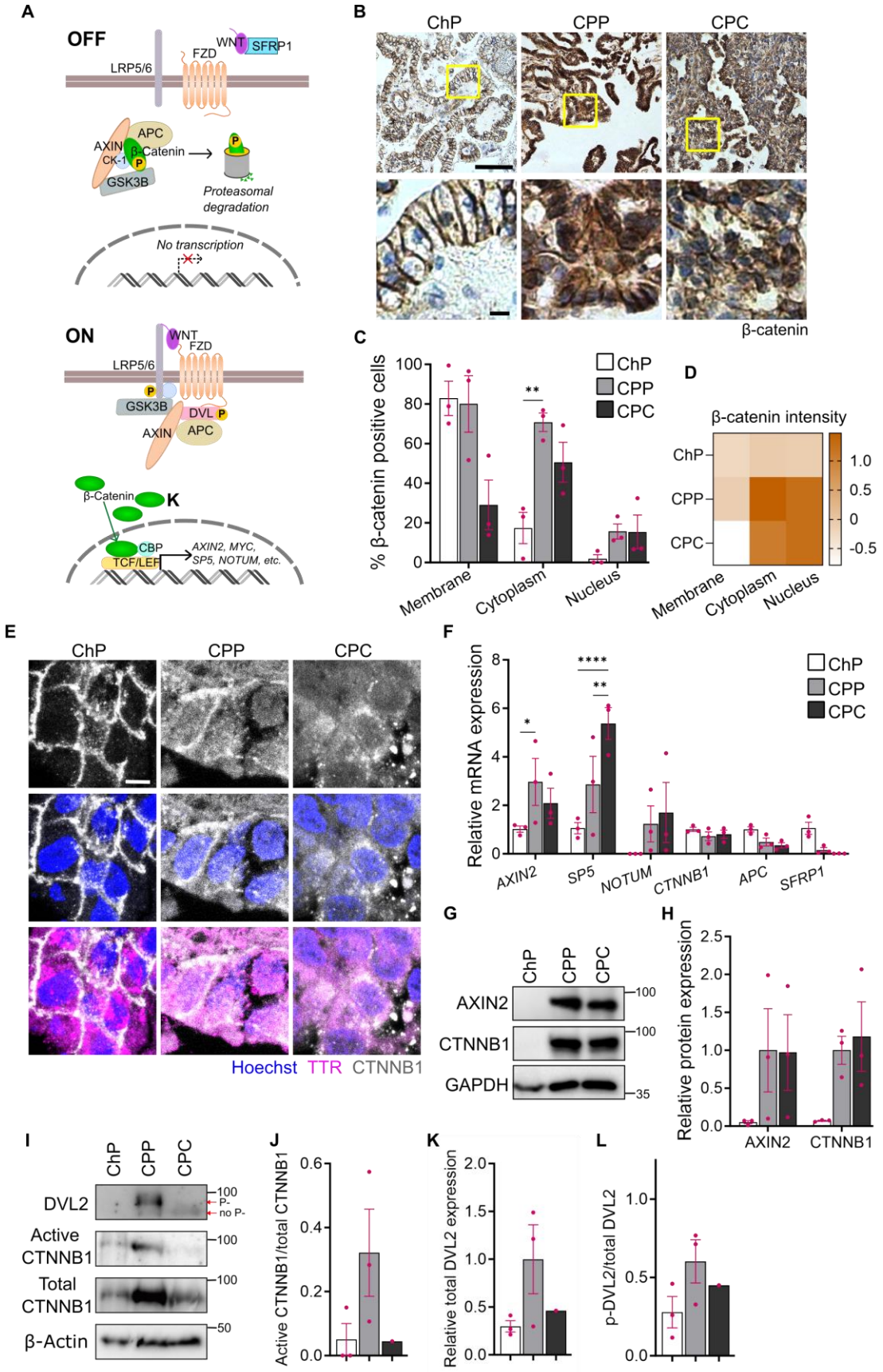

Figure 13: Confirmation of the activation of Wnt/β-catenin signaling pathway in human choroid plexus tumors. A, *Schematic illustration of Wnt/β-catenin signaling pathway.* ***B,***

Representative photomicrographs illustrating β-catenin (CTNNB1) positive cells in post-operative choroid plexus papilloma (CPP), choroid plexus carcinoma (CPC) and healthy choroid plexus (ChP). ***C,*** *Quantification of β-catenin positive cells in three different cellular compartments. n = 3 biological replicates (5-8 random fields for each sample).* ***D,*** *Pseudo-quantification of β-catenin intensity in three different cellular compartments. n = 3 biological replicates (5-8 random fields for each sample). Intensity scores are averaged scores given by two independent evaluators compared to β-catenin level of a chosen image of ChP (Score; -2: much weaker, -1: weaker, 0: similar, 1: stronger, 2: much stronger).* ***E,*** *Representative immunofluorescence images of ChP, CPP and CPC stained for β-catenin (CTNNB1), TTR and Hoechst, showing compartmentalization of CTNNB1 and TTR.* ***F,*** *Relative mRNA expression levels of several Wnt/β-catenin signaling genes in CPP, CPC and ChP. n = 3.* ***G-H,*** *Representative Western blot images of AXIN2 and CTNNB1 (**G**) and quantifications of their relative expressions in independent ChP, CPP and CPC human samples, n = 3 (**H**).* ***I,*** *Representative Western blot images of DVL2, active CTNNB1 (non-phosphorylated at Ser37/Thr41) and total CTNNB1 in human samples. Blots in (**I**) and (**J**) were created using 2 different protocols in 2 different laboratories.* ***J-L****, Ratio of active CTNNB1 over total CTNNB1 (**J**), Relative expression level of DVL2 (**K**) and ratio of phosphorylated DVL2 over total DVL2 (**L**) in ChP, CPP and CPC human samples. n = 3 for (**J, K**) and n = 1 for **L** due to limited availability of CPC tumor samples. Scale bar: main: 50 µm, inset: 10 µm (**B**); 5 µm (**E**). Bars represent Mean ± SEM; Two-Way ANOVA test, Tukey multiple comparison (**C, F**); Unpaired t-test, (**J-L**). *p≤0.05, **p≤0.01, ***p≤0.001, ****p≤0.0001. Staining against CTNNB1 in Figure 13B was provided by Dr. Christian Thomas. Figure 13I was provided by Dr. Ondra Bernatík. Figure 13J-L were provided by Dr. Alena Salasova.*

To investigate the dependence of CPT on Wnt/β-catenin signaling, I treated the human CPP cell line HIBCPP with WNT974, a PORCN inhibitor, which targets the palmitoylation of WNT ligands and, thus, blocks their secretion [120] (Fig. 14A). WNT974 diminished HIBCPP cell viability in a dose-dependent manner (Fig. 14B). TOPFlash assay showed that HIBCPP cells indeed exhibited autocrine WNT and that WNT974 treatment down-regulated Wnt/β-catenin signaling, as demonstrated by reduced luminescence signal in treated cells (Fig. 14C). In addition, mRNA expression of Wnt/β-catenin target genes (*AXIN2, MYC)* and other feedback regulators (*WIF1, DKK1*) were reduced (Fig. 14D). Similarly, protein levels of the target protein AXIN2 and transcription co-activator CTNNB1 were down-regulated upon drug treatment (Fig. 14E, F). Thus, WNT974 treatment indeed down-regulates Wnt/β-catenin signaling in HIBCPP cells. This led to significant reduced number of colonies under drug treatmnet in the clonogenic assay (Fig. 14G, H). WNT974 also significantly reduced the number of proliferative cells in EdU incorporation assay (Fig. 14I, G), increased the percentage of cells in G1 phase (G1 blockage) and decreased those in S phase as measured by flow cytometry (Fig. 14K). These data suggests that autocrine WNT secretion is required for HIBCPP cellular

proliferation. Cell death analysis, using Annexin V/PI staining, showed reduction of living cells (AV-/PI) and an overall increase of dead cells, yet no increase in apoptosis (AV+/PI-) (Fig. 14L, M). Overall, our data the human CPP-derived cell line HIBCPP is dependent on Wnt/β-catenin pathway for its maintenance and proliferation.

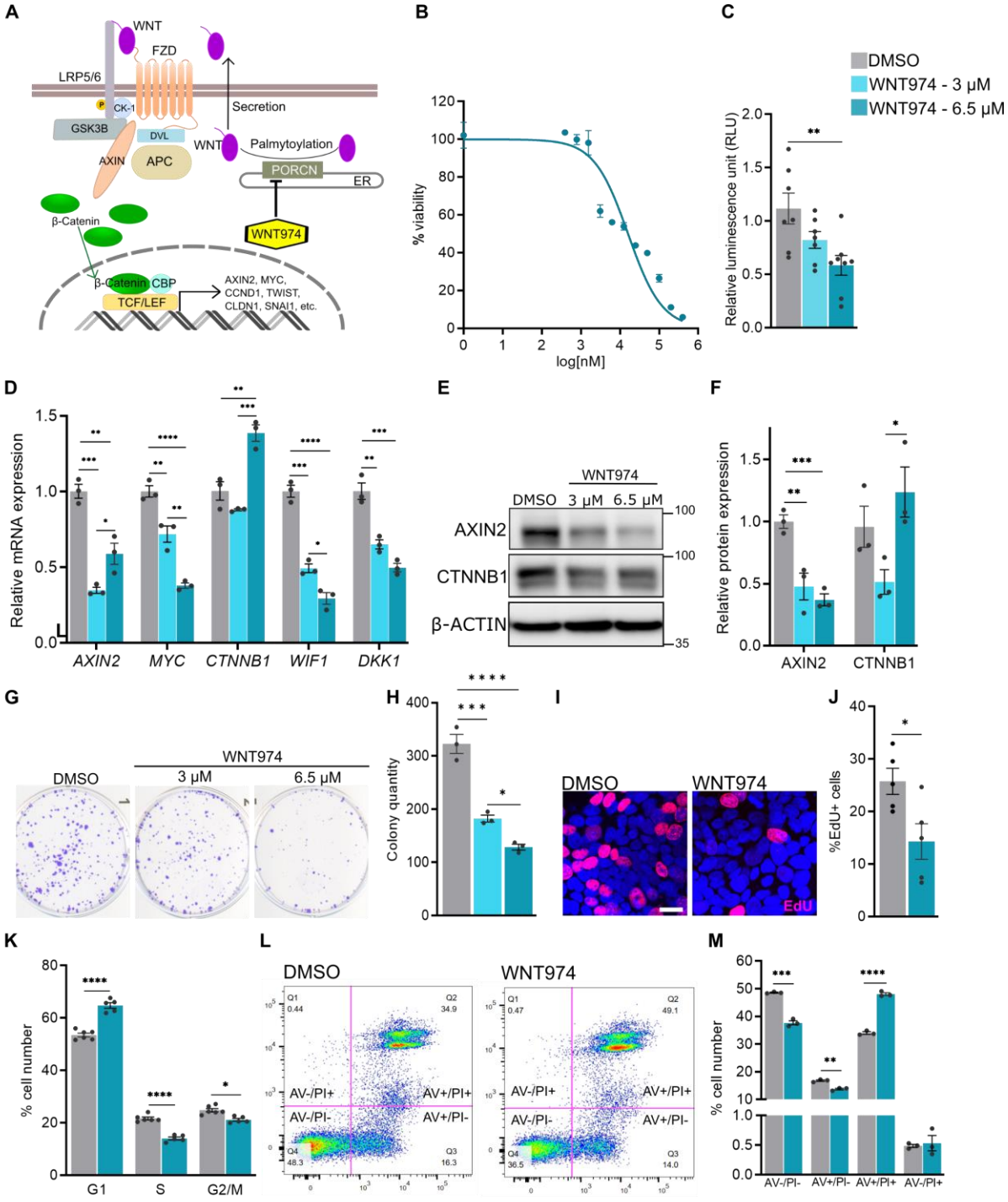

Figure 14. Human choroid plexus tumor (CPT) cells are dependent on Wnt/β-catenin signaling. A, *Schematic illustration of inhibition mechanism of WNT974 on Wnt/β-catenin*

pathway. ***B,*** *Cell survival curve of HIBCPP cells after treatment with WNT974; n = 3.* ***B,*** *Luciferase assay quantification of Wnt/β-catenin signaling activation in WNT974-treated HIBCPP cells; n = 7.* ***D,*** *Relative mRNA expression levels of several key genes in Wnt/β-catenin pathway; n = 3.* ***E-F,*** *Representative image (**E**) and relative quantification (**F**) of Western blot analysis of AXIN2 and CTNNB1 in WNT974-treated HIBCPP cells; n = 3.* ***G-H,*** *Representative image (**G**) and quantification (**H**) of clonogenic assay of HIBCPP cells treated with WNT974 at 3 μM and 6.5 μM. n = 3.* ***I-J,*** *Representative confocal images (**I**) and quantification (**J**) showing EdU-positive cells in WNT974- and DMSO-treated HIBCPP cells; n = 5. Scale bar: 20 μm.* ***K,*** *Cell cycle progression of WNT974-treated HIBCPP cells quantified by flow-cytometry; n = 5-6.* ***L-M,*** *Representative flow cytometry plots of Annexin V (AV)-Propidium Iodide (PI) staining in WNT974- and DMSO-treated HIBCPP cells (**L**) and quantifications of 4 cell populations (**M**); n = 3. Bars represent Mean ± SEM. One-Way ANOVA test, Tukey multiple comparison (**C, D, F, H**); Unpaired t-test (**J, K, M**). Bars represent Mean ± SEM; *p≤0.05, **p≤0.01, ***p≤0.001, ****p≤0.0001.*

2.1.3. Activation of Wnt/β-catenin signaling induces tumorigenic features in a choroid plexus cell line

To evaluate the role of Wnt/β-catenin signaling in ChP tumorigenesis, I created 2D *in vitro* models of Wnt signaling activation. *APC* is one of the most significant drivers for cancers of Wnt/β-catenin signaling [121] and has 4-fold decreased expression in CPP (logFC = -2.05) (Fig. 1B). Using CRISPR/Cas9 technique, I knocked-out (KO) the *Apc* gene in Z310 cells, an immortalized rat choroidal epithelial cell line [122], blocking the formation of β-catenin destruction complex and, thus, constitutively activating the Wnt/β-catenin signaling (Fig. 15A). Two independent *Apc* knock-out (*Apc*_KO) clones from the same sgRNA were selected for analyses. *Apc*_KO cell lines showed a significant increase in TOPFlash luminescence signals, exceeding the level of cells exogenously treated with WNT3A conditioned medium (Fig. 15B). At transcriptional level, *Axin2* mRNA was upregulated in *Apc*_KO cells, while *Ctnnb1* expression was unaffected (Fig. 15C). At translational level, Western blot confirmed the depletion of APC in both clones and showed upregulation of AXIN2, CTNNB1 protein levels, and a decrease of phosphorylated CTNNB1 (Fig. 15D, E). This implies that β-catenin was mostly regulated at translational and post-translational levels. Both *Apc*_KO cell lines showed clear nuclear accumulation of β-catenin and increased cytoplasmic localization (Fig. 15F). Altogether, the data demonstrated the activation of Wnt/β-catenin pathway in *Apc*_KO lines.

To assess functional aspects of *Apc*_KO cells, I performed the assay of colony formations in soft agar, which assesses cells' anchorage-independent growth - a hallmark of

carcinogenic transformation [123]. *Apc*_KO cells formed significantly more colonies in soft-agar assay (Fig. 15G-H), demonstrating tumorigenic potential of Wnt/β-catenin activation through *Apc*_KO. To further assess *Apc*_KO and *WNT3A*_OE cell lines' oncogenic properties, I carried out organotypic brain slices invasion assays [124]. Cells were first grown into spheroids (Fig. 15I); after 4 days of culture, spheroids were implanted on brain slices and subsequently cultured for an additional 48 hours. Imaging data showed that *Apc*_KO1 extended more and longer protrusions from the spheroids' core, showing significantly increased invasion ability compared to control (Fig. 15K, L). On the other hand, *Apc*_KO2 failed to exhibit parenchymal invasion (Fig. 15K, L), possibly due to its weaker ability to form spheroids in the first place (Fig. 15I, J).

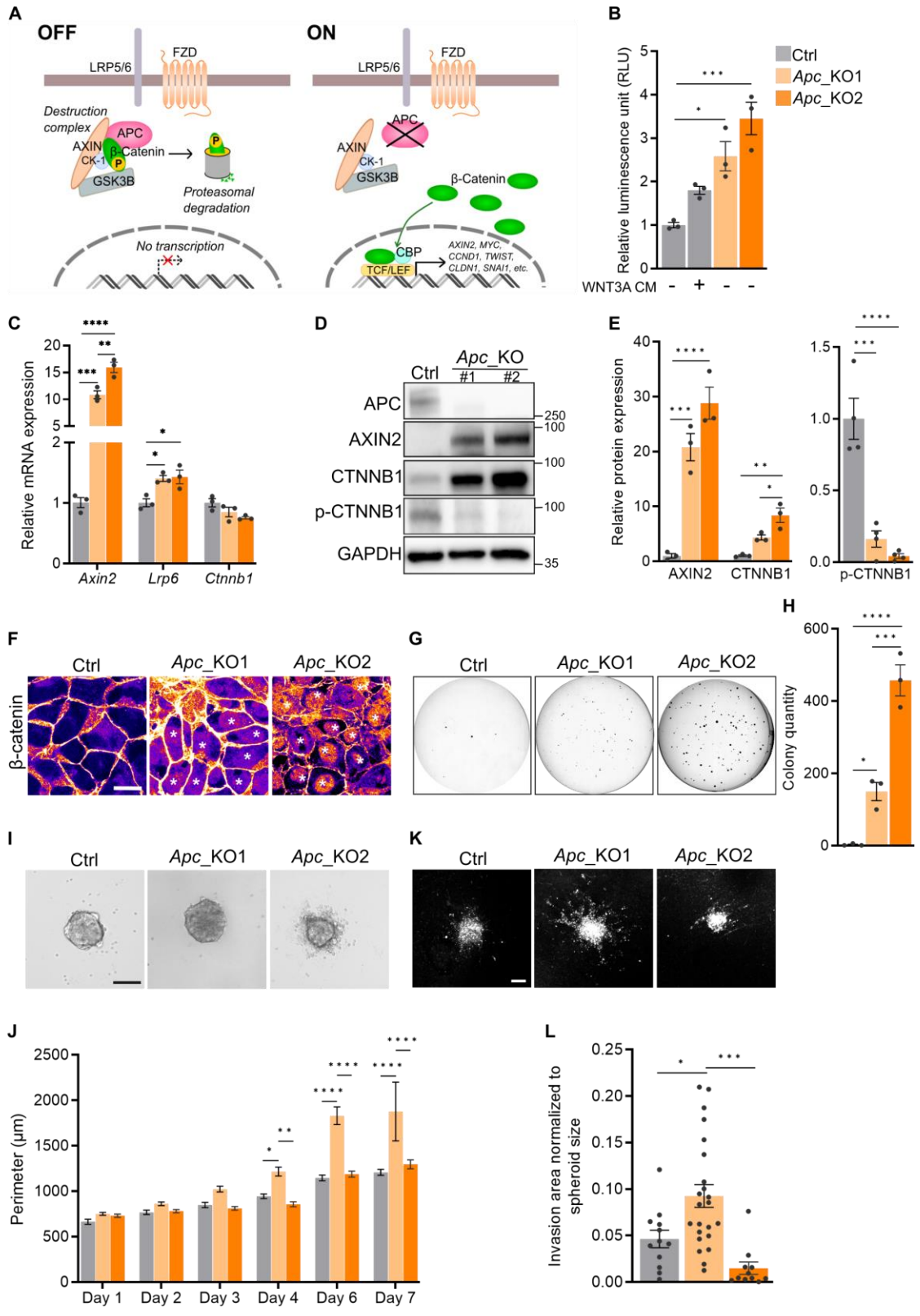

Figure 15. Wnt/β-catenin signaling activation through Apc knock-out in 2D in vitro models. ***A,*** *Schematic illustration of Wnt/β-catenin signaling activation through depletion of Apc.* ***B,*** *Luciferase assay quantification of Wnt/β-catenin signaling in Apc knockout (Apc_KO) and control (Ctrl) cell lines. n = 3.* ***C,*** *Relative mRNA expression levels of several key genes in Wnt/β-catenin pathway; n = 3.* ***D-E,*** *Representative images and relative quantification of Western blot analyses of*

Wnt/β-catenin signaling genes in Apc_KO cells. n = 3. ***F,*** *Representative confocal images of Apc_KO and Ctrl cells stained against β-catenin. Asterisks indicate nuclear β-catenin.* ***G-H,*** *Representative image (**G**) and quantification (**H**) of colonies formed in soft-agar assay of Apc_KO and Ctrl cells. n = 3.* ***I-J,*** *Representative bright-field images (**I**) and measurement of spheroid perimeter (µm) (**J**) of control (Ctrl) and Apc_KO cells monitored in 7 days. n = 6-9.* ***K,*** *Representative confocal DiI images of Ctrl and Apc_KO spheroids in brain slices after 48h of Ctrl and Apc_KO spheroids.* ***L,*** *Invasion area of Ctrl and Apc_KO spheroids after 48h, n = 11-24. Scale bar: 20 µm (**F**), 100 µm (**I, K**). Bars represent Mean ± SEM. One-Way ANOVA test, Tukey multiple comparison (**B, C, E, H, J, L**); *p≤0.05, **p≤0.01, ***p≤0.001, ****p≤0.0001. Spheroid invasion quantification were blindly performed by Dr. Ekaterina Ivanova.*

Next, I employed a second strategy to activate Wnt/β-catenin via over-expression of the *WNT3A* ligand (*WNT3A*_OE) in Z310 cell line (Fig. 16A). *WNT3A*_OE cells showed a 2-fold increase of the TOPFlash luminescence signal compared with controls and responded to WNT inhibition by DKK1 proteins (Fig. 16B). *WNT3A*_OE cells also had increased expression of *Axin2* and *c-Myc* mRNA (Fig. 16C), as well as increased protein levels of AXIN2 and CTNNB1 (Fig. 16D, E), although not reaching induction levels observed upon *Apc* KO (Fig. 15D, E). β-catenin staining showed nuclear accumulation (Fig. 16F), proving that the overexpression of *WNT3A* activates Wnt/β-catenin signaling. Although insignificant, there was a trend of increase in the quantity of colonies formed in soft-agar in *WNT3A*_OE cells compared to control (Fig. 16G, H). No difference in spheroid formation and brain slice invasion were observed for *WNT3A*_OE cells compared to control (Fig. 16I-K).

In summary, by using different strategies to activate Wnt/β-catenin pathway, I showed that pronounced Wnt/β-catenin activation is sufficient to induce tumorigenic properties, such as anchorage-independent growth, proliferation and brain invasion in ChP cells. Although both 2D *in vitro* models - *Apc*_KO and *WNT3A*_OE - aimed at constitutively activating Wnt/β-catenin, their functional read-out and tumorigenic features differed, possibly due to differences in the amplitude of activation of the Wnt/β-catenin pathway. These data provided the first level of experimental evidence on how the selective activation of this pathway is involved in CPT tumorigenesis.

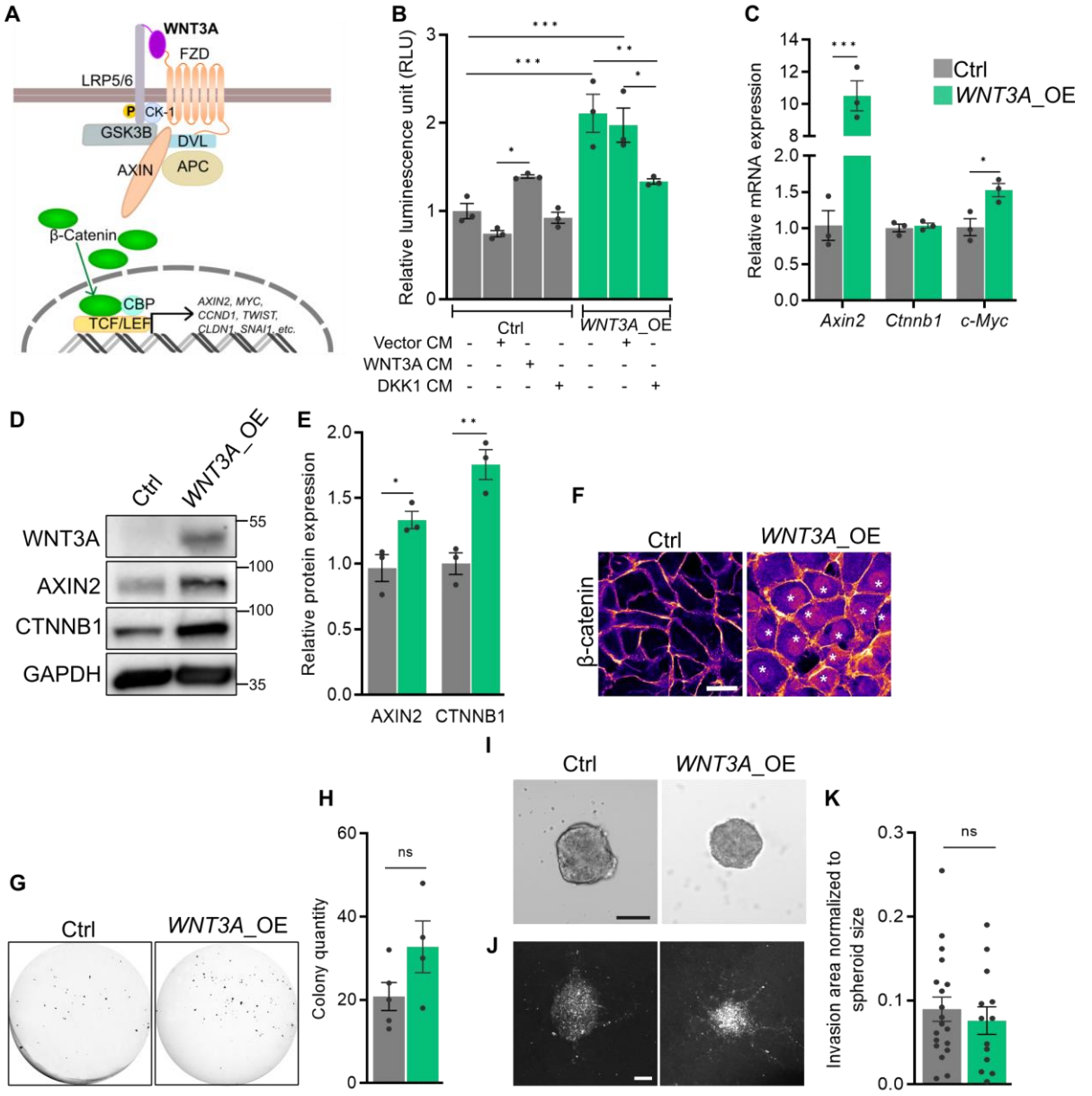

Figure 16. Wnt/β-catenin signaling activation through WNT3A over-expression in 2D in vitro models. A, *Schematic illustration of Wnt/β-catenin signaling activation through over-expression of WNT3A.* ***B,*** *Luciferase assay quantification of Wnt/β-catenin signaling in WNT3A overexpressing (WNT3A_OE) and control (Ctrl) cell lines. n = 3.* ***C,*** *Relative mRNA expression levels of several key genes of Wnt/β-catenin signaling. n = 3.* ***D-E,*** *Representative image (**D**) and relative quantification (**E**) of Western blot analyses of Wnt/β-catenin pathway genes in WNT3A_OE and Ctrl cells. n = 3.* ***F,*** *Representative confocal images of WNT3A_OE and Ctrl cells stained against β-catenin. Asterisks indicate nuclear β-catenin.* ***G-H,*** *Representative image (**G**) and quantification (**H**) of colonies formed in soft-agar assay of WNT3A_OE and Ctrl cells. n = 3.* ***I,*** *Representative bright-field images of Ctrl and WNT3A_OE spheroids.* ***J,*** *Representative confocal DiI images of Ctrl and WNT3A_OE spheroids in brain slices after 48h.* ***K,*** *Invasion area of Ctrl and WNT3A_OE spheroid after 48h. n = 13-19. Scale bar: 20 µm (**F**), 100 µm (**I, J**). Bars represent Mean ± SEM. One-Way ANOVA test, Tukey multiple comparison (**B**); Unpaired t-test (**C, E, H, K**); *p≤0.05, **p≤0.01, ***p≤0.001, ****p≤0.0001. Spheroid invasion quantification were blindly performed by Dr. Ekaterina Ivanova.*

2.1.4. Systemic hyper-activation of Wnt/β-catenin pathway leads to reduced differentiation of choroid plexus organoids

To study Wnt/β-catenin activation in a 3D *in vitro* model that shows a more complex spatio-temporal organization of the ChP, we first generated ChP organoids derived from hiPSC (human induced pluripotent stem cell) [125]. As previously reported, at maturation stage (around day 40-60), the organoids developed curled, veil-like structures histologically resembling ChP tissue (Fig. 17A). Mature organoids also developed fluid-filled structures called "cyst" (Fig. 17B). ChP organoids were confirmed to be positive for lineage markers as OTX2 and LMX1A (Fig. 17C), as well as several epithelial differentiation markers including the water channel AQP4 (Fig. 17C), the thyroid hormone transporter TTR and the cilia marker ARL13B (Fig. 17D). Electron micrographs confirmed the ultrastructural organization of ChP organoids, such as the interspersed existence of light and dark epithelial cells separated by tight junction, the abundance of mitochondria in cytoplasm, the presence of microvilli and multiple cilia on apical surface (Fig. 17E) [125].

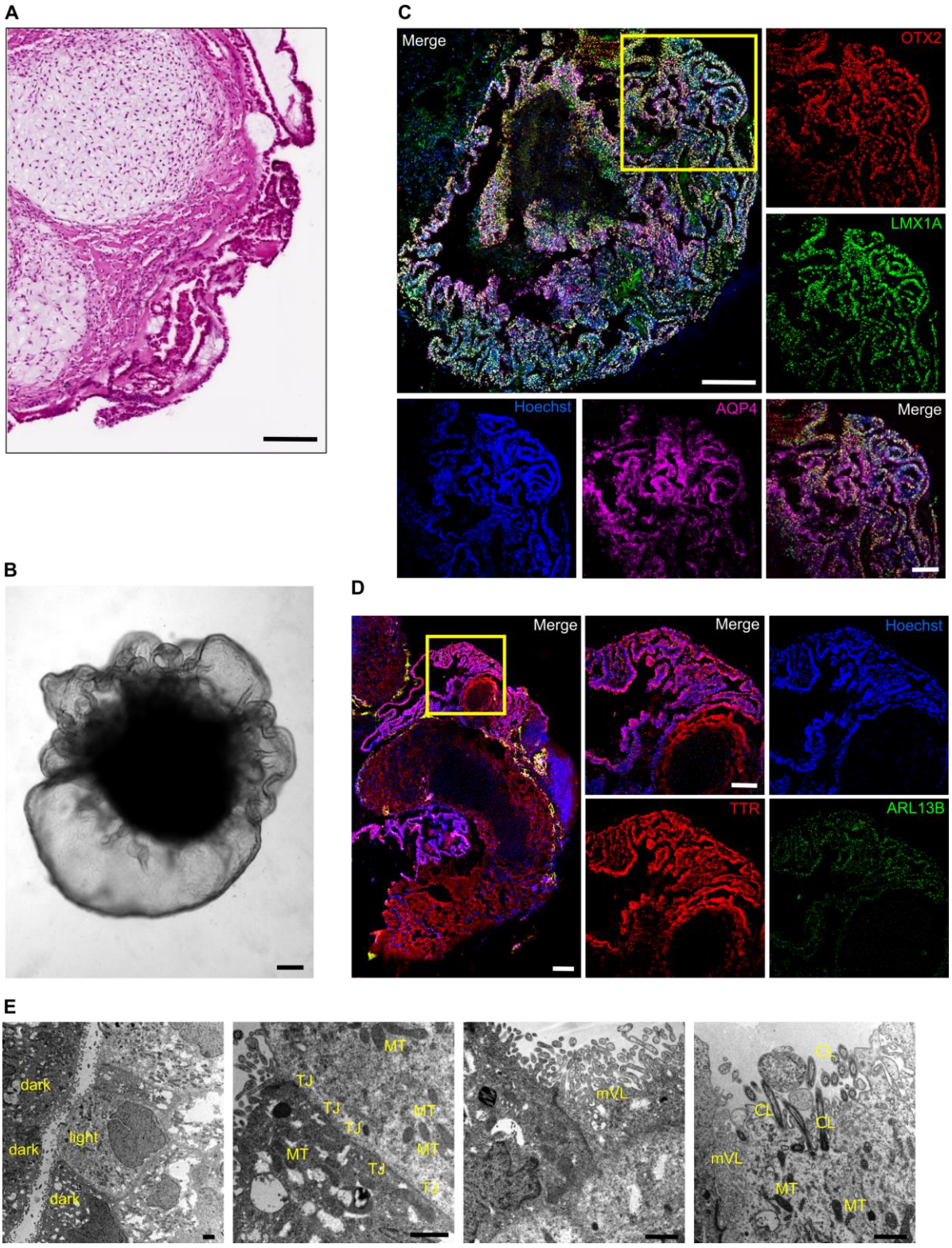

Figure 17. Generation of hiPSC-derived choroid plexus organoids. A, *Hematoxylin and eosin stained section of hiPSC-derived choroid plexus (ChP) organoid. Scale bar: 200 μm.* ***B,*** *Bright-field microscope image showing ChP organoid with the fluid-filled cavity (cyst). Scale bar: 200 μm.* ***C,*** *Representative immunofluorescence images of organoids stained against OTX2, LMX1A and AQP4. Scale bar: main: 200 μm, inset: 100 μm.* ***D****, Representative immunofluorescence images of ChP organoids stained against TTR and ARL13B. Scale bar: main: 200 μm, inset: 100 μm.* ***E****, Electron*

ultramicrographs showing basolateral invaginations of light and dark cells, tight junctions (TJ), mitochondria (MT), microvilli (mVL), cilia (CL). Scale bar: 1 μm. Figure 17A-D were provided by Dr. Ammar Jabali. TEM micrographs in Figure 17E were provided by Dr. Chiara Salio.

Next, to assess the effect of systemic Wnt/β-catenin signaling activation on organoids, I treated organoids from day 40 to 60 with 5 μM CHIR 99021 (CHIR) (Fig. 18A). CHIR inhibits the cytoplasmic negative regulator GSK3B (Fig. 18B) and is a highly potent activator of Wnt/β-catenin signaling [126]. CHIR is normally withdrawn from organoid culture medium from day 17 to attenuate Wnt/β-catenin signaling, mimicking *in vivo* ChP maturation phase [127], but was re-added from day 40 in treated organoids (Fig. 18A). CHIR-treated organoids developed larger area positive for ChP lineage marker OTX2 (Fig. 18C-D) with unchanged cell density (Fig. 18E) and proliferation rate as measured by KI67 staining (Fig. 18F-G). CHIR-treated organoids had reduced protein expression of several differentiation markers include TTR (Fig. 18H-I), AQP1 (Fig. 18J-K) and KIR7.1 (Fig. 18L). Organoids were also pooled, dissociated and evaluated for mRNA and protein expressions. Transcriptional analysis confirmed the decreased mRNA expressions of multiple differentiation markers (Fig. 18M) and demonstrated the increased transcriptions of Wnt/β-catenin pathway's genes: target gene *AXIN2*, nuclear effector *LEF1* and feedback regulator *DKK1* (Fig. 18N). Western blot analysis also showed increased protein levels of AXIN2 and CTNNB1 (Fig. 18O-P). Altogether, these data showed that CHIR treatment efficiently activated Wnt/β-catenin pathway in ChP organoids and led to less differentiated phenotype of OTX2+ ChP lineage cells. This result is rather similar to a previous study where the authors also used CHIR for constitutive activation of Wnt/β-catenin pathway in ChP organoids, leading to reduced expressions of all major differentiation marker, which was indeed caused by cell fate changing as Wnt/β-catenin signaling was hyperactivated since the very early stage of ChP induction [21]. In my study, because the Wnt/β-catenin pathway activation was induced at a later stage of ChP maturation, cells still maintain its ChP lineage, although with weaker differentiation features. The treated organoids did not have key characteristics of tumors (increased proliferation and cytoplasmic distribution of KIR7.1 [128]), but cells' less undifferentiated states have been linked to greater susceptibility to tumor development [129], [130], suggesting that a Wnt/β-catenin activation, even when not directly lead to tumor onset, has a promoting role in the tumorigenesis of ChP.

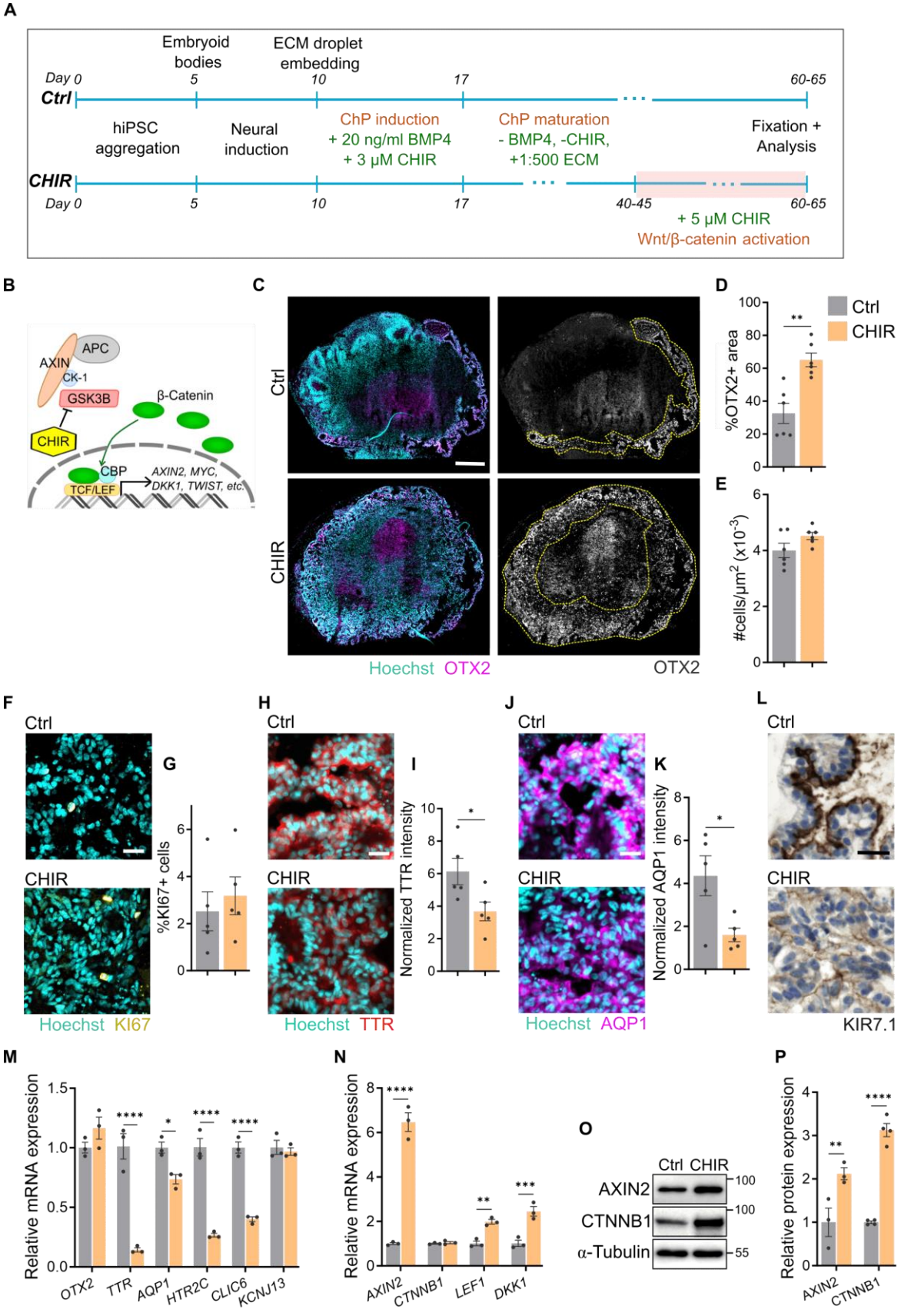

Figure 18. Systemic activation of Wnt/β-catenin pathway in hiPSC-derived choroid plexus organoids with CHIR99021 treatment. A, *Schematic illustration of ChP organoid generation*

procedure and CHIR99021 (CHIR) treatment. ***B,*** *Schematic illustration of the mechanism by which CHIR activates Wnt/β-catenin pathway.* ***C,*** *Immunofluorescence images of Ctrl and CHIR-treated ChP organoids stained against OTX2.* ***D,*** *Quantification of OTX2+ areas in Ctrl and CHIR-treated ChP organoids; n = 5.* ***E,*** *Quantification of cell density in OTX2+ areas of Ctrl and CHIR-treated ChP organoids; n = 5.* ***F-G,*** *Representative immunofluorescence images (**F**) and quantification of the percentage (**G**) of KI67+ cells in OTX2+ areas of Ctrl and CHIR-treated ChP organoids; n = 5.* ***H-I,*** *Representative immunofluorescence images (**H**) and quantification of the signal intensity (**I**) of TTR in OTX2+ areas of Ctrl and CHIR-treated ChP organoids; n = 5.* ***J-K,*** *Representative immunofluorescence images (**J**) and quantification of the signal intensity (**K**) of AQP1 in OTX2+ areas of Ctrl and CHIR-treated ChP organoids; n = 5.* ***L,*** *Representative images of Ctrl and CHIR-treated ChP organoids stained against KIR7.1.* ***M,*** *Relative mRNA expression levels of several key marker genes of ChP in dissociated Ctrl and CHIR-treated ChP organoids; n = 9 (each dot is a pooled sample of 3 organoids).* ***N,*** *Relative mRNA expression levels of several key genes of Wnt/β-catenin pathway in dissociated Ctrl and CHIR-treated ChP organoids; n = 9 (each dot is a pooled sample of 3 organoids).* ***O-P,*** *Representative image (**O**) and quantification (**P**) of relative protein expression levels of AXIN2 and CTNNB1 in Ctrl and CHIR-treated ChP organoids; n = 9 (each dot is a pooled sample of 3 organoids). Scale bar: 200 µm I, 25 µm (**F, H, J, L**). Bars represent Mean ± SEM. Unpaired t-test (**D, E, G, I, K**); Two-Way ANOVA test, Tukey multiple comparison (**M, N, P**); *p≤0.05, **p≤0.01, ***p≤0.001, ****p≤0.0001. The organoids were generated with technical support of Catello Guida.*

2.1.5. APC knock-out is sufficient to induce Wnt/β-catenin signaling activation and neoplasm formation in ChP organoids

Next, I attempted to create ChP neoplasm in organoid models through genetic engineering. Because *APC* mRNA expression was reduced in human tumors (Fig. 1B, 6F) and *Apc*_KO induced tumorigenic features in ChP cell line (Fig. 8), I knocked out the *APC* gene using CRISPR-Cas9 in the ChP organoid model. Matured ChP organoids (day 40-45) were transduced with lentivirus carrying either Cas9-mCherry (Ctrl) or sgRNA-Cas9-mCherry vectors to knock-out *APC* (*APC*_KO) and the organoids were kept in culture until day 60-65 for neoplasms to grow (Fig. 19A). Genetic engineering at the maturation stage provoked heterogeneous alterations, better simulating the process of tumorigenesis and resulted in a chimeric ChP organoid with a normal ChP area adjacent to a neoplastic area (Fig. 19B). Transduced ChP epithelial cells, usually located at the organoid periphery, were verified as mCherry positive (Fig. 19C). Analyses were carried out at mCherry+ areas, which were confirmed ChP lineage by OTX2 staining (Fig. 19D), showing increased cell density and cell proliferation as measured by KI67 staining (Fig. 19C-G).

Like human CPT, neoplastic ChP organoids had reduced expression of TTR (Fig. 19H) [131] and mainly contained unciliated and monociliated epithelial cells, which is

characteristic for epithelial transformation and increased aggressiveness [75], [78] (Fig. 19I). Histopathological analysis of the inward rectifying potassium channel KIR7.1, a specific pathogenic marker of CPTs [128], showed robust signal along the apical border with minimal cytoplasmic expression in Ctrl organoids; in contrast, *APC*_KO organoids were characterized by a strong KIR7.1 expression at both membrane and cytoplasm compartments (Fig. 19J), showing a resemblance to CPC. Methylation analysis [132] classified *APC*_KO organoids in the group "pediatric B" of supratentorial pediatric high-risk choroid plexus tumors [72] (MNP classifier score 0.41) (Fig. 19K).

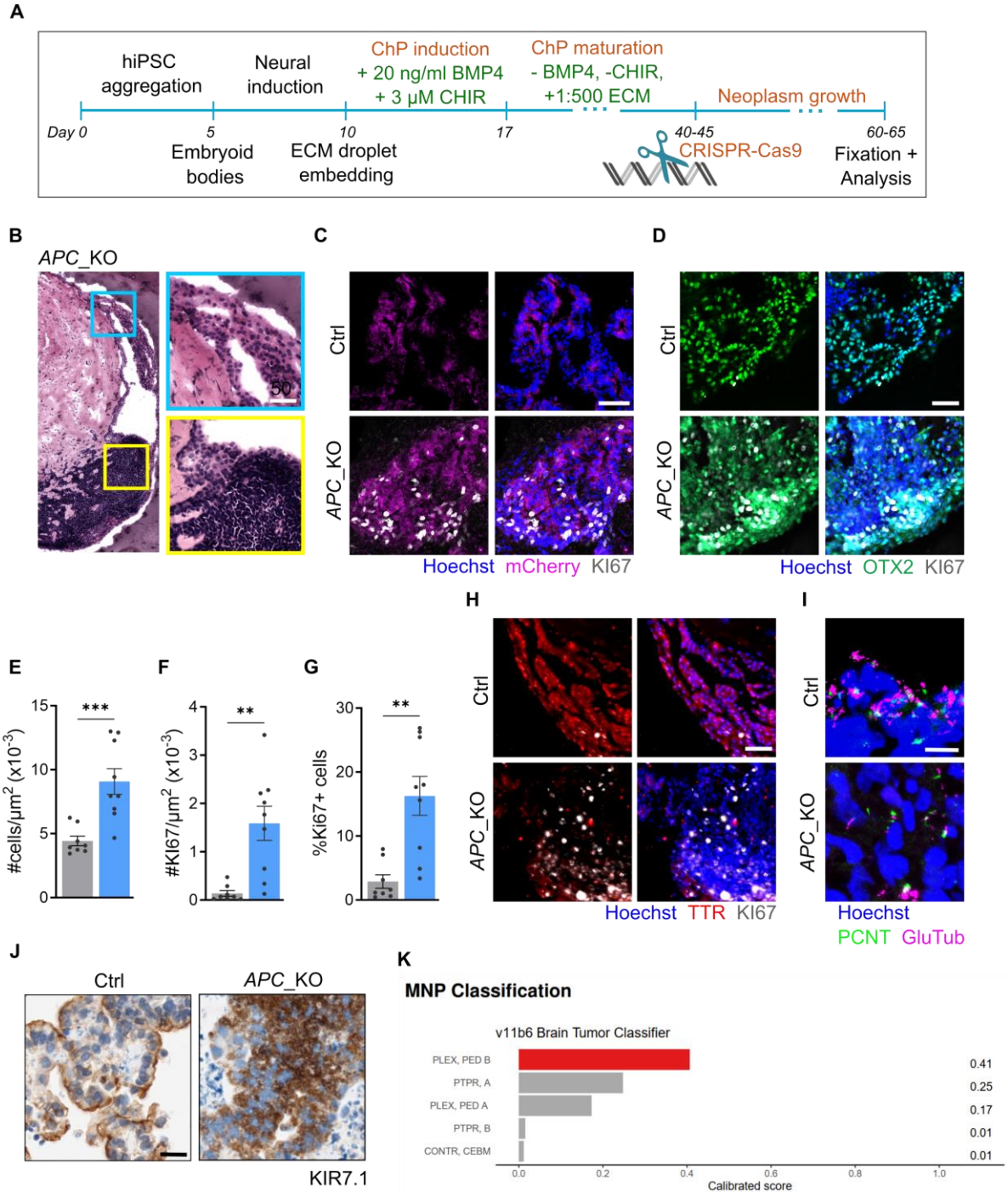

Figure 19. Loss of APC induces neoplasm in hiPSC-derived choroid plexus organoids. A, *Experimental procedure of the in vitro culture system to differentiate hiPSC into choroid plexus organoids and tumors.* ***B,*** *Hematoxylin and Eosin stained sections of choroid plexus (ChP) organoids with an area of APC_KO. Yellow square indicates healthy ChP epithelium. Cyan square shows a neoplastic region adjacent to healthy ChP. Scale bar: main: 200 μm, inset: 25 μm.* ***C,*** *Immunofluorescence images of Ctrl and APC_KO organoids with transduced areas expressing mCherry and stained against proliferation marker KI67.* ***D,*** *Immunofluorescence images of Ctrl and APC_KO organoids stained against OTX2 and KI67.* ***E,*** *Quantification of cell density in OTX2+ areas of Ctrl and APC_KO ChP organoids; n = 9.* ***F,*** *Quantification of KI67+ cell density in OTX2+ areas of Ctrl and APC_KO organoids; n = 9.* ***G,*** *Quantification of percentage of KI67+ cells in OTX2+ areas of Ctrl and APC_KO organoids; n = 9,* ***H,*** *Immunofluorescence images of Ctrl and APC_KO organoids stained against TTR and KI67.* ***I,*** *Immunofluorescence images of Ctrl and APC_KO organoids stained against cilia markers PCNT - basal bodies, GluTub - glutamylated tubulin/axonemes.* ***J,*** *Representative images of Ctrl and APC_KO organoids stained against KIR7.1.* ***K,*** *Molecular neuropathology (MNP) classification of APC_KO organoids based on DNA methylation profiling analysis. Scale bars: 50 μm (**B, C, D, H**), 10 μm (**I**), 20 μm (**J**). Bars represent Mean ± SEM. Unpaired t-test (**E, F, G**); *p≤0.05, **p≤0.01, ***p≤0.001, ****p≤0.0001. The organoids were generated with technical support of Dr. Ammar Jabali and Catello Guida. Figure 19J, K were provided by Dr. Christian Thomas.*

FAC-sorted mCherry cells from dissociated organoids were cultured for molecular analyses (Fig. 20A). RT-qPCR data showed a clear activation of Wnt/β-catenin signaling with significant increased mRNA levels of multiple well-known components: target genes (*AXIN2, DKK1, MYC*), receptors (*LRP6*), effectors (*CTNNB1, LEF1*) (Fig. 20B). Western blot result also showed that *APC*_KO cells expressed increased levels of AXIN2 and CTNNB1 (Fig. 20C, D). Additionally, immunofluorescence staining of CTNNB1 displayed a mis-localization in the cytoplasm compartment, showing disrupted morphology of transduced cells and indicating an increased stability of cytoplasmic CTNNB1 (Fig. 20E). These data confirm Wnt/β-catenin signaling activation in *APC*_KO organoid cells.

In summary, the activation of Wnt/β-catenin signaling, by depletion of APC, is sufficient to induce neoplasm formation in the 3D in vitro model of ChP organoid, which maintained ChP lineage, albeit with disrupted differentiation properties as observed in human and mouse CPT.

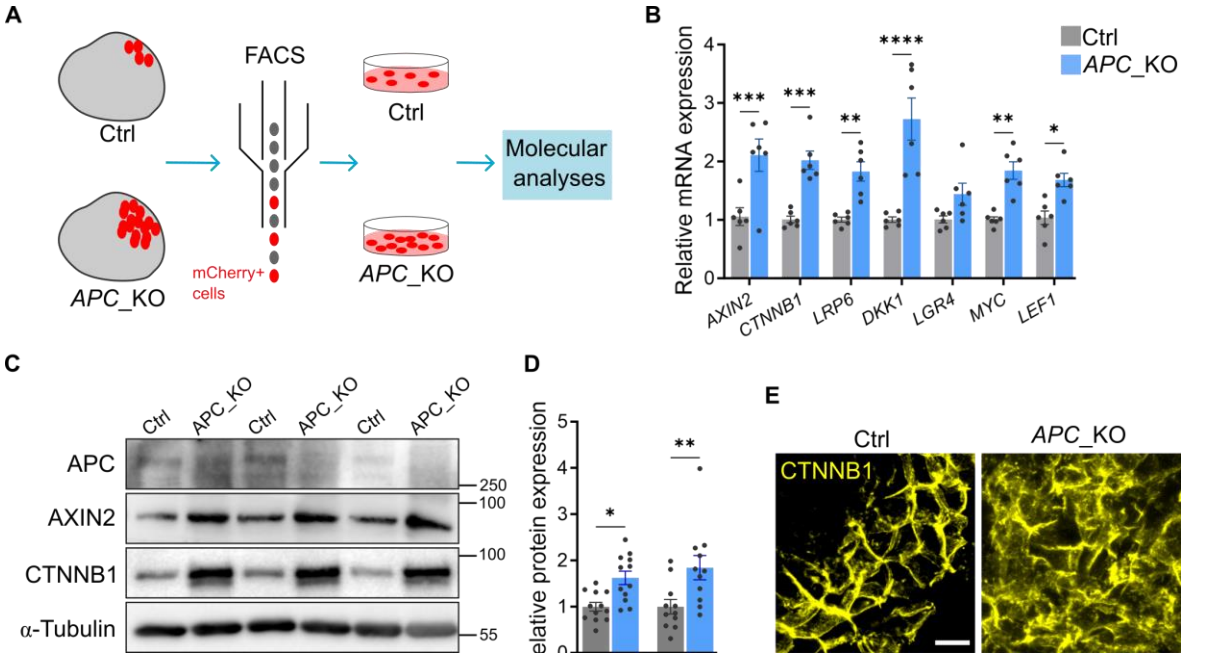

Figure 20. Wnt/β-catenin pathway is activated in APC_KO hiPSC-derived choroid plexus organoids. A, *Schematic illustration of the procedure to collect and analyze transduced cells from ChP organoids.* ***B,*** *Relative mRNA expression levels of several key genes in Wnt/β-catenin pathway in sorted Ctrl and APC_KO cells; n = 6.* ***C-D,*** *Representative image (**C**) and relative quantification (**D**) of protein expressions of APC, AXIN2 and CTNNB1 in sorted Ctrl and APC_KO cells; n = 12.* ***E,*** *Immunofluorescence images of Ctrl and APC_KO organoids stained against CTNNB1. Scale bars: 10 µm (**E**). Bars represent Mean ± SEM. Unpaired t-test (**B, D**); *p≤0.05, **p≤0.01, ***p≤0.001, ****p≤0.0001. The organoids were generated with technical support of Catello Guida.*

2.2. Discussions

This study has uncovered a high prevalence of genomic and transcriptomic alterations that involved multiple Wnt/β-catenin genes in human CPTs. I also demonstrated that CPT cells are dependent on Wnt/β-catenin signaling and that discrete activation of this pathway is sufficient to induce tumorigenesis in both 2D *in vitro* models and hiPSC-derived ChP organoids. Altogether, the data propose the activation of Wnt/β-catenin signaling as a crucial step for CPT tumor onset.

Developmentally, tChP derives from cortical hem whereas hChP originates from rhombic lip, both structures are well known to secrete multiple Wnt ligands [15]. In fact, at embryonic day (E) 10.5, before tChP emerges, *Wnt3a* is already expressed in the cortical hem; at E11.5, when tChP starts to organize structurally, the hem expressions of *Wnt3a*, *Wnt2b* and *Wnt5b* are upregulated, and at birth, when tChP is morphologically mature, hem becomes negative for Wnt ligands [15]. Consequently, tChP is significantly reduced in the *Wnt3a* KO mutants [16]. The hChP is more dependent on *Wnt5a* and *Wnt5a* ablation leads to reduction in size and disrupted architecture of hChP [19], [20]. On the contrary, the constitutive activation of Wnt/β-catenin from early embryogenesis is sufficient to change the cell fate of tChP in a murine model [21]. Similarly, high concentration treatment of hESC-derived ChP organoids with CHIR, a GSK3 inhibitor, during the morphogen induction stage, leads to loss of ChP epithelial identity and transformation to neuronal fate [21]. It is therefore conceivable that ChP development and morphogenesis depend on the timely activation of Wnt/β-catenin and its activation level. Thus, any disturbances of this balance likely derail the time course of normal development. On the other hand, CPT can be detected as early as the third trimester of pregnancy and nearly 50% of childhood CPT are diagnosed within the first year of life [94]. Attempts to model CPT by modulating key developmental pathways should, therefore, carefully consider the temporal dimension to create a tumor of ChP lineage.

Pathway analyses of human CPT transcriptomics data identified Wnt/β-catenin signaling as one of the activated pathways (Fig. 8A), resulting from expressional changes of multiple gene members. Interestingly, the majority of the upregulated genes were positive Wnt regulators, such as ligands and transmembrane receptors, whereas most of the downregulated genes were negative Wnt regulators, including *APC* (Fig. 8B). In

addition, analysis of SVs, SNVs and Indels variants revealed that genes involved in Wnt/β-catenin signaling were characterized by a high prevalence of variants predicted to be detrimental (Fig. 11, 12). Nevertheless, in line with previous genomic investigations [71], [72], [74], no single variant stood out as a driving mutation with both high frequency and pathogenic capacity. Although the initial trigger causing chromosomal instability is presently unknown, it is generally acknowledged that CPTs are characterized by large and frequent chromosomal instability events. Notably, aneuploidy is a remarkably consistent feature of many cancers whose drivers have not yet been identified. Thus, it has been suggested that certain synergies of chromosomal gains and losses may be sufficient to initiate a cancer without specific, targeted driver events [103]. Here, I suggest that Wnt/β-catenin activation could be a consequence of CPT genome-wide instabilities, which ultimately lead to the initiation and development of CPT. Interestingly, the activation of Wnt/β-catenin pathway has been proven causative of chromosomal instability through the involvement of multiple players, such as AXIN [133] and APC [134], [135] during mitosis. Therefore, the synergy between Wnt/β-catenin signaling and chromosomal instability could fuel the tumor onset.

Earlier studies demonstrated that two feedback regulators of Wnt/β-catenin signaling, *TWIST-1* and *WIF1*, are highly upregulated in CPPs [99], [118]. Knocking-down *TWIST-1* inhibits proliferation and invasion of ChP cell lines [99], whereas silencing *WIF1* neither modulates proliferation nor affects invasion [118]. Here, I demonstrated that the ablation of the negative regulator *APC* in 2D *in vitro* models was sufficient to induce oncogenic characteristics including increased anchorage-independent growth and brain parenchyma invasion (Fig. 13G-L). Importantly, the single genetic ablation of *APC* from hiPSC-derived ChP organoids was sufficient to induce ChP neoplasm formation (Fig. 19). These results suggest that the integrity of APC complex and its downstream regulatory target of β-catenin localization may play a strategic role in the onset of CPT. Immunohistochemical monitoring of β-catenin in human CPTs shows a lack of apparent homogenous nuclear localization; however, both CPPs and CPCs exhibit a clearly higher abundance of cytoplasmic β-catenin [118], [119] (Fig. 13B-E). β-catenin abundance and localization is a dynamic process, which depends on a multitude of transcriptional and translational controls, as well as the interaction of β-catenin with various transporters and signaling pathways, including Hippo and Wnt/PCP signaling [136]. Additionally, it

has been proved that the effect of Wnt/β-catenin pathway activation is dosage and time-dependent: high level of activation promotes pluripotency maintenance, while a mild stimulation could enhance differentiation [137], [138]. In a systemic disruption without genetic modification, Wnt/β-catenin activation by treating ChP organoids undergoing maturation stage with 5 μM CHIR leads to a less differentiated state of ChP epithelial cells, predisposing them to oncogenic transformation [129]. Overall, our data genuinely propose Wnt/β-catenin pathway as an important player in the onset of CPTs. In the future, it will be crucial to dissect how and when the molecular machinery responsible of the β-catenin stabilization in cytoplasm is disrupted during the initiation and progression of CPTs.

Due to its important role in tissue development and homeostasis, Wnt/β-catenin signaling has been an attractive yet challenging pathway to target for precision cancer therapy. Nevertheless, multiple clinical trials using different strategies to tame this pathway are currently ongoing. One of the rising prominent targets is the enzyme Porcupine (PORCN), which enables the secretion of WNT ligands through catalyzing palmitoylation. WNT974 is the first-in-class PORCN inhibitor; it has shown good tolerance and anti-tumor effect and is currently in Phase 1-2 clinical trials for the treatment of multiple solid tumors [120]. Our data showed that WNT974 exhibits anti-tumor activity on the CPP cell line by affecting cell proliferation and survival (Fig. 14). More extensive and intensive studies, using different tumor models including murine CPT [74], [75], [76], [77], [78], [79] and patient-derived ChP organoids and xenografts, when available, as well as the identification of cancer-specific Wnt signaling regulators, are needed to assess the effectiveness and feasibility of targeting this pathway for CPT treatment. In that respect, the recent development of receptor-specific WNT activators and inhibitors, including those for blood-brain-barrier [139], [140], [141], could open new opportunities for pharmaceutical intervention of CPT.

Despite the existence of several mouse models resembling some CPT features [74], [75], [76], [77], [78], [79], to our knowledge, only one CPT 2D *in vitro* model is currently available [142]. While organoid biobanks of patient-derived tumors are already established for many cancers [143], due the rarity of CPT and the lack of a common standard operative procedure, no similar resource is available for this cancer. Thus, the organoid model of CPT, described and utilized in our study, will be a highly valuable and

critical tool to accelerate both basic and translational research in CPT for the benefit of this neglected group of young patients.

3. The biogenesis and maintenance of nodal-like choroid plexus cilia

3.1. Results

3.1.1. Choroid plexus tissue expansion predominantly takes place near the ventricular wall throughout embryogenesis

In the adult mouse brain, the tChP is an unfolded thin bi-layered epithelium that spans a surface area of 4.9±0.7 mm^2 across the entire antero-posterior region of the lateral ventricles. The automatic segmentation of flat-mount adult tChP immunostained with the Trp73 antibody revealed that it is comprised of approximately 50000 cells, of which 95±3% are Trp73 positive (+) (Fig. 21A-C). Trp73 protein is a crucial regulator of multi-ciliogenesis [87], thereby confirming the multi-ciliated nature of the ChP epithelial cells. In order to determine the temporal origin of Trp73+ epithelial cells along the entire tChP, I injected a single EdU pulse to pregnant mice starting from early embryonic stages (E) 8.5 until postnatal days (P) 17 and subsequently assessed the distribution of Trp73+EdU+ cells at P25 (Fig. 21D). The P25 tChP exhibited three distinct spatial areas, each containing progenitors born in different time windows (Fig. 21E-F). The earliest progenitors were dispersed throughout the entire tissue, while the most recent wave of progenitors was located closer to the central nervous system parenchyma (Proximal Zone) (Fig. 21E-G), thereby indicating that the tChP is formed by a treadmill of cells generated during embryonic stages. The majority of tChP multi-ciliated cells (56%) were primarily generated as early as E10 showing that most, if not all, Trp73+ cells were born prior to the completion of embryogenesis (Fig. 21G).

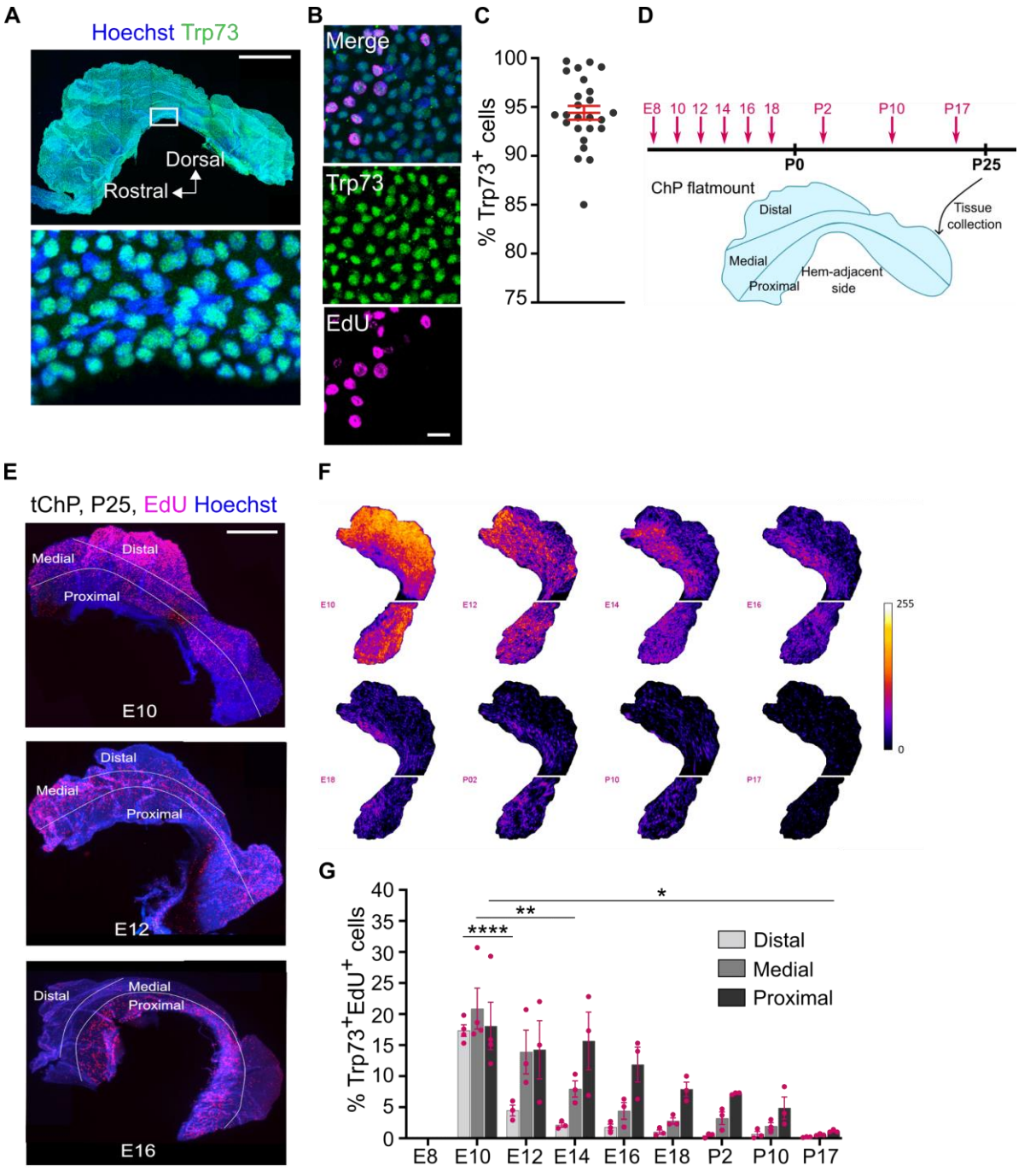

Figure 21: Treadmill of proliferative cells into choroid plexus. A, *Flatmount P25 telencephalic (t) choroid plexus (ChP) labeled with Trp73.* ***B,*** *Representative image of P25 tChP labeled with Trp73 and EdU.* ***C,*** *Quantification of the percentage of Trp73+ cells in P25 tChP.* ***D,*** *Schematic representation of the single EdU injection experiment.* ***E,*** *P25 tChP flatmounts labeled with EdU at the indicated embryonic ages and divided into 3 zones.* ***F,*** *Reassembled and animated P25 ChP flatmounts, pseudocolor represents EdU injected at 8 developmental time points.* ***G,*** *Quantification of Trp73+EdU+ cells in each zone at P25 after one single EdU injection at the indicated age (n = 3 per age). Scale bar: 700 µm (A, E), 15 µm (B), One-way ANOVA, *p≤0.05, **p≤0.01, ***p≤0.001, ****p≤0.0001. Bars represent mean ± SEM. Figure 21 was provided by Dr. Nathalie Spassky's group.*

To further explore the dynamics of cell proliferation during the development of ChP, I mapped the distribution of actively dividing cells along the axis of the ChP using double S-phase labeling. Pregnant female mice were injected with both EdU and BrdU 24 hours apart, and embryos were collected 24 hours after the final injection (Fig. 22A). This experiment mainly focuses on the tChP. Analysis of tissue size revealed that the length of the tChP increased by approximately 2-fold every 48 hours from E12.5 to E16.5, but the growth rate slowed down, as the length only increased by 1.5-fold, from E16.5 to E18.5 (Fig. 22B). The number of positive cells was quantified in each segment of increased tissue after every 48 hours (Fig. 22C). Overall, the only stage when proliferative cells distributed along all four quartiles was E12.5 (Fig. 22D); since E14.5, the number of proliferative cells gradually decreased along the tChP axis (Fig. 22E). The percentage of EdU+ and BrdU+ cells declined over time and along the tChP tissue axis (Fig. 22F-H). Indeed, within the first 0.25 mm tissue from ChP root, up to 150-200 cells were proliferating when analyzed at E12.5, followed by a significant drop to around 50 cells at E14.5 and further decline to under 10 cells at E18.5 (Fig. 22F, G). The number of double dU+ (EdU+ and BrdU+) showed a similar trend (Fig. 22I). To then infer the proportion of dividing cells re-entering cell cycle, I ratioed the number of double dU+ over EdU+ cells. Between E10.5 and E12.5, around 70% proliferating cells re-entered the cell cycle; this percentage was steady until E16.5 and then decreased to around 20% at E18.5 (Fig. 22J). Although recurrent proliferative cells represent a small minority of tChP epithelial cells since E14.5 (Fig. 22I), they were distributed along the tChP length, suggesting that some cells located at the tissue medial and distal regions retain proliferative ability (Fig. 22K).

In summary, our data shows that ChP is generated by a treadmill of dividing cells, the proliferative ability of which decreases gradually along temporal development and spatial dimension of the tChP.

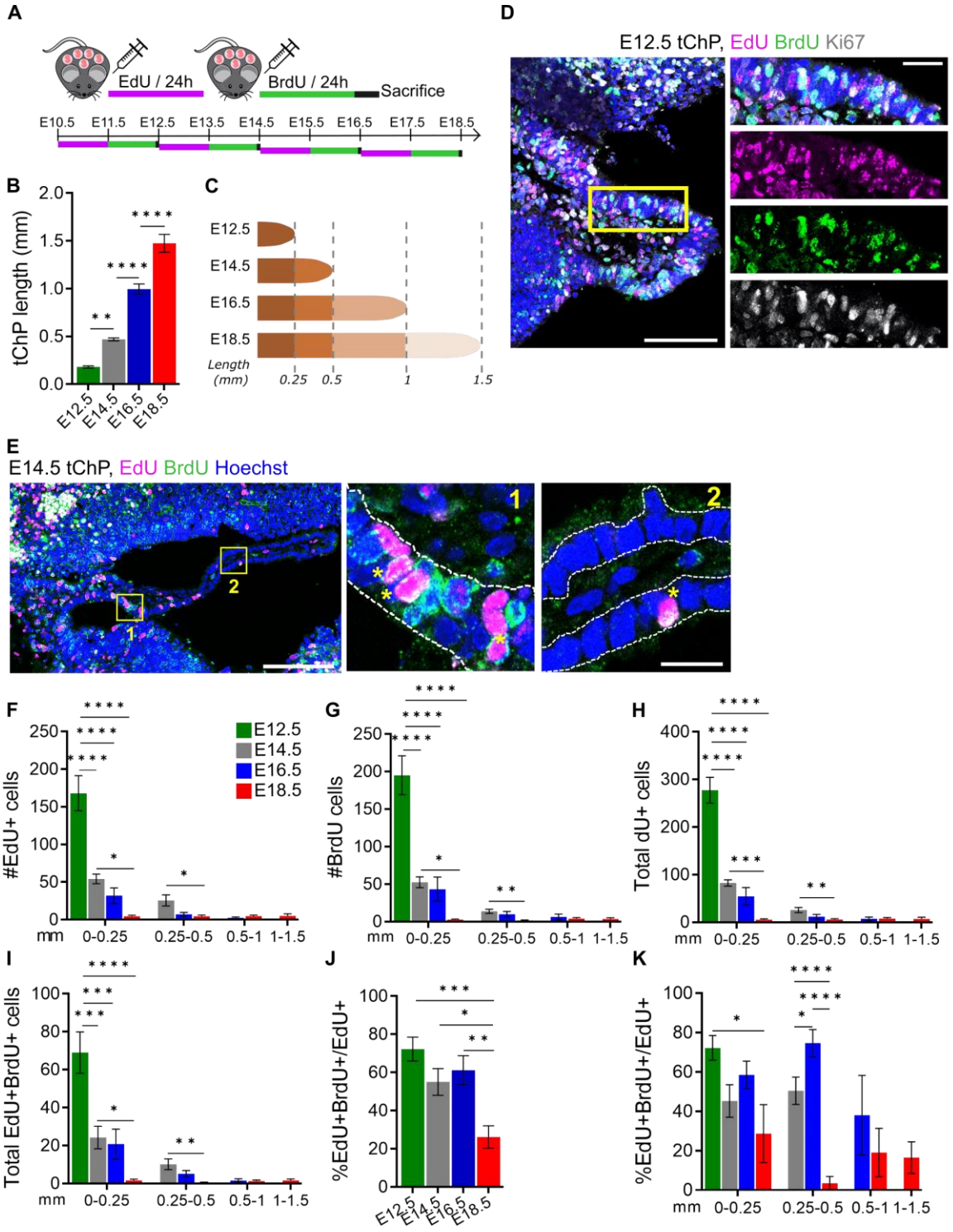

Figure 22: Double S-phase labeling deciphers the spatial temporal dynamics of ChP proliferation. A, *Schematic representation of double S-phase experiment procedure.* ***B,*** *Increased length of the tChP during embryogenesis.* ***C,*** *Schematic layout of tChP length increase throughout embryogenesis.* ***D,*** *E12.5 tChP sections were triple stained against EdU, BrdU and Ki67.* ***E,*** *E14.5 tChP sections were triple stained against EdU, BrdU and Ki67. Insets feature ChP proximate to (1) or distant from (2) the ventricular wall. Asterisks (*) indicate double positive EdU+BrdU+ cells.* ***F,*** *The numbers of EdU+ cells along tChP length in every increased tissue segment after 48 hours.* ***G,*** *The numbers of BrdU+ cells along tChP length in every increased tissue segment after 48 hours.* ***H,*** *The*

numbers of EdU+ and/or BrdU+ cells along tChP length in every increased tissue segment after 48 hours. ***I,*** *The numbers of double positive (EdU+ and BrdU+) cells along tChP length in every increased tissue segment after 48 hours.* ***J,*** *The percentage of double positive cells over EdU+ cells at each of the studied embryonic age.* ***K,*** *The percentage of double positive cells over EdU+ cells along tChP length in every increased tissue segment after 48 hours. Scale bar: 100 µm (D, E: overview), 30 µm (D: insert), 10 µm (E: insert). Bars represent mean ± SEM. One-Way ANOVA (B, J), Two-way ANOVA (F-I, K). *p≤0.05 **p≤0.01, ***p≤0.001, ****p≤0.0001.*

3.1.2. Ciliogenesis as a spatial and temporal footprint of choroid plexus epithelial cell development and maturation

We next correlate cellular proliferation and maturation by mapping the spatial organization of multiple markers, including Ki-67 – cell proliferation, E-Cadherin - epithelial differentiation, and cilia markers including γ-tubulin (basal bodies) and acetylated α-tubulin (axoneme). At E12.5, early stage of morphogenesis for tChP [144] - nearly all cells are proliferating, as shown by the labelling of Ki-67 (also consistent with EdU labeling experiments in Fig. 21 and 22), while E-Cadherin signal was barely detectable (Fig. 23A). At this stage, immunostaining for cilia showed numerous basal bodies but no axoneme along the whole ChP length (Fig. 23B), suggesting that at this stage, ChP consists of proliferative, undifferentiated progenitors.

At later stages, from E14.5 for tChP, E-Cadherin signal became more visible, creating distinct areas of cells at different developmental stages. In areas adjacent to cortical hem – progenitor pools of tChP, most cells were positive for Ki-67 and had weak, disrupted E-Cadherin (area 1), showing that these cells were either still actively dividing or had just exited cell cycle [145] (Fig. 23C, area 1). This area was also characterized by multiplied basal bodies; however, the majority of cells were not ciliated yet (Fig. 23D, area 1). Conversely, the distal epithelial area was almost negative for Ki-67 and strongly positive for E-Cadherin, indicating these cells had long been in G0 phase and were establishing characteristics of differentiated cells (Fig. 23C, area 2). Most cells here were also already multi-ciliated (Fig. 23D, area 2). Similar patterns of proliferation and differentiation/ciliation was true also for hChP. which emerges earlier than tChP at E11.5 [144].

All together, these results showed that, unlike ependymal cells which are only ciliated at neonatal ages [146], ChP becomes multi-ciliated soon after cells are committed (E12.5 in

hChP and E14.5 in tChP). ChP ciliogenesis regionalization is closely related to cell proliferation and maturation.

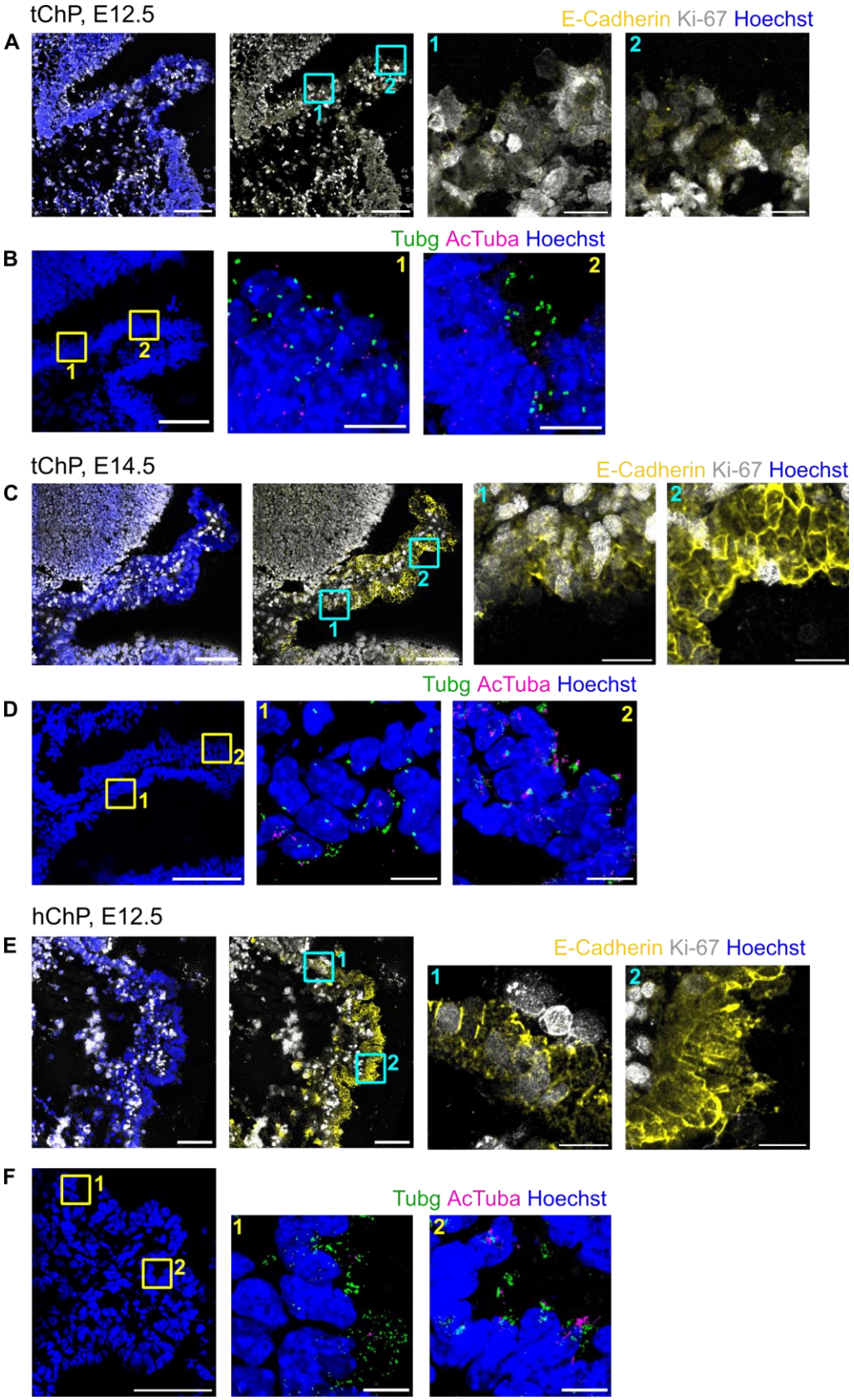

Figure 23: Ciliogenesis state of the choroid plexus epithelial cells correlates with cellular differentiation. A, *Telencephalic (t) choroid plexus (ChP) at E12.5 was stained against E-cadherin and Ki67.* ***B,*** *E12.5 tChP was stained against γ-Tubulin (Tubg) and acetylated tubulin (AcTuba).* ***C,*** *E14.5 tChP was stained against E-cadherin and Ki67.* ***D,*** *E14.5 tChP was stained against (Tubg) and acetylated tubulin (AcTuba).* ***E,*** *Hindbrain (h) choroid plexus (ChP) at E12.5 was stained against E-cadherin and Ki67.* ***F,*** *E12.5 hChP was stained with Tubg and AcTuba. Inset boxes feature ChP proximate (1) or distant (2) from the ventricular wall, respectively. Scale bars: overview: 100 µm, inset: 10 µm.*

3.1.3. Choroid plexus cilia are assembled in a highly organized multi-step process matching cellular maturation

We proceeded to characterize one of the pivotal steps in the process of multiciliogenesis, namely centriole amplification. This was accomplished by both immunostainings and TEM ultrastructural analysis of serial sections of immature tChP cells. Our investigation revealed that cells involved in the process of centriole amplification, as indicated by the presence of SAS-6 and DEUP1 antibodies, which label procentrioles and deuterosomes, respectively, were abundantly present from E12 (Fig. 24A). Additionally, a few scattered multi-ciliated cells were also observed, indicating that cell differentiation and maturation occur rapidly in these cells (Fig. 24B). The process of centriole amplification in these cells follows similar phases as those previously characterized in ependymal cells [88], but still with significant differences. The amplification phase commenced with the formation of Cen2GFP and SAS-6 structures in the centrosomal region, which is likely indicative of procentrioles forming around parental centrioles (Fig. 24C, early amplification). No clear staining with DEUP1 was observed during this early amplification phase, suggesting that deuterosome formation may occur slightly later (Fig. 24C, early amplification). Subsequently, small dense structures resembling pro-deuterosomes, with irregular shapes and containing one or two procentrioles, could be observed at the TEM level in close proximity to the parental centrioles (cell #1 in Fig. 24D; early amplification phase). Deuterosomes, averaging at a quantity of 4 per cell (with a range of 2-6), were initially loaded with procentrioles (2-6 per deuterosome, mean: 4). Subsequently, they underwent enlargement while remaining in the centrosomal region during the late amplification phase (Fig. 24C). During the growth phase, procentrioles dispersed across cells' apical surface (Fig. 24C, cell #2 in Fig. 24D) and increased their size significantly (Fig. 24F, G). Throughout the disengagement phase, centriole splitting occurred while still

attached to a deuterosome (Fig. 24C, cell #3 in Fig. 24D), followed by axonemal growth. At this stage, some centrioles surrounding the parental centrioles remained visible (cell #3 in Fig. 24D). Mature tChP multi-ciliated cells contained a range of 15-42 ciliated basal bodies (mean: 24) that were produced through centriolar and deuterosome-dependent pathways in an equivalent ratio. This contrasts with ependymal cells, where the majority of centrioles grow on deuterosomes [88]. Of note, the basal bodies were initially dispersed across the entire apical surface and gradually converged to form a tightly packed cluster of approximately 2 μm^2 during postnatal stages. This tightly packed cluster of basal bodies occupies less than 3% of the total apical surface of tChP cells (Fig. 24C, H, J), which is markedly different from the ependyma, whose basal bodies occupy around 20% of the apical surface [147].

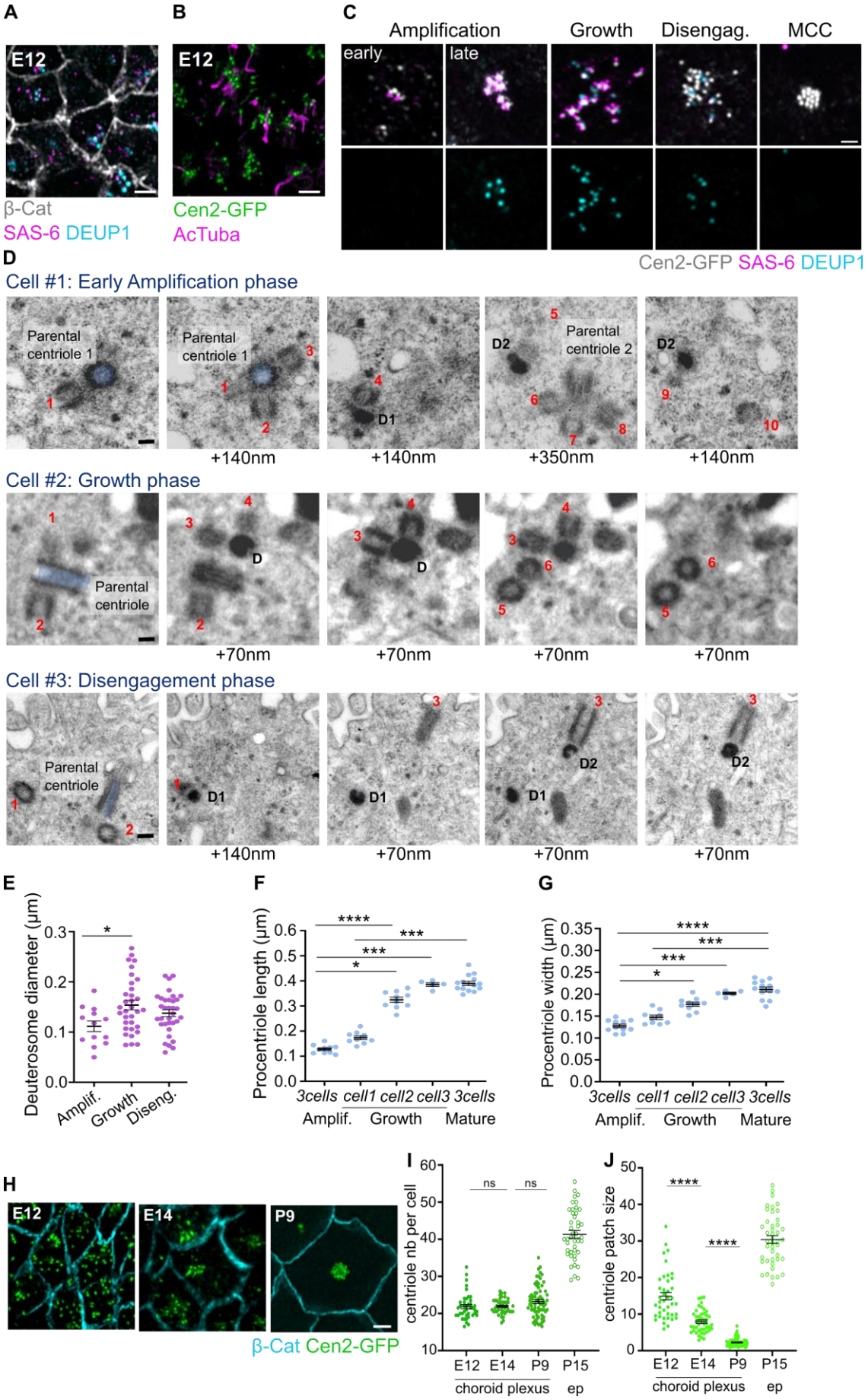
A
E12
β-Cat
SAS-6 DEUP1
B
E12
Cen2-GFP
AcTuba
C
Amplification
Growth
Disengag.
MCC
early
late
Cen2-GFP SAS-6 DEUP1
D
Cell #1: Early Amplification phase
Parental centriole 1
Parental centriole 2
D1
D2
+140nm
+350nm
Cell #2: Growth phase
Parental centriole
D
+70nm
Cell #3: Disengagement phase
E
Deuterosome diameter (µm)
Amplif.
Growth
Diseng.
F
Procentriole length (µm)
3cells cell1 cell2 cell3 3cells
Amplif. Growth Mature
G
Procentriole width (µm)
H
E12
E14
P9
β-Cat Cen2-GFP
I
centriole nb per cell
ns
E12 E14 P9 P15
choroid plexus
ep
J
centriole patch size
****
choroid plexus

Figure 24: Centriole amplification in telencephalic choroid plexus epithelial cells. A, *Wholemount E12 ChP triple stained against beta-catenin (β-Cat), SAS-6 and DEUP1.* ***B,*** *Wholemount ChP from E12 Cen2-GFP mice stained against acetylated tubulin (AcTuba).* ***C,*** *Cen2-GFP flat-mount tChP at E15.5 stained against SAS-6 and DEUP1 showing each phase of centriole amplification.* ***D,*** *Serial transmission electron microscopy (TEM) sections spanning the parental centrioles and deuterosomes of tChP cells at early amplification (Cell #1), growth (Cell #2) and disengagement (Cell #3) phases.* ***E,*** *Measurement of deuterosome diameter at each phase.* ***F,*** *Measurement of procentriole length at each phase.* ***G,*** *Measurement of procentriole width at each phase.* ***H,*** *Wholemount ChPs from Cen2-GFP mice were stained against β-Cat at E12, E14 and P9.* ***I,*** *Quantification of the number of centrioles per cell at different developmental time points.* ***J,*** *Quantification of centriole patch size at different developmental time points. Scale bar: 2 µm (**A, B, C, H**), 280 nm (**D,** Cell #1, Cell #2), and 320 nm (**D,** Cell #3). Bars represent mean ± SEM. Kruskal-Wallis test (**E, F, G, I, J**). n = 3 animals. *p≤0.05, **p≤0.01, ***p≤0.001, ****p≤0.0001. ns: not significant. Figure 24 was provided by Dr. Nathalie Spassky's group.*

Axoneme formation was best illustrated along E16.5 tChP, which showed a clear gradient of differentiation along its axis. Cells amplifying centrioles were ciliated at multiple stages, ranging from a single cilium (sc) to disengagement phase of multi-ciliated cells (mcd) and fully developed multi-ciliated cells (mcc), coexisted along the tissue length (Fig. 25A). These cilia configurations were also confirmed through ultrastructural analysis using TEM (Fig. 25B). At E16.5, the majority of the tChP was predominantly occupied by mcd cells (40% ciliated cells), while a gradual transition from mcd to the mature mcc was observed in the more distal part of the tChP (Fig. 25A, C).

Quantification of the proportion of ciliated cells throughout embryonic development showed that, since E14.5, at least up to 70% - 80% ChP epithelial cells contain multiple basal bodies, confirming that cells were committed to be multi-ciliated (Fig. 25D). However, only 40% - 50% of these cells carried clear axonemes at E14.5 (Fig. 25E). By the age of E16.5, up to 80% of ChP epithelial cells were multi-ciliated. This proportion was generally maintained until birth (Fig. 25E). Of note, the average length of the axoneme was constant during embryonic development and ranged from around 0.9 to 1.3 µm (Fig. 25F), which is considerably shorter than ependymal (8 µm) and tracheal cilia (4-7 µm) [148]. Multi-ciliogenesis in hChP takes place following a similar process (Fig. 25D-F).

Serial TEM reconstruction of mcc cilia shows 9+0 axoneme structure with regularly ordered microtubule doublets all along the axoneme shaft (Fig. 25G, H). Interestingly, basal bodies of ChP cells carried up to 6 basal feet (also known as subdistal appendages),

canonical structures that connect basal bodies to the microtubule cytoskeleton [149] (Fig. 25G, I). Ependymal motile cilia are characterized by one basal foot per basal body that is crucial to coordinate ciliary beating [149], whereas primary cilia usually contain nine basal feet [150]. The presence of 6 basal feet denotes a unique feature of ChP cilia.

To further characterize the mcc cilia, I assessed the presence of post-translational modifications (PTMs) of tubulin, as these modifications are closely correlated with cilia length and stability [151]. Double staining of E16.5 cilia with acetylated a-tubulin (AcTuba) and the structural microtubule marker Tubulin alpha 4a (Tub4a) or glutamylated tubulin (GluTub, GT335) demonstrated that all cilia contained both PTM types along the whole axoneme (Fig. 25J, K). These results differ from previous reports, which suggested that AcTuba covers a longer length of the axoneme, including the ciliary tip, compared to GluTub, which is located more at the base of the axoneme [151]. Despite the relatively short length of the ChP cilia, I observed glycylated tubulin present (Fig. 25L). However, the distribution of glycylated tubulin was not uniform at E16.5 (Fig. 25L, M), suggesting that this PTM might primarily play a role in cilia maturation rather than cilia formation [152]. Our data provide evidence that ChP axonemes possess multiple PTMs and that these modifications occur post-translationally from the initial stages of their formation.

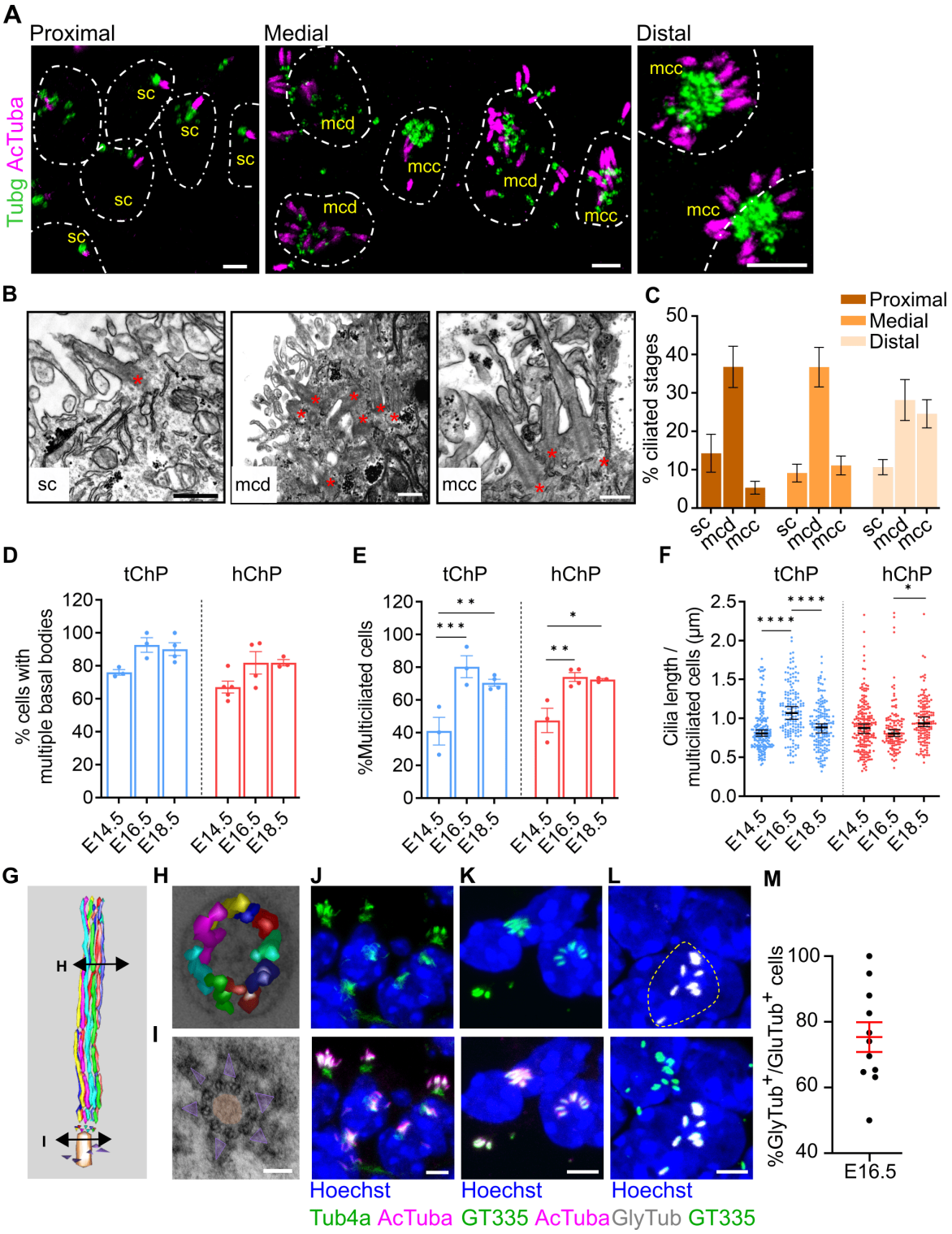

Figure 25: Multi-step ciliogenesis process in ChP epithelial cells. A, *E16.5 sagittal brain sections of tChP stained against γ-Tubulin (Tubg) and acetylated α-tubulin AcTuba. Multiple cilia configurations were identified along the tChP according to their distance to the ventricular wall. sc: single cilium; mcd: multi-ciliated, disengaged basal bodies; mcc: multi-ciliated, clustered basal bodies.* ***B,*** *Transmission electron microscopy (TEM) of E16.5 ChP epithelial cells showing all types of ciliated cells: sc, mcd and mcc.* ***C,*** *Histograms of the distribution of cells at different ciliated stages of tChP at E16.5. n = 4 embryos.* ***D,*** *Quantification of the percentages of cells containing multiple basal bodies of tChP and hChP at different developmental time points.* ***E,*** *Quantification of the percentages*

of multiciliated cells of tChP and hChP at different developmental time points. ***F,*** *Measurement of cilia length of tChP and hChP at different developmental time points.* ***G,*** *TEM 3D model showing the reconstruction of tubulin doublets along the entire length of E15 tChP cilium.* ***H,*** *Cross section of the cilium showing circular organization of tubulin doublets.* ***I,*** *Basal body cross section showing 6 basal feet (purple triangle).* ***J,*** *P0 tChP sections stained against Tubulin alpha 4a (Tub4a) and AcTuba.* ***K,*** *E16.5 tChP sections stained against glutamylated tubulin (GluTub) and AcTuba.* ***L,*** *E16.5 tChP sections stained against glycylated tubulin (GlyTub) and GluTub. Dotted line indicates region of interest showing GluTub-positive/GlyTub-negative cilia at E16.5.* ***M,*** *Quantification of percentage of cells carrying cilia which are GluTub-positive/GlyTub-negative at E16.5. Scale bar: 20 µm (**A**), 500 nm (**B**), 3 µm (**J, K, L**). Bars represent mean ± SEM, n = 3 mice per age (**C, D, E, M**). Bars represent Median ± 95% CI, n = 130-200 cilia (from 3 mice) (**F**). One-way ANOVA (**C**), Two-way ANOVA (**D, E**), Kruskal-Wallis (**F**). *p≤0.05, **p≤0.01, ***p≤0.001, ****p≤0.0001. Image acquisition for Figure 25A was performed by Dr. Elisa D'Este. Image acquisition for Figure 25B was performed by Dr. Chiara Salio. Figure 25G-I were generated by Dr. Nathalie Spassky's group.*

Notably, a small subgroup of sc cells with a solitary cilium were uniformly dispersed along the tChP (Fig. 25C). These cells existed amidst neighboring cells carrying multiple cilia (Fig. 26A), and their presence was confirmed through serial transmission electron microscopy (TEM) reconstruction analysis (Fig. 26B, C). The average length of the axonemes of these single cilia was approximately 2-3 µm (Fig. 26D), which is longer than the axoneme length of ChP multi-ciliated cells. To determine whether the sc configuration was temporary, I examined cilia configurations at E16.5 and P0. Compared to E16.5, there was a substantial transition to the mcc configuration at P0; however, the proportion of sc cells with a single cilium remained similar at both ages at around 5% (Fig. 26E). This indicates the co-existence of multiple cilia configurations in the differentiated ChP.

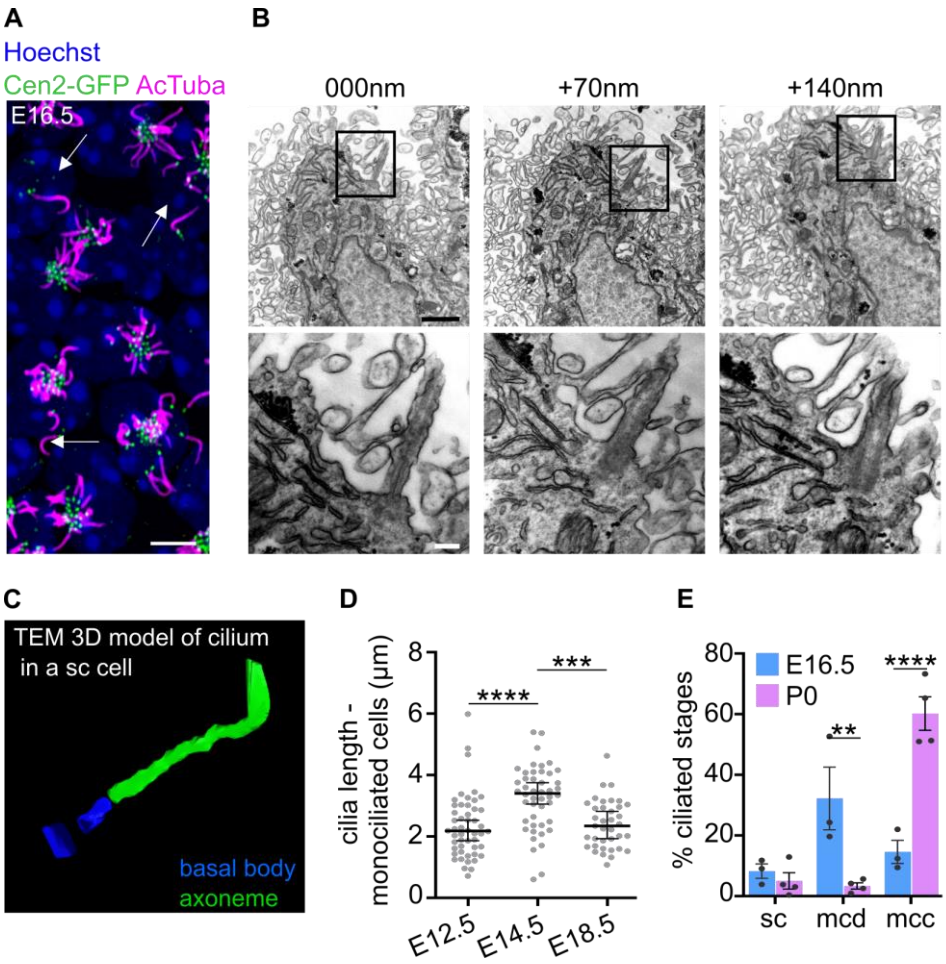

Figure 26: Choroid plexus also contains a monociliated epithelial cells. A, *Wholemount tChP of Cen2-GFP mice stained against acetylated tubulin (AcTuba). Arrows indicate monociliated cells.* ***B,*** *Transmission electron microscopy (TEM) serial reconstruction showing monociliated cells at E16.5 ChP.* ***C,*** *TEM 3D model of a monociliated cell showing 1 basal body and 1 axoneme.* ***D,*** *Quantification of cilia length in ChP monociliated cells at embryonic indicated age. Each dots represent a single cilum. n = 37-50 cilium from 3 mice per age.* ***E,*** *Quantification of different type of ciliated stages at E16.5 and P0 ChP. n = 3 mice per age. Scale bar: 70 µm (**A**), overview 1 µm, inset 200 nm (**B**). Bars represent mean ± SEM. Kruskal-Wallis test (**D**), Two-Way ANOVA (**E**). *p≤0.05, **p≤0.01, ***p≤0.001, ****p≤0.0001. Figures 26A, C were provided by Dr. Nathalie Spassky's group. TEM serial reconstruction (Figure 26B) was performed by Dr. Chiara Salio.*

3.1.4. Choroid plexus carries atypical multi-cilia with both motile and primary features

The nature of the ChP epithelial cilia has been a controversial and under-studied topic [80]. By utilizing publicly available single-nucleus RNA (snRNA) data of ChP epithelial cells at three distinct developmental stages (E16.5, P120, and P600) [6], I selectively extracted genes associated with cilia and identified the expressions at E16.5 of regulators of multiciliogenesis, such as *Mcidas* and *Ccno* [80], as well as numerous components of cilia motility programs, including Dynein arms, Central pairs, Nexin-Dynein regulatory complex (N-DRC), and genes related to flagella structure and sperm movement (Fig. 27A, B). RT-qPCR data from E16.5 ChP homogenates confirms the expression of some of these key cilia motility-related genes (Fig. 27C). This transcriptomic profile, coupled with the fact that ChP epithelial cells are multiciliated, implies that the ChP, similar to the ependyma, trachea, and fallopian tube, possesses motile cilia [80]. Interestingly, the majority of these genes displayed significant downregulation at postnatal stages compared to E16.5, which is in line with the previously reported gradual decline of cilia motility [93], suggesting that cilia motility may serve different functions during embryonic and adult stages.

Next, I verified the protein expressions and localizations of a subset of candidates by immunofluorescence. Our analysis focused on GAS8, a constituent of the nexin-dynein regulatory complex (N-DRC) [153], and the coiled-coil containing protein CFAP53, recognized as a crucial regulator of ciliary motility [154] (Fig. 27D-F). Our findings revealed that the majority of cilia were positive for GAS8, which was predominantly localized along the axoneme shaft, as indicated by co-labeling with GluTub (Fig. 27D). Intriguingly, I observed an exclusive localization of CFAP53 at the basal bodies (Fig. 27E, F), aligning with earlier reports on its distribution in nodal cilia [154]. On the contrary, CFAP53 is also expressed along the axoneme of the canonical 9+2 ependymal and tracheal cilia [154].

Nonetheless, when juxtaposed with the typical structure of motile cilia (Fig. 27A), our TEM ultrastructural examination predominantly showed a 9+0 axonemal tubulin arrangement with frequent appearance of a central, yet unidentified, electron-dense (ed) structure (Fig. 27G, white arrow), along with the possible presence of outer dynein arms (Fig. 27G, red arrows). These observations suggest that, despite not having 9+2

configuration, the ChP epithelial cilia could possibly be motile. Notably, the electron-dense structure showed a fragmented pattern along the axoneme shaft and is uncharacterized with respect to its composition and function. Analyses of serial sectioning TEM at both prenatal (E15.5) and postnatal (P45) stages showed that the conventional 9+0 cilia only accounted for around 10%-20% cilia and the majority of cilia had the 9+ed tubulin structure (Fig. 27H).

Altogether, our data shows that embryonic ChP multi-ciliated cells contain multiple nodal-like cilia presenting features of both primary and motile cilia, which includes the ultrastructure of 9+0 and 9+ed tubulin axoneme, as well as the expression and spatial distribution of genes and proteins associated with cilia beating machinery.

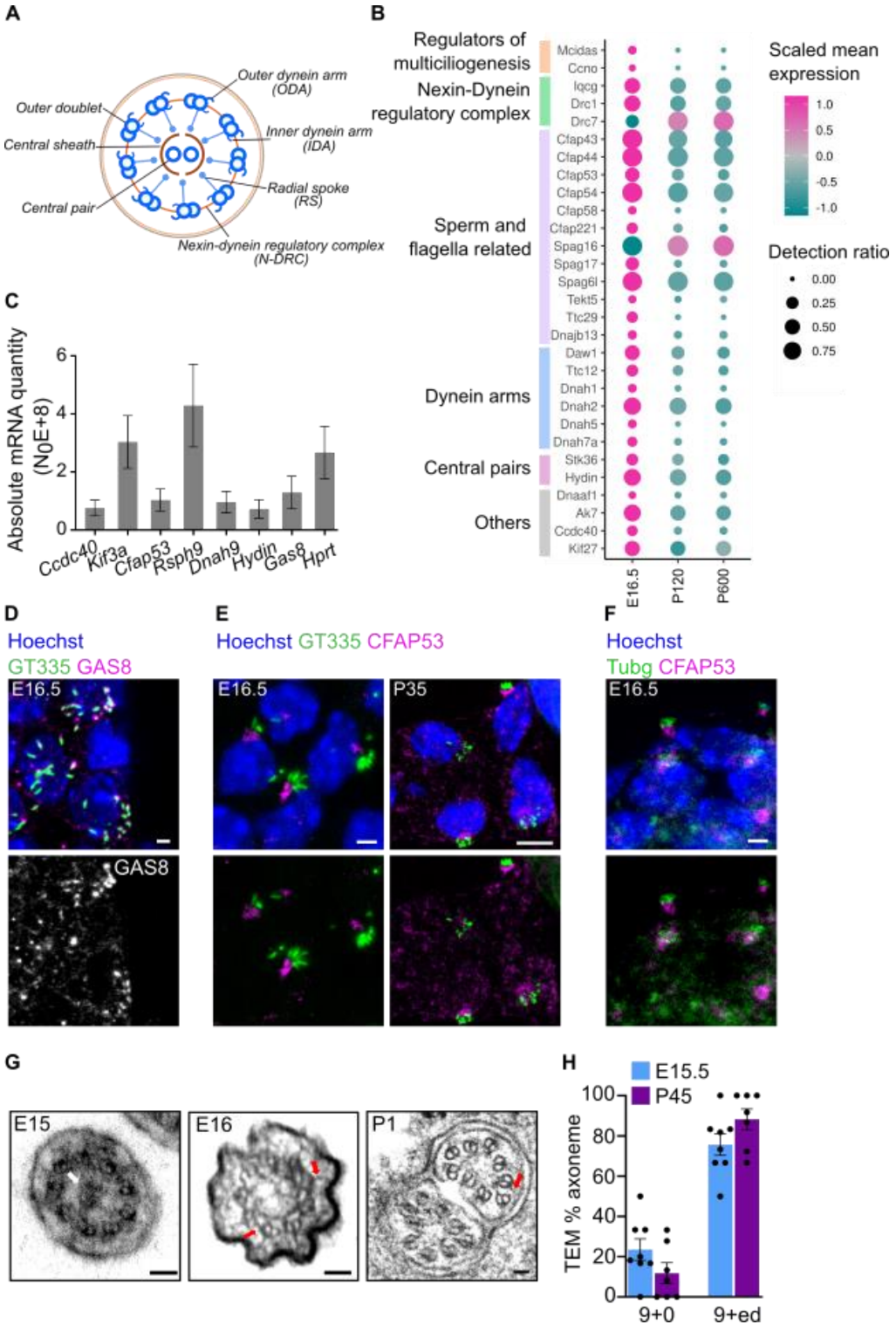

Figure 27: Multi-cilia of ChP have both primary and motile cilia features. A, *Diagram of an axonemal cross section of canonical motile cilia configuration.* ***B,*** *Dot plot of cilia motility genes' expressions by snRNA-seq. Scaled mean expression level in ChP epithelial cells (color) and proportion of expressing cells (circle size) of selected cilia motility candidate genes (rows) at different ages (columns).* ***C,*** *Absolute RT-qPCR expression level of a subset of motile cilia genes in E16.5 ChP homogenates. n = 3 embryos.* ***D,*** *E16.5 ChP sections stained against glutamylated tubulin (GT335) and GAS8.* ***E,*** *E16.5 and P35 ChP sections stained against GT335 and CFAP53.* ***F,*** *E16.5 ChP stained against γ-Tubulin (Tubg) and CFAP53.* ***G,*** *Transmission electron microscopy (TEM) of axonemal*

cross sections in ChP epithelial cells at E15, E16 and P1. Red arrows indicate putative dynein arms. White arrow indicates electron-dense structure. ***H,*** *Percentage of axoneme structure at indicated ages as examined by TEM. Ed, electron-dense structure. n = 7–8 cells per age. Scale bar: 2 μm (****D, E, F****), 450 nm (****G****). Bars represent mean ± SEM (****C, H****). Electron micrographs in Figure 27G was provided by Dr. Nathalie Spassky, Dr. Chiara Salio and Dr. Mirko Cortese.*

3.1.5. Gradual postnatal disappearance of choroid plexus cilia

Because the expressions of cilia motility genes changed in postnatal stages, I further analyzed postnatal ChP cilia to examine possible changes of cilia presentation. SsTEM reconstruction spanning the entire basal bodies of adult tChP revealed that most basal bodies possessed 2 to 3 basal feet (Fig. 28A-C). During embryonic stages, these basal feet were found to be more abundant (Fig. 25I), indicating potential maturation or functional alterations in basal body activity during postnatal stages. A complete three-dimensional TEM reconstruction and subsequent modeling of adult ChP cilia unveiled a systematic disorganization of the 9 doublets towards the ciliary tip, which strongly suggests the occurrence of microtubule deconstruction during postnatal stages (Fig. 28D). Next, I compared ChP cilia at birth (P0), P14 (eye opening), P35 (end of synaptogenesis) and P720 (aged brain) using double staining of ChP cryosections with Tubg and AcTuba antibodies. Our observations revealed a significant reduction in the presence of cilia at P35 (Fig. 28E). Furthermore, by super-resolution (STED) imaging of AcTuba and LRRC45, a marker for the distal end of the mother centriole [155], I were able to identify two distinct types of cilia clusters. The first type consisted of basal bodies with short axonemes (Fig. 28F, left), while the second type exhibited basal bodies that were either devoid of cilia or displayed only stubby, truncated axonemes (Fig. 28F, right). Quantitative analysis of both the tChP and hChP samples indicated a gradual decline in the percentage of cells with multiple basal bodies (Fig. 28G). In addition, there was a sharp decrease in the proportion of multiciliated cells between the P14 and P35 stages (from approximately 65% to less than 40%) (Fig. 28H). This decrease was accompanied by a significant reduction in cilia length, which reached its lowest point at the P720 stage (averaging 0.6 μm compared to 1.2 μm at P0) (Fig. 28I). SsTEM analysis of adult tChP cells revealed that most cells analyzed carried extremely short axoneme, which were rarely longer than microvilli (Fig. 28J). These short axonemes were also frequently deeply embedded in the cytoplasm within ciliary pockets (Fig. 28K). At the transcriptional level,

I analyzed the public snRNA data of ChP at 3 developmental stages [6] and showed that the vast majority of cilia organization genes (curated list based on GO Cilia organization) had reduced expression at P120 and P600 compared to E16.5 (Fig. 28L). Altogether, I demonstrated that ChP epithelial multicilia are not maintained throughout life but rather disappear from an early post-natal stage, which is quite a unique developmental characteristic of mammalian ciliated cells and suggest different developmental functions of these cilia.

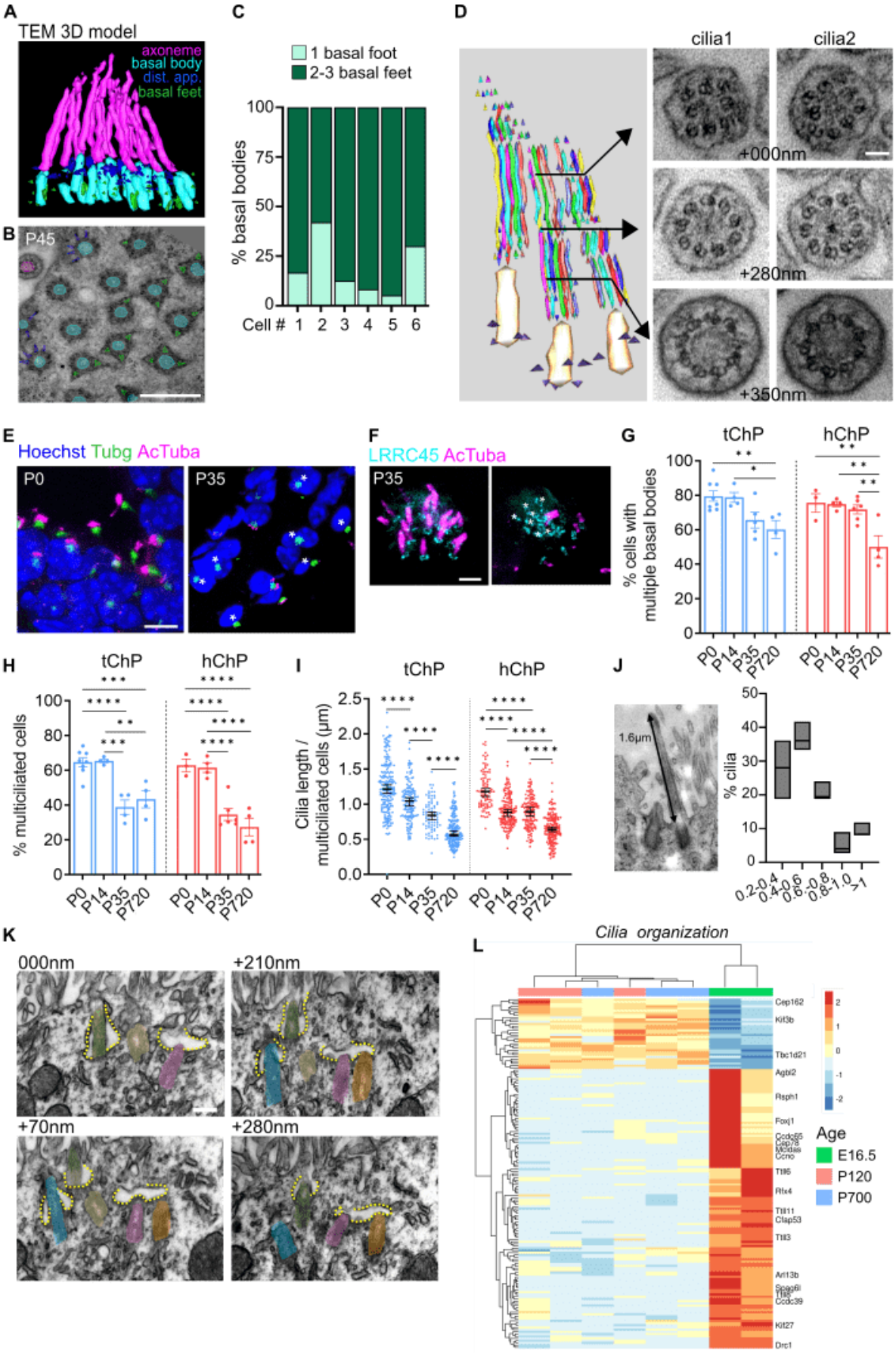
A
TEM 3D model
axoneme
basal body
dist. app.
basal feet
B
P45
C
1 basal foot
2-3 basal feet
% basal bodies
Cell # 1 2 3 4 5 6
D
cilia1
cilia2
+000nm
+280nm
+350nm
E
Hoechst Tubg AcTuba
P0
P35
F
LRRC45 AcTuba
P35
G
tChP
hChP
% cells with multiple basal bodies
P0 P14 P35 P720
H
% multiciliated cells
I
Cilia length / multiciliated cells (µm)
J
1.6µm
% cilia
0.2-0.4 0.4-0.6 0.6-0.8 0.8-1.0 >1
K
000nm
+210nm
+70nm
+280nm
L
Cilia organization
Age
E16.5
P120
P700

Figure 28: Disappearance of choroid plexus cilia starting from early postnatal ages. A, *Transmission electron microscopy (TEM) 3D model showing the tightly packed basal bodies at tChP cells at P45.* ***B,*** *TEM images showing cross sections of basal bodies with varied configurations of distal appendages and basal feet.* ***C,*** *Percentage of basal bodies carrying different numbers of basal feet. 6 cells of P45 tChP were used for this quantification, which was performed on TEM serial sections spanning the entire basal body patch in (88 basal bodies in total).* ***D,*** *TEM 3D reconstruction of tubulin doublets along the entire axoneme shaft of the tChP cilia at P45. The 3 displayed planes of TEM section shows the disorganization of microtubule doublets in the upper part of axoneme and discontinuous central blurry electron-dense structure.* ***E,*** *tChP sections stained against γ-Tubulin (Tubg) and acetylated α-tubulin (AcTuba) at P0 and P35. Asterisks (*) indicate cells negative for AcTuba.* ***F,*** *Super resolution images (STED) of P35 tChP sections stained against LRRC45 and AcTuba. Asterisks (*) indicate single LRRC45-positive basal bodies negative for AcTuba.* ***G,*** *Quantification of the percentage of cells positive for multiple basal bodies in both tChP and hChP at multiple postnatal ages. n = 3 mice per age.* ***H,*** *Quantification of the percentage of multi-ciliated cells in both tChP and hChP at multiple postnatal ages. n = 3 mice per age.* ***I,*** *Measurement of cilia length of multi-ciliated cells in both tChP and hChP at multiple postnatal ages. n = 80-200 cilia (from 3 mice) per ventricle per age.* ***J,*** *Axoneme length composition in adult P60 tChP. n = 205 axonemes (from 3 mice).* ***K,*** *TEM serial reconstruction showing the same multi-ciliated cell at P60. Colored regions indicate individual cilium. Yellow dotted lines indicate ciliary pockets.* ***L,*** *Heatmap of snRNA-seq data of differentially expressed cilia organization genes in all three ventricles at 3 developmental ages. Scale bar: 450 nm (**B**), 500 nm (**D**), 10 µm (**E**), 1 µm (**F**), 200 nm (**K**). Bars represent Bars represent Mean ± SEM (**G, H**). Bars represent Median ± 95% CI (**I, J**). Two-way ANOVA (**G, H**). Kruskal-Wallis (**I**). *p≤0.05, **p≤0.01, ***p≤0.001, ****p≤0.0001. Figures 28A-D are provided by Dr. Nathalie Spassky's group. STED image acquisition was performed by Dr. Martin Meschkat (Figure 28F). TEM micrographs (Figures 28J, K) were provided by Dr. Chiara Salio.*

3.1.6. Destabilization of microtubules is upstream of choroid plexus cilia regression

While cilium assembly is a well characterized process, much less is known about the mechanism of cilium disassembly/regression and most of the available knowledge is based on studies of primary cilium [156]. I hypothesized that microtubule destabilization could represent an important step in the regression of the axoneme. Multiple PTMs have been linked to microtubule turnover and tubulin destabilization [156], [157], [158]. Therefore, I examined the mRNA expression levels of key enzymes that regulate post-translational modifications (PTMs) throughout the ChP development and observed a rather distinctive pattern of expression (Fig. 29A, B). As anticipated, the majority of the acetylases, glutamylases, and glycylases exhibited high expression levels during embryonic stages and subsequently decreased at birth (Fig. 29A), as ciliogenesis in the ChP occurs during embryogenesis. Conversely, enzymes involved in the disassembly of

cilia, such as deacetylases *Hdac6, Sirt2,* and deglutamylase *Agbl4* (which encodes for CCP6), were all selectively upregulated at P15 in comparison to P0, then returned to baseline at P60. These findings strongly indicate the presence of a specific developmental time frame during which ChP epithelial cells activate a transcriptional pathway dedicated to the disassembly of cilia, which becomes evident at P35 (Fig. 28E, H).

Next, selective antibodies were used to assess the level of the total glutamylation (GT335) [159] and polyglutamylation (polyE, referring to side chains with more than four glutamates) [160]. The measurement of signal intensity showed a notable decline in the polyglutamylation/total-glutamylation (polyE/GT335) ratio during the transition from P0 to P15 and P35, indicating a destabilization of tubulin (Fig. 29C, D). In order to comprehend the significance of tubulin glutamylation levels in maintaining the axoneme in ChP epithelial cells, our first primary focus was on spastin, a protein responsible for severing microtubules and converting them into shorter fragments [161], [162], [163]. Spastin severing activity is a biphasic occurrence that is initially activated by an elevation in tubulin polyglutamylation. However, as more glutamates accumulate, they impede the activity of spastin [162]. In order to assess the contribution of spastin in maintaining the stability of ChP epithelial cilia, I examined P35 spastin KO (*Spast* KO) mice. These mice exhibited a subtle yet significant increase in the proportion of ChP epithelial cells with cilia (Fig. 29F, G) and a slight rise in the ratio of poly-glutamylation compared to their wild-type (WT) counterparts (Fig. 29H, I), indicating more stable axoneme microtubule. Of note, the levels of *Spast* mRNA remained unchanged during development (Fig. 29E), suggesting that our observed phenotype is primarily regulated at the local protein level. I postulated that the modulation of glutamylation level may be sufficient to regulate the stability of the axoneme. To examine this proposition, I considered CCP enzymes, which are responsible for the removal of glutamate residues from the C-terminal tails, thereby regulating the length of glutamylate chains on tubulin [160]. Because *Agbl4* was identified as the enzyme with the highest expression in the ChP at P15 (Fig. 29B), I proceeded to analyze *Agbl4* knockout (KO) mice (CCP6 KO) [164]. The CCP6 KO mice did not exhibit significant disparities when compared to their WT littermates, as there was no observable change in the percentage of ciliated cells (Fig. 29J, K), and the poly-glutamylation ratio remained diminished in the CCP6 KO (Fig. 29L, M). These findings provided evidence that CCP6 is not indispensable for either the formation or maintenance of cilia in the ChP, suggesting that other CCPs may have compensated for the loss of this

singular enzyme. Conclusively, our study has demonstrated that the absence of Spastin hinders the regression of cilia by regulating the level of microtubule polyglutamylation.

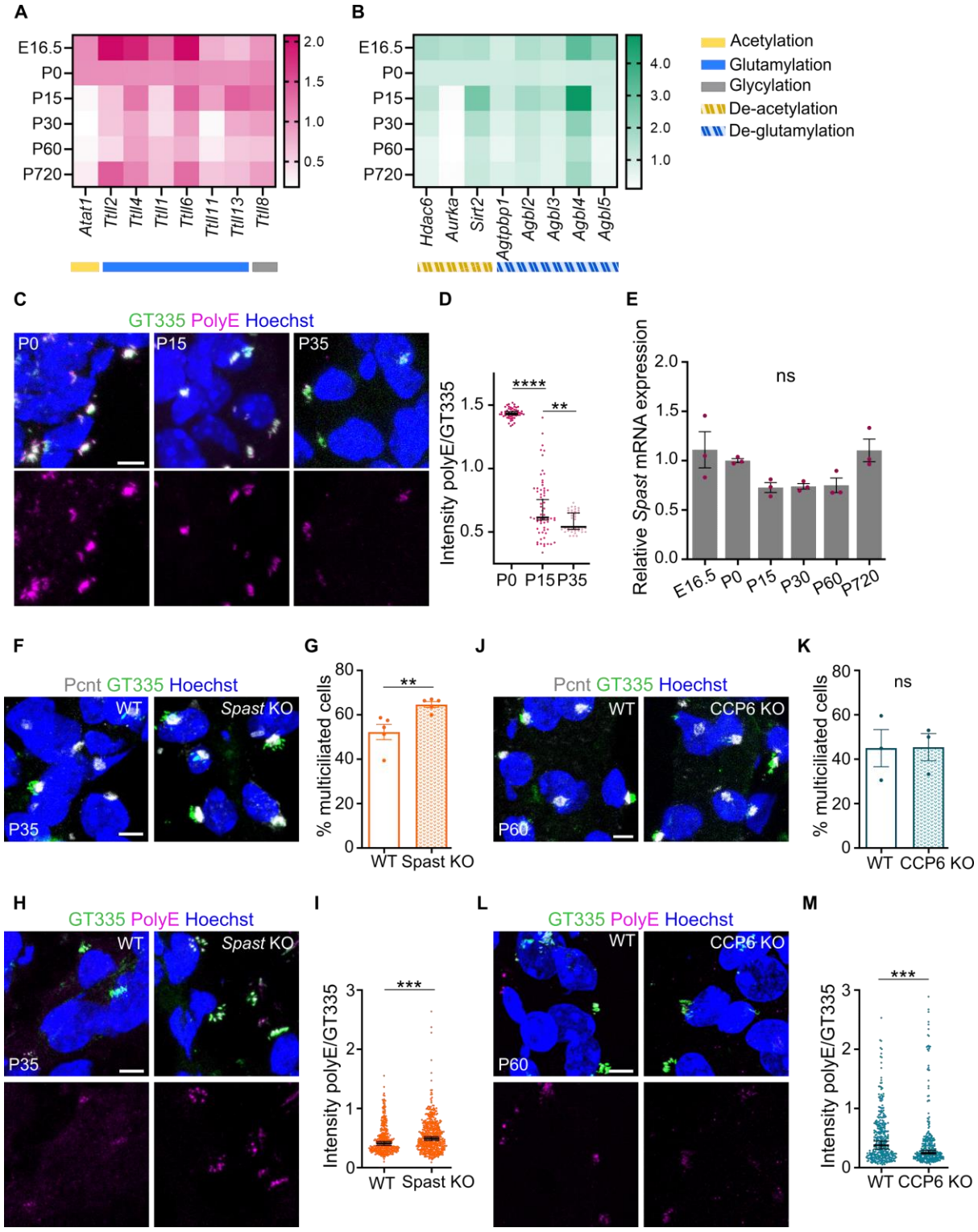

Figure 29: Spastin regulates choroid plexus cilia regression by controlling axonemal polyglutamylation level. A, *Heatmap from RT-qPCR data showing mRNA expression levels of post-translational modification enzymes, which introduces modifying compounds to tubulin, at multiple postnatal time points. n = 3 mice per age.* ***B,*** *Heatmap from RT-qPCR data showing mRNA expression*

levels of post-translational modification enzymes, which remove modifying compounds from tubulin, at multiple postnatal time points. n = 3 mice per age. ***C,*** *tChP sections at 3 postnatal ages stained against GT335 and polyE.* ***D,*** *Ratio of poly-glutamylation (polyE) over total Glutamylation (GT335) at 3 postnatal ages. Each dot represents a single cilium. n = 40-55 cilia clusters from 3 mice per age.* ***E,*** *Relative Spast mRNA expression levels at different developmental ages. n = 3 mice per age.* ***F,*** *P35 WT and Spastin (Spast) KO ChP sections stained against GT335 and pericentrin (Pcnt).* ***G,*** *Quantification of the percentage of multi-ciliated cells in P35 WT and Spast KO littermates. n = 5 mice per genotype.* ***H,*** *P35 WT and Spast KO ChP sections stained against GT335 and polyE.* ***I,*** *Ratio of poly-glutamylation (polyE) over total Glutamylation (GT335) in Spast KO compared to littermate WT. n = 250-350 cilia clusters from 5 mice per genotype.* ***J,*** *P60 WT and Agbl4 knockout (CCP6 KO) ChP sections stained against GT335 and Pcnt.* ***K,*** *Quantification of the percentage of multi-ciliated cells in P60 WT and CCP6 KO littermates. n = 3 mice per genotype.* ***L,*** *P60 WT and CCP6 KO ChP sections stained against GT335 and polyE.* ***M,*** *Ratio of poly-glutamylation (polyE) over total Glutamylation (GT335) in CCP6 KO compared to littermate WT. n = 280-320 cilia clusters from 3 mice. Scale bar: 5 µm (****C, F, H, J, L****). Bars represent Mean ± SEM (****E, G, K****). Bars represent Median ± 95% CI (****D, I, M****). One-way ANOVA test (****D, E****). Mann-Whitney test (****G, I, K, M****). *p≤0.05, **p≤0.01, ***p≤0.001, ****p≤0.0001. ns: not significant.*

3.1.7. Axonemal tubulin regression is evolutionarily conserved between human and mice

To further enhance the relevance of our findings, I examined human postmortem ChP specimens at multiple time points. In young ChP, a major proportion of epithelial cells (up to 80%), which were identified as positive for OTX2, TTR, and E-Cadherin (Fig. 30A), were ciliated as confirmed by double staining for pericentrin (PCTN) and GT335 (Fig. 30B-D). This percentage notably decreased to 60% in aged ChP specimens (Fig. 30B, D). Furthermore, the length of the axoneme showed a significant decrease over time (Fig. 30E). These findings indicate that the disappearance of cilia, along with the reduced axoneme length, is conserved between rodent and human ChPs. Similarly, the level of tubulin polyglutamylation showed a significant decrease in aged human ChP (Fig. 30F, G), thereby demonstrating the involvement of a similar molecular mechanism in the regulation of tubulin destabilization in both human and mouse ChP cilia.

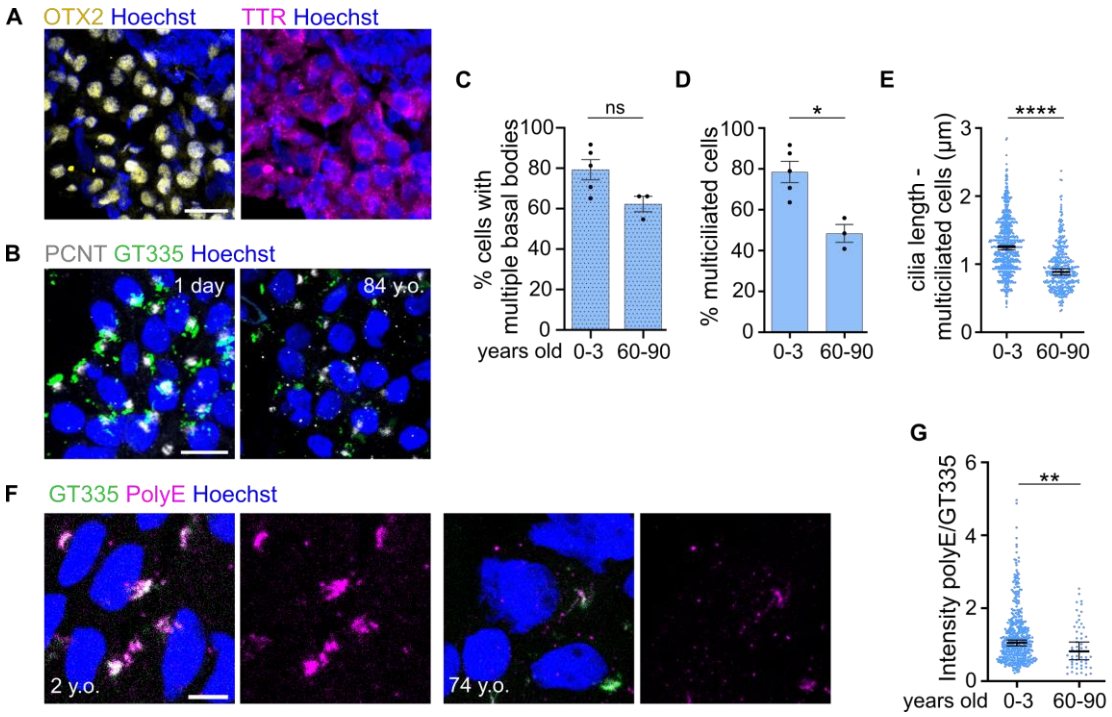

Figure 30: Regression of aged human choroid plexus cilia. A, *Human postmortem ChP sections stained against OTX2 and Transthyretin (TTR) in 1-day-old patient (left) and in 84-year-old patient (right).* ***B,*** *Human postmortem ChP sections stained against glutamylated tubulin (GT335) and pericentrin (PCNT) in 1-day-old patient (left) and in 84-year-old patient (right).* ***C,*** *Quantification of the percentage of cells positive for multiple basal bodies in young (0-3 years-old) and aged donors (60–90 years-old).* ***D,*** *Quantification of the percentage of multi-ciliated cells in young (0-3 years-old) and aged donors (60–90 years-old).* ***E,*** *Measurement of cilia length in multiciliated cells of young (0-3 years-old) and aged donors (60–90 years-old).* ***F,*** *ChP sections stained against GT335 and polyglutamylated tubulin (polyE) in 2 years-old and in 74-year-old donors.* ***G,*** *Ratio of poly-glutamylation (polyE) over total Glutamylation (GT335) in young (0-3 years-old) and aged donors (60–90 years-old). Each dot represents a single cilia cluster. n = 5 young specimens, 3 aged specimens (**C, D, E, G**). Scale bar: 20 µm (**A**), 10 µm (**B**), 5 µm (**F**). Bars represent Mean ± SEM (**C, D**); Bars represent Median ± 95% CI (**E, G**). Mann-Whitney test (**C, D, E, G**). *p≤0.05, **p≤0.01, ***p≤0.001, ****p≤0.0001. ns: not significant.*

3.2. Discussion

In this project, I have characterized the biogenesis and maintenance of cilia murine ChP epithelial cells. Our investigation reveals that the ChP primarily consists of Trp73+ multi-ciliated cells, the majority of which are produced as early as E10.5, coinciding with the production of the first neurons. The ChP epithelium is generated on a treadmill of incoming mono-ciliated progenitors on both sides of the expanding plexus during embryogenesis. Centriole amplification and multi-ciliogenesis proceed through a atypical series of events in most Trp73+ cells, with approximately 10% of cells remaining mono-ciliated during post-natal stages. I showed that ChP ciliogenesis takes place on a gradient of events along the tissue and is spatio-temporally controlled so that the majority of differentiated CPe harbor multiple cilia in a tight cluster. Remarkably, multi-ciliated ChP axonemes are regressed during the postnatal period, most likely through an intrinsic destabilization process of the axonemal microtubule controlled by the tubulin-severing protein Spastin and associated with downregulation of microtubule polyglutamylation. Finally, I showed that axoneme regression is not a species-specific event, as it also happens in postmortem human ChP epithelial cells.

Unlike ependymal cilia that are formed after birth, ChP epithelial cells commit to multi-ciliation fate and become ciliated since as early as E12.5 (hCP) - E14.5 (tCP). During embryonic development, ChP ciliated states closely correlate with cells' proliferation and maturation. Centriole amplification in ChP progenitors follows similar phases as observed in ependymal cells [88], although notable and significant differences were observed: centrioles/basal bodies are generated equally through either the centriolar or deuterosomal pathways, but their overall quantity is reduced by half compared to ependymal cells. Deuterosomes consistently maintain a smaller size during the amplification process and accompany the centrioles as they migrate apically towards the cell surface. The final stage of maturation involves the extreme compaction of basal bodies into a 2 μm^2 cluster located in the center of the apical surface, independent of cilia formation. Interestingly, at the basal bodies, the number of basal feet decreases from 6 to 2-3 between the embryonic and postnatal stages. Motile cilia typically carry on their basal bodies one basal foot each, which connect basal bodies to the cell's microtubule cytoskeleton, therefore linking motile cilia in a network and coordinate their beating

direction [165]. In multiciliated cells of the airways, loss of basal feet leads to disorientation of basal bodies and cilia coordination, manifested as the disorder of primary ciliary dyskinesia [165], [166]. Primary cilium, on the other hand, carries around its basal body up to nine basal feet, which keeps the cilium submerged in the cytoplasm and links the basal body to Golgi. This Golgi connection helps limit ectopic Shh signaling activation [167], [168]. Additionally, primary cilium's basal foot is also indirectly linked to TGF-β signaling [169]. Liu et al. recently discovered the hybrid cilium in airways and ependymal motile cilia, which expresses structural proteins for beating but carries three basal feet; these cilia are positioned toward the beating direction and function in the alignment of basal bodies [170]. In another case, exposure to thrombin results in a rapid increase in the number of basal feet per mature basal body in endothelial cells [171]. These information shows that the number of basal feet is directly linked to the specific cell type, its functional state, age, and external influences. Therefore, it is reasonable to speculate that the number of basal feet in ChP cells is influenced by similar, yet unidentified mechanisms that may contribute to the various functions of the ChP in the brain.

Unexpectedly, there is around 5% mono-ciliated cells within multiciliated cells of the fully developed ChP. Both mono and multi-cilia maintain a consistent 9+0 configuration throughout their lifespan, regularly with discontinuous unknown electron-dense structure in place of the central pair. This is by far a unique feature of ChP cilia, and highlight more the question of whether they are motile or not. Our study demonstrates that the ChP exhibits elevated levels of well-established motility cilia genes during the process of embryogenesis, which significantly decline postnatally, indicating a potential change in their function to adapt to the new developmental condition. In fact, these cells express CFAP53, a protein known to present specifically in motile cilia. While ependymal and tracheal cilia express CFAP53 at both basal bodies and axonemes, CFAP53 is restrictedly distributed at basal bodies of CP cilia, similar to nodal cilium [154]. Interestingly, it has been previously established that ChP cilia undergo rotational movements during embryonic development [93]. In summary, the localization of CFAP53 at the base of the cilia, the expression of motility genes, and the 9+0 axonemal ultrastructure collectively provide compelling evidence that the embryonic ChP multi-cilia bear resemblance to rotating nodal cilia.

Our study reveals that both mouse and human ChP exhibit an unconventional progressive regression of cilia that commences during early adulthood, which is an event not observed in mammalian multiciliated cells of other organs. I demonstrated that the regression of ciliary axoneme is regulated by the tubulin-severing enzyme spastin. Spastin is classified as a member of the microtubule-associated proteins family, and its catalytic efficacy relies on the concentration of glutamate chains on the targeted microtubule [162]. Indeed, while at P35 when the percentage of ciliated cells is decreased at P35, the expression of deglutamylase enzyme is increased since P14, and the intensity of poly-glumamylation is gradually decreased since P0 to P35. The absence of spastin (Spast KO) results in a greater number of ciliated ChP cells in adult mice, thus corroborating the notion that spastin's absence preserves the microtubules from being severed, allowing them to persist and continue undergoing polyglutamylation [164]. Although no significant regulators of spastin have been identified thus far, it is widely acknowledged, based on *in vitro* experiments, that spastin's activity can be temporally and spatially regulated at both the transcriptional and protein levels [172]. In the ChP, the level of spast mRNA remains constant over time, indicating that the selective activation of spastin may be associated with as yet unidentified cofactors that can independently activate and/or control spastin's activity, or changes in length of the microtubule glutamate-side chains through time becoming critical at young adult ages.

ChP cilia resorption since early postnatal ages confers a novel phenomenon in multiciliated cells. It is worth noting that not all cilia vanish from the ChP, indicating that local cilia may serve distinct functions during different stages of development. On functional aspect, when cells are multiciliated, their cilia are motile. Cilia quantity, length, beating amplitude and frequency are important for ependymal cilia to generate CSF fluid flow and for airway cilia to propel mucus and contaminants [173]. In fact, ChP cilia displayed weak, transient motility at perinatal period with mixed beating patterns and were speculated to generate CSF movement at this stage; however, experimental evidence from *ex vivo* setup concluded that such movement is too weak to power CSF flow [93]. I have also demonstrated that ChP cilia bear multiple characteristics of nodal cilia, which has critical roles in establishing left/right body asymmetry thanks to its rotational movement [174], [175]. Considering that (i) ChP develops anatomical laterality earliest in the human brain, (ii) its cilia form during the early stages of ChP morphogenesis, and

(iii) its cilia share similar features with nodal cilia, ChP cilia are thought to also affect brain asymmetry through modulating CSF movement [176], [177], [178]. However, there are also evidence suggesting ChP cilia function as sensory primary cilia. Despite their presence as multiple cilia, ChP cilia are significantly short (0.9 – 1.3 μm) compared to those of ependyma and trachea (4 – 8 μm) [148]. Additionally, ChP cilia axonemes structure are mainly 9+0, which is the notable tubulin structure of sensory primary cilium, therefore, ChP cells may also actually possess multiple primary cilia. In fact, ChP ciliary dysfunction in *Tg737*^{orpk} mutants caused elevated intracellular cAMP level, altered pH regulation and ion transporter activity [83]. ChP cilia were also shown to modulate fluid transcytosis [84] and to share molecular similarity with photoreceptor outer segment [92]. Furthermore, a recent study demonstrated the link between ChP cilia loss and tumor associated hydrocephalus via the recruitment and activation of mast cells [98]. In conclusion, the distinctive characteristics of ChP cilia suggest unconventional yet potentially significant roles, underscoring the need for further investigation into their functions in both normal development and neuropathological conditions.

4. Conclusion and Perspective

In my doctoral studies, I have elucidated the mechanism driving CPT pathogenesis, namely the dysregulated activation of Wnt/β-catenin signaling – a pathway crucial for ChP development. Additionally, I created the first human-cell-derived organoid model of CPT using genetic engineering, facilitating further investigations and drug testing. Simultaneously, my second project delved into the detailed understanding of ChP cilia biogenesis and maintenance – an atypical organelle of the ChP.

Although the two projects appear disparate, progress in one domain could significantly advance research in the other. As ChP epithelial cells in both human and mouse transition from a multiciliated to monociliated state in tumors [75], [78], with an increasing proportion of mono-ciliated cells correlating positively with tumor aggressiveness [75], studying key events regulating multi-ciliogenesis in ChP can unveil crucial factors in tumor initiation and malignancy. Moreover, since 70% of CPT patients exhibit hydrocephalus symptoms [97], and hydrocephalus has been linked to several dysfunctions of ChP cilia [83], [98], investigations into ChP cilia function relating to CSF secretion may offer a new therapeutic strategy to address this complication. Conversely, identifying the oncogenic factors causing cell transition from multi- to mono-ciliated state may lead to findings of novel regulators upstream of multiciliogenesis in ChP. As my study found that Wnt/β-catenin signaling is activated in CPT, it is intriguing to explore potential regulatory role of Wnt/β-catenin pathway in ChP multiciliogenesis. Additionally, many components of the Wnt pathway are associated with the cilium structure; therefore, cilia disruption in CPT could exacerbate the dysregulation of Wnt/β-catenin signaling. Interestingly, the interaction between Wnt/β-catenin signaling and cilia has been a complex and controversial topic, with contradicting findings reported on whether cilia promote or inhibit Wnt/β-catenin signaling, and whether this pathway plays a role in regulating cilia formation or not [179], [180], [181], [182], [183]. However, studies of Wnt/β-catenin and cilia mainly focus on primary cilia; therefore, investigations on the interaction between Wnt/β-catenin signaling and the atypical cilia of ChP are necessary and could provide additional viewpoints into this topic.

So far, the majority of data relating to CPT and ChP cilia are derived from mouse models. While future studies integrating CPT and cilia could still be conducted on this system, utilizing organoid models created from human induced pluripotent stem cells – similar

to CPT organoids created in my project – offers a promising alternative to reduce the use of experimental animals and identify therapeutic options that are more compatible with the human system. However, further investigations into ChP organoid's development and ciliogenesis are necessary to ensure its similarity to the processes taking place in human. In conclusion, the two projects conducted during my PhD have laid the groundwork for further investigations into each topic individually, as well as for exploring the interconnection between the two processes – rare tumorigenesis and atypical cilia, ultimately for the enhancement of our understanding of ChP from multiple aspects.

5. Materials and Methods

5.1. Materials

5.1.1. Human tissue samples

Table 2: Human tissue samples used in the studies

Code	Source	Gender	Age	Clinical history	Experiment
1275	NIH	F	2.2y	Acute Myocarditis	IF
4942	NIH	F	0y	Premature birth	IF, WB
5576	NIH	M	2.8y	Drowning	IF
5618	NIH	F	68y	Heart disease	IF
5770	NIH	F	0.4y	Sudden death	IF, WB
5744	NIH	F	84.3y	Alzheimer disease; hypothyroidism	IF
5754	NIH	M	0.4y	Sudden death	IF
5824	NIH	M	74.3y	Hypertensive calcific atherosclerotic disease	IF
5879	NIH	M	15y	Normal	WB
NCH719x	NCT	F	30y	CPP	WB
NCH714c	NCT	M	16y	CPC	WB
N3562/09	UKM	F	0.6y	CPC	WB
01/174	NBB	F	47y	Normal	RT-qPCR, WB
N2323/14	UKM	M	72y	CPP	RT-qPCR, WB
N4942/17	UKM	F	0.8y	CPC	RT-qPCR, WB
N713/13	UKM	M	30y	CPC	RT-qPCR, WB
97/337	NBB	M	78y	Normal	RT-qPCR
03/258	NBB	F	24y	Normal	RT-qPCR
N2940/14	UKM	F	12y	aCPP/CPC	RT-qPCR
N1959/05	UKM	F	1.5y	CPP	RT-qPCR
N329/04	UKM	M	0.9y	CPP	RT-qPCR
3017/13	UKM	M	10y	CPP	IHC

1940/08	UKM	M	50y	CPC	IHC
N394/23	UKM	M	1.2y	CPP	IHC
N4606/22	UKM	F	2y	CPC	IHC
N2623/22	UKM	M	3y	CPC	IHC
N615/23	UKM	M	58y	CPP	IHC
N1030/00	UKM	F	2y	CPP	IHF
N745/20	UKM	M	9m	CPC	IHF

NIH: National Institutes of Health (USA); NBB: The Netherlands Brain Bank (the Netherlands); UKM: Uniklinik Münster (Germany); NCT: Nationales Centrum für Tumorerkrankungen (Germany); F/M: female/male.

5.1.2. Chemicals and reagents

Table 3: Chemicals and reagents

Item	Catalog number	Manufacturer
2-Mercaptoethanol	M3148-25mL	Sigma-Alrich
2-Phenylbenzothiazole, 97%	225444-5G	Sigma-Alrich
A83-01 (TGF-β pathway inhibitor)	Cay9001799	Biomol
Albumin (BSA) Fraction V (pH 7.0)	A09-A65880100	Applichem
Ammonium Acetate	AM9071	Gibco
Ammonium Persulfate (APS)	486-25G	VWR International
Ampicillin sodium salt	K029.5	Carl Roth
ATP	A2383	Sigma-Alrich
B27 supplement	17504044	Gibco
BMP4 (recombinant protein)	130-110-921	Miltenyi Biotec
Bovine serum albumin (BSA)	A6588.0100	AppliChem
BrdU	B5002	Sigma-Alrich
$CaCl_2$	A119.1	Carl Roth
Cell staining buffer	420201	BioLegend
CHIR99021	SM13	Cell Guidance Systems
Corning® Matrigel® Growth Factor Reduced (GFR)	356230	Corning
Crystal Violet	B21932.14	VWR International

D-fructose	F0127	Sigma-Aldrich
D-glucose	HN06	Carl Roth
D-luciferin	L9504	Sigma-Alrich
Dako mounting medium	S302380-2	Agilent
RNase-Free DNase Set (50)	79254	Qiagen
DiI dye	60014	Biotium
DMEM high glucose medium	41965-039	Gibco
DMEM/F12 medium	11330032	Gibco
DMSO	2650	Sigma
dNTP 10mm	R0192	VWR International
Doxorubicin	HY-15142	MedChemExpress
DTT	40400120-1	Biotrend
EdU	A10044	Invitrogen
Essential 8 (E8) medium	A1517001	Gibco
Ethanol	32221-2.5L-M	Sigma-Aldrich
Eukitt mounting medium	600010001040101	ORSAtec
FastAP Thermosensitive Alkaline Phosphatase	EF0651	Thermo Scientific
FastDigest Esp3I	FD0454	Thermo Scientific
FastRuler Middle Range DNA Ladder	SM1113	Life Technologies
Fetal bovine serum (FBS)	10500064	Gibco
Fluoromount-G	0100-01	Southern Biotech
Geltrex	A1413202	Gibco
GeneRuler Low Range DNA Ladder	SM1193	Thermo Scientific
Gentamicin	15710049	Gibco
GlutaMax	35050038	Gibco
Glycerol	7530.1	Carl Roth
Glycine	13073	Sigma-Aldrich
HCl 37%	30721-1l-m	Sigma-Aldrich
Heat-inactivated horse serum	26050070	Life Technologies
Heparin	H3149	Sigma-Aldrich
HEPES	H0887-100mL	Sigma-Aldrich

Hoechst 33342	Cay15547-25	Biomol
Insulin	I9278	Sigma-Alrich
KCl	6781.1	Carl Roth
L-Glutamine	25030024	Gibco
Laemmli sample buffer	1610747	Bio-Rad
LDN-193189 (BMP pathway inhibitor)	SM23	Cell Guidance Systems
Low-melting agarose	850081	Biozym scientific
MEM medium	M2279	Sigma-Aldrich
MEM NEAA	11140035	Gibco
Methanol	1.06009.2511	Merck
$MgSO_4$	sc-250284	Santa Cruz
MTT	475989	Merck
N2 supplement	A1370701	Gibco
NaCl	S316060	Thermo Fisher Scientific
Normal donkey serum unconjugated	LIN-END9010-10	Biozol Diagnostica
Normal goat serum unconjugated	005-000-121	Jackson ImmunoResearch
NP-40	NP40S	Sigma-Aldrich
Opti-MEM	31985062	Gibco
Page Ruler Plus Pre-stained Protein Ladder	26619	Life Technologies
Paraformaldehyde Solution 16%	E15710	ScienceServices
PBS, pH 7.4	10010023	Gibco
PBS powder pH 7	P3813-10PAK	Sigma-Aldrich
Peqgreen	732-2960	VWR international
Penicillin/Streptomycin	15070063	Gibco
Phosphatase inhibitor	4906837001	Roche
Pierce™ ECL Western Blotting Substrate	32109	Thermo Scientific
Pluronic F-127	P2443	Sigma-Aldrich
Polyethylenimine (PEI)	23966-1	Polysciences
Polybrene	sc-134220	Santa Cruz

Protease inhibitor	04693159001	Roche
RNase A	19101	Qiagen
ROTIPHORESE®Gel 30	3029.1	Carl Roth
SDS	CN30.3	Carl Roth
Skim milk powder	#1602.0500	GERBU Biotechnik
Sodium acetate	71196-100mL	Sigma-Aldrich
Sodium cacodylate Buffer	97068	Merck
Sodium pyrophosphate	M9191-500g	Hölzel Diagnostik
Sucrose	19401890	MP Biomedicals
T4 Polynucleotide Kinase	M0201S	New England Biolabs
TBST	1061.1	Carl Roth
TEMED	2367.1	Carl Roth
Tissue-Tek OCT Compound	SA62550	Sakura Finetek
TRIS	T1503	Sigma-Aldrich
Triton X-100	T9284	Sigma-Alrich
Trypan Blue	15250061	Gibco
TrypLE Express	12605028	Gibco
Trypsin	15400054	Gibco
UltraPure™ DNase/RNase-Free Distilled Water	10977035	Invitrogen
WesternBright Chemiluminescence Substrate	541020	Biozym
WNT974	HY-17545	MedChemExpress
XAV939 (Wnt pathway inhibitor)	SM38	Cell Guidance Systems
Y-27632 (ROCK inhibitor)	SM02	Cell Guidance Systems

5.1.3. Media and buffers

Table 4: Media and buffers composition

Media/Buffer	Composition
1X Running buffer	25 mM Tris 192 mM Glycine

	0.1% SDS
	MilliQ H_2O
1X Transfer buffer	25 mM Tris
	192 mM Glycine
	20% MeOH
Brain slice medium	MEM medium
	25% heat-inactivated horse serum
	25 mM HEPES
	1 mM L-Glutamine
	1% Penicillin/Streptomycin
Cacodylate buffer	50 mM Cacodylate buffer
	1 M KCl
	0.1 M CaCl2
	0.1 M MgCl2
	0.2 2.5% Glutaraldehyde
	0.3 2% sucrose
ChP induction medium	DMEM/F12
	0.5 % N2 supplement
	1% B27 supplement
	1% GlutaMax
	1% NEAA
	4.44 mM D-glucose
	2.5 µg/ml Insulin
	20 ng/ml BMP4
	3 µM CHIR99021
	1% Penicillin/Streptomycin
FACS buffer	2% FBS
	25 µg/ml DNase
	25 mM HEPES
	2 mM EDTA
	PBS
Firefly substrate solution	25 µM DTT
	1 mM ATP

	0.2 mM D-Luciferin P/RlucA solution
HIBCPP medium	DMEM/F12 10% FBS 5 µg/ml Insulin 2% Penicillin/Streptomycin
Neural induction medium	DMEM/F12 0.5% N2 supplement 1% B27 supplement 0.2 mM LDN-193189 0.5 mM A83-01 2 µM XAV939 1% GlutaMax 1% NEAA 4.44 mM D-glucose 10 µg/ml Heparin 1% Penicillin/Streptomycin
NP40 buffer	50 mM Tris/Tris-HCl pH8 120 mM NaCl 1% NP40 MilliQ H_2O Phosphatase and Protease inhibitors (added right before use)
P/Rluc lysis buffer (5X)	125 mM Tris-Phosphate 10 mM DTT 10 mM EDTA 5% Triton X-100 50% Glycerol
P/RlucA (pH 8.0)	200 mM Tris/HCl 15 mM $MgSO_4$ 0.1 mM EDTA MilliQ H_2O
P/RlucB (pH 5.0)	25 mM Sodium Pyrophosphate

	10 mM Sodium Acetate 15 mM EDTA 500 mM Sodium Sulfate 500 mM Sodium Chloride
Renilla substrate solution	4 µM Coelenterazine h 50 µM Benzothiazole P/RlucB solution
Z310 medium	DMEM #41965-039 10% FBS 1% Penicillin/Streptomycin 40 µg/ml Gentamycin

5.1.4. Antibodies

Table 5: Primary and secondary antibodies

Antibody	**Host species**	**Catalog number**	**Manufacturer**	**Dilution (IF)**	**Dilution (WB)**
Primary antibodies					
anti-acetylated α-tubulin	rabbit	5335T	Cell Signaling	1:800	
anti-α-tubulin	mouse	T9026	Sigma-Aldrich	1:1000	
Anti-active-CTNNB1	mouse	05-665	Sigma-Aldrich		1:500
anti-APC	mouse	OP44-100UG	Merck		1:100
anti-AQP4	mouse	sc-32739	Santa Cruz	1:100	
anti-ARL13B	mouse	75-287	NeuroMab	1:100	
anti-AXIN2	rabbit	ab32197	Abcam		1:800
Anti-β-actin	mouse	3700	Cell Signaling Technology		1:3000
anti-BrdU	rat	BU1/75	Abcam	1:500	

anti-cleaved Caspase-3	rabbit	9664	Cell Signaling Technology	1:500	
anti-CFAP53	rabbit	A16607	ABclonal	1:200	
anti-CTNNB1	mouse	610153	BD Biosciences	1:500	1:1000
Anti-DVL2	rabbit	3216	Cell Signaling Technology		1:1000
anti-E-Cadherin	mouse	610182	BD Biosciences	1:200	
anti-γ-tubulin	mouse	MA1-19421	Invitrogen	1:1500	
anti-GAS8	rabbit	HPA041311	Atlas Antibodies	1:200	
anti-GFP	chicken	GFP-1010	Hölzel	1:1000	
anti-glutamylated tubulin GT335	mouse	AG-20B-0020	AdipoGen	1:800	
anti-glycylated tubulin	rabbit	AG-25B-0034-C100	Biomol	1:5000	
anti-KI67	rabbit	PA5-19462	Thermo Fisher Scientific	1:700	
anti-LMX1A	rabbit	AB10533	Milipore	1:300	
anti-LRP6	rabbit	2560	Cell signaling Technology		1:500
anti-LRRC45	guinea pig	A gift from Dr. Gislene Pereira		1:200	
anti-OTX2	goat	AF1979-SP	R&D Systems	1:200	
anti-p-CTNNB1	rabbit	9561	Cell signaling Technology		1:1000
anti-pericentrin	rabbit	ab4448	Abcam	1:200	
anti-polyE	rabbit	AG-25B-0030-C050	AdipoGen	1:1000	
anti-RSPH9	rabbit	HPA031703	Atlas Antibodies	1:200	
anti-TP73	rabbit	ab40658	Abcam		
anti-TTR	sheep	ab9015	Abcam	1:300	
anti-WNT3A	rabbit	2721	Cell Signaling Technology		1:1000
Secondary antibodies					

Abberior STAR 635 anti-guinea pig	goat	STRED-1006-500UG	Abberior GmbH	1:500	
Alexa Fluor 488/555/ 594/647 anti-chicken/ goat/mouse/ rabbit/ rat/sheep	donkey, goat		Jackson ImmunoResearch	1:500	
anti-mouse HRP	rabbit	ab6728	Abcam		1:5000
anti-rabbit HRP	goat	ab6721	Abcam		1:5000

5.1.5. Vectors, DNA fragments and oligonucleotides

5.1.5.1. Vectors

Table 6: Vectors

Vector	Source
lentiCRISPRv2 puro	addgene #98290
lentiCRISPRv2 mCherry	addgene #99154
pcDNA3.1	A gift from Prof. Dr. Aurelio Teleman
pLenti-CAG-empty-ires-EGFP	addgene #122953
pRenilla	A gift from Prof. Dr. Sergio Acebron
psPAX2	A gift from Dr. Ana Banito
TOPFlash	A gift from Prof. Dr. Sergio Acebron
VSV-G	A gift from Dr. Ana Banito

5.1.5.2. Primers

Table 7: Primers' sequences

Target	Sequence (5'-3')	Product size (bp)	Source

qPCR	**(h: human, m: mouse, r: rat)**		
h-ACTB	TCCCTGGAGAAGAGCTACGA	98	[184]
	AGGAAGGAAGGCTGGAAGAG		
h-APC	CATGATGCTGAGCGGCAGA	104	[185]
	GCTGTTTCATGGTCCATTCGTG		
h-AQP1	TGGACACCTCCTGGCTATTG	164	[186]
	GGGCCAGGATGAAGTCGTAG		
h-AXIN2	GTGAGGTCCACGGAAACTGT	103	[187]
	TGGCTGGTGCAAAGACATAG		
h-CLIC6	GGGACCCAACATCCCGAATC	161	PrimerBank
	TCAGGCAGAGGGCTATTTAAGT		[188]
h-CTNNB1	TCTGAGGACAAGCCACAAGATTACA	122	[185]
	TGGGCACCAATATCAAGTCCAA		
h-DKK1	ATAGCACCTTGGATGGGTATTCC	96	PrimerBank
	CTGATGACCGGAGACAAACAG		[188]
h-HPRT	CAGTCCCAGCGTCGTGATTA	168	[189]
	TGGCCTCCCATCTCCTTCAT		
h-HTR2C	CTAATTGGCCTATTGGTTTGGCA	89	[190]
	CCACCATCGGAGGTATTGAAAA		
h-KCNJ13	TTTTGTGGCGAAGATTGCCC	149	This study
	AGACCCGGACACTGGTTAGA		
h-MYC	TGAGGAGACACCGCCCAC	71	[191]
	CAACATCGATTTCTTCCTCATCTTC		
h-OTX2	CAAAGTGAGACCTGCCAAAAAGA	179	PrimerBank
	TGGACAAGGGATCTGACAGTG		[188]
h-RPL13A	CATAGGAAGCTGGGAGCAAG	157	[192]
	GCCCTCCAATCAGTCTTCTG		
h-SFRP1	TGGAGGGGTTTACCTGGAAC	107	This study
	AGCTGTTGCTTCCTACCTGA		
h-TTR	TGGGAGCCATTTGCCTCTG	240	PrimerBank
	AGCCGTGGTGGAATAGGAGTA		[188]
h-WIF1	GCCCACAACCCTGTCGAAAT	75	

	CTCCCTGGTAACCTTTGGAAC		PrimerBank [188]
m-Agbl2	ATGAATGTCCTGCTTGAGATGG	146	PrimerBank [188]
	CAAACGCGCTGATGAGTGC		
m-Agbl3	TGACTTGGATGAGGATTCCTTCA	96	PrimerBank [188]
	GGGAAGAATGGGTCACCAATAG		
m-Agbl4	AGGCAGGCAATGATACAGGAA	135	PrimerBank [188]
	GGTTACCACTTTCAAAGCAAGCA		
m-Agtbbp1	ATGAGCAAGCTAAAAGTGGTGG	107	PrimerBank [188]
	TCTGACTCTGTGGAATCCGTATT		
m-Atat1	AGCAACCGGCACGTTATTTAC	147	PrimerBank [188]
	GCAAAGGGGTTCTACCTCATTGT		
m-Aurka	GAATTGTAACGGCTGAGCTACC	73	This study
	TCCATGTCACAGGCAGGAAC		
m-Ccdc40	GGAAGGCCCTCCGAGGAATA	86	PrimerBank [188]
	TTGGGGTCTGACCTTTCTGTG		
m-Cfap53	TCTAGTTTCCTGTCGCCACC	134	This study
	CTCTGAGCTTTGGGAGGCTT		
m-Dnah9	CACAGTGAGCCAGTCTCAGAT	144	This study
	GGGGGTGGGATTTTGTCCTT		
m-Gas8	GACGAGATGAACGAGATGCAG	120	PrimerBank [188]
	TTCCCATTTCAGGTCCTTTAGC		
m-Hdac6	GAGGAGCTGATGTTGGTTCAC	124	PrimerBank [188]
	AGTTCGGATGCAGATACACTGA		
m-Hprt	CAAACTTTGCTTTCCCTGGT	101	[193]
	TCTGGCCTGTATCCAACACTTC		
m-Hydin	CTTGCCCCTCCGAATCAGAG	114	PrimerBank [188]
	AGGATTGCCTCGTAACAGTGA		
m-Kif3a	ATGCCGATCAATAAGTCGGAGA	134	This study
	GTTCCCCTCATTTCATCCACG		
m-Rpl27	AAGCCGTCATCGTGAAGAACA	143	[193]
	CTTGATCTTGGATCGCTTGGC		

m-Rpl13a	AGCCTACCAGAAAGTTTGCTTAC	129	[193]
	GCTTCTTCTTCCGATAGTGCATC		
m-Rsph9	CACTGCTCACGTCCCTTATGC	100	PrimerBank
	GCGATGTAGTAATCCGCCACA		[188]
m-Sirt2	CAAGGAAAAGACAGGCCAGA	84	[194]
	GCCTTCTTGGAGTCAAAATCC		
m-Spast	GCCTCGATCAAAAACTGTCCT	106	PrimerBank
	TCCCGGTCTTGCTCCAGAAA		[188]
m-Ttll1	GTGTCGCAGTCCACAAAAGAA	93	PrimerBank
	ATACAGACGAAGGTCAAACTTCC		[188]
m-Ttll2	ATGACCAATCTCACCAGGAAGG	76	PrimerBank
	AGAGAGACTCACCATAGCGAC		[188]
m-Ttll3	ATGGGCCGACTCAGAAACG	104	PrimerBank
	CGCAAGAGACACCGGATCA		[188]
m-Ttll4	AGGCAAAAACCATACCAGCAA	119	PrimerBank
	GTGGCTTTATTGGCAGTGACA		[188]
m-Ttll6	AAGCCCTTCATCATCGACGG	142	PrimerBank
	TGTCTAGGTTAGGGTGGGAGTAA		[188]
m-Ttll8	TTCACAACCAAGATTGGACTCTG	108	PrimerBank
	GCTCTCAGTGCAAAGGCCATA		[188]
m-Ttll11	TGTCTCAGGTCCAAACGGTG	76	PrimerBank
	CAACCACTATCCGGTTTCACAA		[188]
m-Ttll13	GTTAGAGAGGAATCTACCACCCC	97	PrimerBank
	CTACAACCGATAAGGCAACCC		[188]
r-Axin2	AAGAGCTACCCGTTGGAGTC	121	This study
	GGTCCTGGGTAAATGGGTGA		
r-Ctnnb1	TGGTGAAAATGCTTGGGTCG	54	This study
	TGGTGATGGCGTAGAACAGT		
r-Hprt	TTCCTCCTCAGACCGCTTTT	58	This study
	ACTGAGGGTCGACATGACAG		
r-Lrp6	CAATGGTCAGTGCGTTGGAA	106	This study
	CTGTAGGATGGTGGTGGGTT		

r-Myc	GGACAGTGTTCTCTGCCTCT	105	This study
	GTGACTGTCGGGTTTTCCAC		
r-Rpl13a	GCTGTGAGGGCATCAACATT	85	This study
	TTGGTGTTCATCCGCTTTCG		
PCR			
OG fwd	GCTGGCTCAACTTCCTACT	590: wt	[195]
Otx2 rev	TTGGTTGCATGTCGCTAGAA	1397: mt	
OG fwd	GCTGGCTCAACTTCCTACT	590: wt	[195]
GFP rev	ACCCTCTCCACTGACAGAA	423: mt	
sgAPC-r1-P1	GACTCCATCAGTACAGGGCA	767	This study
	TTGGCACCTCTCTCTTGGTC		
sgAPC-r3-P1	AGTCATCACGCAAAGCCAAA	788	This study
	GGGTGTGTAATGATGCGGTG		

5.1.5.3. Other oligonucleotides

Table 8: Other olionucleotides

Name	**Sequence (5'-3')**	**Usage**	**Source**
sgAPC-h1	GATGGTAGAAGTTTGTACAC	sgRNA	This study
sgAPC-h2	GATGACAATAAAGCAGAGGA	sgRNA	This study
sgAPC-r1	GCTTAGCTTCAGAATCCGCC	sgRNA	This study
sgAPC-r2	GTTCAGAGTGAGCCATGTAG	sgRNA	This study
sgAPC-r3	GATAATGGACCAAGTCCAAC	sgRNA	This study
sgAPCr1-P1S1	CTGCAAAGTCCCCTCCATCA	Sanger sequencing	This study
sgAPCr1-P1S2	GCTGACAATCCCACTCACCA	Sanger sequencing	This study

5.1.6. Kits

Table 9: Kits

Name	Catalog number	Manufacturer
Biozym Red HS Taq Master Mix	331126L	Biozym
Click-iT™ EdU Cell Proliferation Kit for Imaging, Alexa Fluor™ 594 dye	C10339	Invitrogen
Dual-Glo® Luciferase Assay System	E2920	Promega
EZ-PCR Mycoplasma test	20-700-20	NeoLab
FITC Annexin V Apoptosis Detection Kit	640914	BioLegend
GeneArt Genomic Cleavage Detection Kit	A24372	Life Technologies
Glycogen, RNA grade	R0551	Thermo Scientific
High-Capacity RNA-to-cDNA™ Kit	4387406	Applied Biosystems
Lipofectamine 3000 Transfection Reagent	L3000001	Life Technologies
NucleoSpin Plasmid (250)	740588250	Macherey-Nagel
NucleoSpin Gel and PCR Clean-up	740609250	Macherey-Nagel
Pierce BCA Protein Assay Kit	23225	Life Technologies
PowerUp SYBR Green Master Mix	A25918	Life Technologies
QIAshredder (50)	79654	Qiagen
QIAquick PCR Purification Kit (50)	28104	Qiagen
Quick Ligation™ Kit	M2200S	New England Biolabs
RNeasy Mini Kit (50)	74104	Qiagen
SampleIN™ Direct PCR Kit	DPK0105	highQu

5.1.7. Cell lines and bacteria strains

Table 10: Cell lines and bacteria strains

Item	Source
Cell line	
HEK293T	A gift from Dr. Wilhelm Palm

HIBCPP	A gift from Prof. Dr. Christian Schwerk
Z310	Provided by Dr. QiuQu Zhao
Bacteria	
One Shot™ Stbl3™ Chemically Competent *E. coli*	Invitrogen #C737303

5.1.8. Consumables

Table 11: Consumables

Item	Catalog number	Manufacturer
24-well ThinCert® cell culture insert	662638	Greiner Bio-One
Cell culture multi-well plate, 6 wells	657160	Greiner Bio-One
Cell culture multi-well plate, 12 wells	665180	Greiner Bio-One
Cell culture multi-well plate, 24 wells	662160	Greiner Bio-One
Coverslips 24 x 50 mm	2980-225	Corning
Cryotube 1.8 ml	V7634-500EA	Sigma-Aldrich
Frosty box	KR-FB-18	Kisker Biotech
LightCycler® 480 Multiwell Plate 384, white	4729749001	Roche
Luna cell counting slide	L12001-LG	BioCat
Millex GS Filter steril 0.22 µm		Millipore
Millex HA Filter sterile 0.45 µm		Millipore
µ-Slide 8 Well Glass Bottom	80827	ibidi
µ-Plate 24 Well Black	82426	ibidi
PAP Pen	A-PAP Pen	Daido Sangyo
PCR tube	294981305	neoLab
Petri dish, 10 cm, cell culture	664160	Greiner Bio-One
PP tubes, round bottom, 14 ml	187261	Greiner Bio-One
PVDF Transfer Membrane, 0.45 µm	88518	Thermo Scientific

Scalpel	9409805	Th. Geyer
Serological pipette 5 ml	606180	Greiner Bio-One
Serological pipette 10 ml	357551	Corning
Serological pipette 25 ml	4489	Costar
Superfrost® Plus slides	9161155	Th. Geyer
Tube 5 ml	0030119401	Eppendorf
Tube 2 ml	0030120.094	Eppendorf
Tube 1.5 ml	0030120.086	Eppendorf
Tube 1.5 ml, Biopur®, individually packed	296921589	Eppendorf

5.1.9. Equipment

Table 22: Equipment

Equipment	Type	Manufacturer
Agarose gel electrophoresis system	Mupid One	Nippon Genetics
Automated stainer	BenchMark ULTRA Autostainer	VENTANA/Roche
Cell counter	LUNA-II™ Automated Cell Counter	logos biosystems
Centrifuge	5430R	Eppendorf
Centrifuge	Heraeus Megafuge 40	Thermo Scientific
Chemiluminescence blot imager	ChemiDoc Touch Imaging System	Bio-Rad
CO_2 incubator	Heracell™ 150i #51032720	Thermo Scientific
Confocal microscope	LSM 710	Zeiss
Confocal microscope	LSM 780	Zeiss
Confocal microscope	TCS SP5	Leica
Cryostat	CM1950	Leica
Dry block heater	Dry Block Heater 1	IKA
Gel transferring cell	Mini Trans-Blot Cell #1703930	Bio-Rad

Gel documentation system	E-BOX VX2	Vilber
Flow cytometer	BD FACSCanto II	BD Biosciences
Flow cytometer	BD FACSAria Fusion	BD Biosciences
Inverted microscope for cell culture	Primovert	ZEISS
Microplate reader	Infinite® M Plex	Tecan
Microplate reader	Mitras LB940 plate reader	Berthold Technologies
Microplate reader	Omega	BMG-Labtech
Mini centrifuge	3-1810	neoLab
Orbital shaker ()	Infors Celltron HD	Infors HT
PCR machine	T100 Thermal Cycler	Bio-Rad
Polyacrylamide gel electrophoresis system	Mini-PROTEAN Tetra Vertical Electrophoresis for Handcast Gels (1.0 mm), 4-gel #1658001EDU	Bio-Rad
qPCR machine	LightCycler® 480 System	Roche
Safety cabinet	Safe 2020, MaxiSafe 2020	Thermo Scientific
Stereomicroscope for dissection	Stemi DV4	Zeiss
TEER machine	Millicell ERS-2 Voltohmmeter #MERS00002	Millipore
Thermomixer	Mixing Block MB-102	BIOER
Ultrapure water system	Barnstead™ GenPure™ Pro	Thermo Scientific
UV spectrophotometer	NanoDrop One	Thermo Scientific
Vibrating blade microtome	VT1000 S	Leica
Vortex mixer	Vortex-Genie 2	Scientific Industries
Wide field slide scanner	Axioscan 7	Zeiss
Wide field microscope	Cell Observer	Zeiss

5.2. Methods

5.2.1. Usage of human samples

De-identified healthy choroid plexuses (ChP) were provided by The Netherlands Brain Bank (Amsterdam, the Netherlands) and NIH Neurobiobank at the University of Maryland (Baltimore, MD, USA). De-identified choroid plexus tumours were acquired from the Nationales Centrum für Tumorerkrankungen (NCT) in Heidelberg and from the Institute of Neuropathology in Münster. The histopathology was evaluated based on the most recent WHO standards. The handling of all tissues and experiments were complied with ethical guidelines and regulations for the research use of human tissue issued by the Medical Faculty of the Heidelberg University (S-753/2019). Detailed information about all human samples is provided in Table 2.

5.2.2. Experimental animals

Inbred C57BL/6J and C57BL/6N mice were purchased from Janvier labs. GFP-tagged Otx2 mouse line was provided by Dr. Thomas Lamonerie [195]. P35 Spastin knockout (KO) mice were generated as described by Brill et al. 2016 [163]. P60 *Agbl4* (CCP6) KO mice were generated as described by Magiera et al. 2018 [164]. *Cent2*–GFP mice (CB6-Tg(CAG-EGFP/CETN2)3-4Jgg/J) [196] were purchased from The Jackson Laboratory and maintained on a C57Bl/6J background; both homozygous and heterozygous *Cent2*–GFP mice were used for experiments.

The studies encompassed both male and female mice, which were housed in cages devoid of environmental enrichment toys, but provided with additional Kimwipes tissue. Following weaning, the animals were housed in groups of 2-5 per cage, in a temperature- and humidity-controlled room, on a 12-hour light/12-hour dark cycle, and with *ad libitum* access to food and water. The animal experiments were authorized by the regulatory bodies of Germany, France, and the European Union, in compliance with the guidelines established by the local regional ethics committee (Regierungspräsidium Karlsruhe, Germany; the Government of Upper Bavaria; Comité d'éthique en expérimentation animale n°005; Institut Curie CEEA-IC #118 n° 04395.03 given by National Authority). Animal studies were reported in accordance with the ARRIVE guidelines.

5.2.3. Single and double S-phase labelling

Mated female mice were subjected to a daily examination between 6:30 and 7:30 AM to observe the presence of a vaginal plug. The midday of the day on which the plug was detected was considered E0.5. The weight of the female mice was recorded every other day to verify pregnancy. The EdU and BrdU solutions were freshly prepared on injection days by dissolving in 50°C sterile PBS to 6.15 mg/ml [197].

For single EdU labeling, pregnant mice were administered an intraperitoneal (i.p.) injection of 50 mg EdU/ 1 kg body weight at a particular development stage. As for double labeling, pregnant dams at E10.5-E16.5 were administered an i.p. injection of 50 mg EdU/1 kg body weight at around noon, followed by a second injection of 50 mg BrdU/1 kg body weight 24 hours later. Embryos were collected 24 hours post BrdU administration.

5.2.4. Plasmid vector construction and lentivirus production

sgRNA sequences targeting human *APC* and rat *Apc* gene were designed using E-CRISP tool [198]. The ligation of rat sgRNA into lentiCRISPRv2 puro and human sgRNA into lentiCRISPRv2 mCherry were performed following Zhang Lab's protocol [199]. Plasmids over-expressing human WNT3A were kindly provided by Prof. Dr. Michael Boutros. Sequences of sgRNA and Sanger sequencing primers are provided in Table 8.

For lentivirus production, HEK293T was seeded to reach 80-90% confluence on the 2nd day, then they were co-transfected with a mixture of 2 µg transfer plasmid, 1.32 µg psPAX2 and 0.66 µg VSV-G using polyethylenimine (PEI) in Opti-MEM. The volume ratio of PEI:transfer vector = 4:1. Media containing transfection mix was changed after 6-8 hours. 48 hours after transfection, viral supernatant could be collected and filtered through 0.45 µm PES filter. Virus supernatant could be used immediately or frozen and kept at -80°C. Frozen virus vials should be thawed slowly on ice.

5.2.5. Cell culture and generation of stable engineered cell lines

Z310 and HIBCPP cell lines were maintained in the corresponding media (Table 4). Cell counting for seeding/quantification was performed out by staining with Trypan Blue and automatic counting with LUNA-II cell counter. All cell lines were routinely checked for

mycoplasma contamination and only those younger than passage 32 were used for experiments.

To generate stable engineered cell lines, lentivirus carrying CRISPR-Cas9 or over-expressing construct was introduced into Z310 cells with 10 mg/ml polybrene. The *Apc*_KO lines were generated by selection with puromycin treatment and single clones isolation through limited dilution. WNT3A_OE was generated by single cell selection and sorting of GFP+ cells using FACSAria III cell sorter. Genetic modifications were validated through Sanger sequencing, while protein ablation/overexpression was confirmed by western blot. The engineered cell lines were maintained in the same media as the original lines.

For cell death and cell cycle analyses of HIBCPP: Cells were seeded on cell culture cover slips. When cells reached 50%-60% confluence, 6.5 µM WNT974 or DMSO was added. For apoptosis analysis, cells were incubated with WNT974 in 3 days, then undergone cleaved Caspase-3 staining procedure following the below immunofluorescence protocol. For proliferation analysis, cells were exposed to the drug for about 2.5 days, then 10 µM EdU was added to culture media and incubated for 4h. Cells were then washed with PBS and proceeded with EdU detection procedure using Click-iT EdU Cell Proliferation Kit for Imaging following manufacturer's protocol.

5.2.6. Organoid production and engineering

Human induced pluripotent stem cells (hiPSCs) were generated from skin fibroblasts of a healthy donor (44-year-old healthy female derived with given informed consent within the collaborative research center project SFB636 B7; ID number B7_028#4). iPSCs reprogramming were approved by Ethics Committee II of Heidelberg University, approval no. 2009-350N-MA for hiPSC generation.

Generation of hiPSC

hiPSCs were generated and cultured following protocol established in Jabali et al. 2022[200]. In brief, Sendai virus (SeV) vectors were used for skin fibroblasts reprogram by non-integrative delivery of OCT4, SOX2, KLF4, and c-MYC. hiPSCs were then cultured

as colonies on Geltrex-coated cell culture plates in Essential 8 medium with daily medium change.

Generation of ChP organoids

Human iPSCs were used to generate ChP organoids. On day 0, U-bottom 96-well plates were coated with 5% Pluronic F-127 in PBS for 15 minutes to create low attachment wells. Next, iPSC colonies were dissociated using TrypLE Express; cells were then seeded with the density of 6000 cells per low attachment well in 150 µl E8 medium supplemented with 50 µM Y-27632 to form embryoid bodies. Medium was changed every other day. On day 5, medium was switched to neural induction medium (Table 4). Medium change was done every other day.

On day 10, organoids were embedded in a droplet of about 25 µl GT and transferred into Pluronic-coated 6-cm dishes. Medium was switched to ChP-induction medium (Table 4) and changed again on day 13. On day 15, ChP organoids-containing dishes were transferred onto an orbital shaker and cultured with continuous agitation at 70 rpm. On day 17, BMP4 and CHIR99021 were removed and ChP induction medium was supplemented with 1:500 GT instead, followed by medium changes every 3 to 4 days.

Generation of engineered ChP organoids

Between days 40-45, ChP organoids were transduced with lentivirus delivering plasmids encoding either Cas9-sgRNAs-mCherry targeting the *APC* gene, or Cas9-mCherry as Control. For each well of Pluronic-coated 24-well plate, 5 organoids were transduced with 1:2 dilution of lentivirus and 10 µg/ml Polybrene (Santa Cruz #sc-134220) in a total volume of 500 µl medium. Organoids were incubated with the virus at 37°C for 24 hours before they are transferred back into ChP maturation medium in 6-cm dishes and further cultured under agitation. After 3 weeks of further culture, organoids were harvested and analyzed.

Conditioned media (CM) treatment of organoids

From days 40-45, treated organoids were cultured in ChP maturation medium containing either 5 µM CHIR99021 (Cell Guidance Systems #SM13). Control organoids were kept in normal ChP maturation medium. After 3 weeks of further culture, organoids were harvested and analyzed.

5.2.7. Organoid dissociation and 2D culture of FAC-sorted organoid cells

Organoids are washed with PBS, then dissociated with 9:1 enzyme mix of Accutase/Trypsin and incubated at 37°C for 4-5 minutes. PBS is then added to dilute the enzyme, and cell pellets were collected through centrifugation. Pellets were washed again with PBS and either stored for downstream analyses like qPCR, Western blot; or further processed for FAC-sorting.

For FAC-sorting experiments, dissociated organoid pellets were resuspended in PBS and passed through 70 µm filter. The filtrate was diluted in FACS buffer (Table 4), passed through 35 µm filter and mCherry positive cells from both the Control and *APC*_KO organoids were sorted using BD FACSAria Fusion (BD Biosciences). Sorted cells were cultured in Geltrex-coated plates with ChP maturation medium supplemented with 20% FBS. Cells were passaged when becoming confluent; all cells used in this study were younger than passage 7.

5.2.8. RT-qPCR

The starting materials are frozen cell pellets gathered from distinct wells/experiments, or pooled dissected mouse tChP and hChP tissue, or snap-frozen human specimens sliced with Leica CM1950 cryostat. Due to the small size of E16.5 mouse tissue, samples from 3 embryos were pooled for each biological replicate. RNA extraction was performed using RNeasy Mini Kit, following the manufacturer's protocol. RNase-free DNase I was used to remove the genomic DNA. RNA was eluted from the column with 30 µl RNase-free water and stored at -80 °C. RNA quality and concentration were assessed by UV spectrophotometry on NanoDrop One with the desired absorbance ratios A260/A280 and A260/A230 of 1.8-2.2. RNA samples with absorbance ratios below 1.8 were precipitated using glycogen, following the manufacturer's protocol.

cDNA synthesis was performed using the High-Capacity RNA-to-cDNA kit. The cDNA samples were stored at -20 °C. Subsequently, qPCR was carried out on 50-70 ng cDNA of each sample with PowerUp SYBR Green Master Mix in a 10 µl reaction volume. Thermal protocol following manufacturer's protocol with annealing temperature at 56 °C in 15 s. All RT-qPCR experiments were performed on LightCycler 480 for 384-well plate. Reference genes were *ACTB, HPRT*, and *RPL13A* for human samples and cell lines; *Hprt,*

Rpl13a for rat cell lines; and *Hprt, Rpl27, Rpl13a* for mouse samples. Primer sequences can be found in Table 7.

Raw data obtained from RT-qPCR without baseline correction was retrieved from the machine to be used as input for LinRegPCR [201] (version 2020.0). The software calculated a baseline correction for each sample individually whilst computing the amplification efficiency (E), quantification cycle (Cq) through the application of a linear regression model to the log-linear phase. Technical replicates were allowed for a maximum variation of Cq set at 0.5 and unqualified replicates were eliminated. If the panel was merged from 2 different plates, LinRegPCR output generated from two plates was subsequently fed into Factor-qPCR [201] (version 2020.0) to remove any systematic bias between different RT-qPCR runs. Ultimately, the Cq value representing biological samples was derived as the arithmetic mean of technical replicates. Relative expression level was calculated by Pfaffl method (or efficiency method) [202].

5.2.9. Western blot

The starting materials were either cell pellets washed with ice-cold PBS or 12 µm snap-frozen human specimens sliced using Leica CM1950 cryostat. For most experiments, cells/tissue were lysed in ice-cold NP buffer (Table 4). For the detection of DVL2 and activated β-catenin in human samples, snap-frozen tissue slices were lysed in buffer containing 2% SDS, 62.5mM Tris pH 6.8, 10% glycerol. Protein concentrations were determined using BCA assay and the same amount of protein were loaded on SDS-PAGE gels. For APC detection, 70-80 µg total proteins were loaded on 6% gel; for remaining proteins, 20-30 µg proteins were loaded on 8% gel. Electrophoresis was carried out in Running buffer (Table 4), starting with 70V in the first 15 minutes, then 100V in around 45 minutes. Blotting was carried out in Transfer buffer (Table 4) with constant current 0.37A in 1h45m at 4°C. 0.45 µm PVDF membrane activated in MeOH for 1 min was used for protein transfer. For antibodies against phosphorylated proteins, 5% BSA in TBST were used as blocking and antibody solutions. For remaining antibodies, 5% milk in TBST were used. Antibodies were detected using Chemiluminescence with HRP substrates Pierce ECL Substrate and WesternBright Chemiluminescence Substrate. Images were acquired with ChemiDoc Touch imaging system operated by Image Lab (v3.0.1.14). Information of antibodies are provided in Table 5.

5.2.10. Immunofluorescence staining

Processing and fixation:

For animal materials, whole embryos (E11.5 - E12.5), whole heads (E13.5 – E16.5) and dissected brains (E18.5 – P720) were rinsed in cold PBS and subsequently embedded in Tissue-Tek OCT before being frozen on dry ice and stored at -80°C. Tissues of double S-phase labeling experiment underwent a cold PBS rinse, followed by a 2-hour immersion in 4% PFA, an overnight cryoprotection in 30% sucrose, then embedded in OCT, frozen on dry ice and kept at -80°C. Frozen tissue blocks were sectioned into 15 µm segments on Superfrost slides.

Organoids were washed with PBS and then fixed in 4% PFA for 10 minutes, followed by embedding in a 10%/7.5% gelatin/sucrose solution, then frozen on dry ice and kept at -80°C. Frozen tissue/organoid blocks were sectioned into 20 µm segments on Superfrost slides.

Cultured cells (on coverslip) were washed with PBS and subsequently fixed in 4% PFA for 10 minutes prior to staining.

General staining procedure:

Fixed samples were blocked with a solution of 10% donkey serum and 0.5% TritonX-100 in PBS for 1 hour at room temperature. Antibodies were diluted in the antibody solution consisting of 3% donkey serum and 0.5% TritonX-100 in PBS. Primary antibody was incubated overnight at 4°C. Secondary antibody incubation was performed for 2 hours at room temperature. Nuclei were stained with Hoechst 33342 for 15 minutes at room temperature. Finally, coverslips were mounted on microscopic slides with Fluorescence Mounting Medium. Antibody information are provided in Table 5.

Special staining procedure:

Single S-phase labeling: Whole-mounts P25 choroid plexus were dissected, fixed in 4% PFA for 2 hours, then subsequently permeabilized and blocked in a solution containing 0.1% Triton X-100 and 10% fetal bovine serum in PBS for 1 hour. The EdU incorporation was detected through using Click-IT EdU Alexa Fluor imaging kit following the manufacturer's protocol. To determine the birthdate of Trp73+ cells, tissues were washed again and incubated overnight at 4°C with the Trp73 antibody. After incubation

with the secondary antibody for 2 hours and Hoechst staining, ChPs were mounted with Fluoromount-G mounting medium.

Double S-phase labeling: PFA-fixed sections were fixed a second time with 4% PFA for 10 minutes and then permeabilized with 1% Triton X-100 for 1 hour. Detection of EdU was carried out by employing the Click-iT EdU Imaging Kit in accordance with the manufacturer's protocol. Following this, the tissue was incubated with 37°C 2N HCl for 40 minutes to denature DNA for BrdU labeling. The HCl was subsequently neutralized using 1M Tris pH8.0. Afterwards, tissue was blocked and permeabilized (see above) and incubated with anti-BrdU overnight at 4°C. Secondary antibody labeling and later steps are similar to the above general procedure.

5.2.11. Immunofluorescence microscopy and image analysis

Most confocal microscopy images were acquired using a Zeiss LSM780 microscope with x40 or x63 objective. ZEN Black software was used for image acquisition. Images used for polyE quantification were acquired with a Leica SP5 microscope with x63 objective. Images were acquired with 2048 x 2048-pixel. For whole mount ChP, 3D confocal tilescan images of P25 whole ChP were acquired on an inverted LSM880 Airyscan Zeiss microscope with x20 0.8 plan-apochromat objective. Images were stitched together to reconstruct the whole plexus as prepared on cover slips. Wide field images were acquired using Zeiss Axioscan 7 (Zeiss, Germany) at x20 magnification. Images were analyzed using Fiji.

Automatic segmentation and analysis of choroidal plexus cells: a 3D segmentation was performed independently on each channel (Hoechst, EdU and Trp73) to obtain a 3D mask from each labeled nucleus with a Fiji macro developed for the Automatic image analysis of MAGIC Markers [203]. Briefly, a 3D Gaussian filtering with a sigma set to 1/3rd of the estimated nuclear radius was first applied on the Hoechst channel to remove noise. This pre-processing was then followed by a Log3D filtering [204] to emphasize only the objects approximately matching the nuclear size. Following this, a threshold was applied to remove the background and 3D maxima were detected to localize the centre of each nucleus on the foreground. Finally, a 3D-seeded watershed segmentation was performed from these maxima to accurately split touching nuclei and obtain an accurate voxel mask for each nucleus on each channel if present. A script in python was then used to retrieve

the mean intensity levels of Trp73 and EdU channels within each cell mask defined by Hoechst. A cell was considered positive for Trp73 or EdU when signal in these channels remained in the Hoechst mask after the detection step and negative otherwise.

Quantification of EdU+ and Trp73+ cells in P25 choroid plexus: total number of EdU and Trp73 positive cells were quantified at each time point, percentages of Trp73+ cells was calculated based on total number of Hoechst cells, and percentage of Trp73+EdU+ cells was calculated on total number of Hoechst cells.

EdU positive cells density maps overtime: using dedicated Python scripts, tilescan images of each plexus was divided in small bins of 60x60 pixels. A count of Trp73+ EdU+ cells was retrieved from each of these bins and represented as a single grey level pixel in a new 60 times smaller image. The whole intensity of this small image was then divided by the total cell count of the slide thus resulting in one density map for each replicate choroid plexus slide. From this point, each replicate choroid plexus was split in two and processed separately. For each half ChP, all the 3x8 replicates shape contours were parameterized with 300 points thanks to a parametric contour algorithm developed in Laruelle et al., 2020 [205]. These contours were then all associated together to find an optimal match between all couples of them. Once aligned, an average shape contour was computed. The content of all density maps previously obtained were then morphed into this average shape using the Mean Value Coordinates routine also implemented in this previous work [205]. The 3 morphed replicates per time point were then averaged to finally obtain a single density map of cell division at each age per half ChP. Half ChP images at each age were reassembled to produce the animation presented as supplementary video.

Double S-phase: whole ChP tissue was acquired using 40x oil objective with tile-stitch module of 10% overlap and z-stack projection of 3-5 µm range. The number of EdU+ and BrdU+ cells located in the neuroepithelial layer was quantified from the ventricular wall to the tip of the tChP. The percentage of cells re-entering cell cycle was calculated as (EdU+BrdU+)/EdU+ cells.

Cilia apparatus: Selective ChP regions (bottom, mid and tip based on distance from ventricular wall) were acquired with 63x oil objective, zoom 2, z-stack projection of 0.35 m interval. All images were acquired for the entire penetration of the antibodies to ensure the full reconstruction of cilia apparatus. Cell density, number of axonemes and basal bodies were quantified using Cell Counter plug-in. Cilia length was manually

measured in max intensity projection images. For GT355 and polyE expression analysis the mean pixel intensity of the single channel signal in each field was measured using Fiji [206].

Super-resolution/STED microscopy images were acquired with an Abberior Instruments FACILITY LINE STED microscope equipped with an inverted IX83 microscope (Olympus), a 60x oil objective (UPlanXApo 60x/1.42 oil, Olympus), using pulsed excitation lasers at 561 nm and 640 nm and a pulsed STED laser operating at 775 nm at 40-MHz repetition rate. All acquisition parameters were controlled via the Lightbox Software (Abberior Instruments).

All images were processed and analyzed with ImageJ (Fiji, NIH) [206].

5.2.12. Transmission electron microscopy (TEM) and serial section (ss)TEM

For E16.5 (n = 4) and P60 (n = 3) tissue: The ChP was dissected and fixed with 2.5% glutaraldehyde in cacodylate buffer. They were post-fixed for 1-2 hours in the same fixative at 4°C. After washing in PB 0.2 M, the ChP was post-fixed in osmium ferrocyanide (1 volume of 2% aqueous osmium tetroxide: 1 volume of 3% potassium ferrocyanide) for 1 hour at 4°C, dehydrated for 15 minutes in increasing concentrations of acetone (30%, 60%, 90%, 100%), incubated in acetone/Spurr resin (1:1, 30 minutes, 1:2, 30 minutes) and in Spurr resin (Sigma-Aldrich) at room temperature (RT) overnight. Finally, the ChP was embedded in Spurr resin in capped 00 BEEM capsules (Electron Microscopy Sciences) for 24 hours at 70°C.

For E15.5 and P45 tissue: The ChP was dissected and fixed with 2.5% glutaraldehyde in PBS for 2 hours at 4°C. After washing in PBS, the ChP was post-fixed in 1% osmium tetroxide for 1 hour at 4°C, dehydrated for 10 minutes in increasing concentration of ethanol (30%, 50%, 70%) and incubated in 1% uranyl acetate in 70% methanol, before final dehydration in ethanol (90%, 100%) then acetone (100% three times). Samples were then incubated in acetone/Araldite 502 resin (2:1, 40 minutes, 1:1, 40 minutes, 1:2, 40 minutes) and in Araldite 502 resin at RT overnight. Finally, the ChP was embedded in Araldite 502 resin, mounted flat between two sheets of Aclar 33C (Electron Microscopy Sciences) for 48 hours at 60°C.

For organoid: Whole organoids were fixed with 2.5% glutaraldehyde and 2% PFA in 0.1 M cacodylate buffer (CB), pH 7.4, overnight at 4°C. They were rinsed on the next day with CB and stored overnight at 4°C. Organoids were then post-fixed in 1% osmium tetroxide in CB for 1 h at 4°C, washed with distilled water and dehydrated in an ascending ethanol series (30%, 50%, 70%, 90%, 100%). Next, they were incubated in propylene oxide for 10 min, infiltrated and embedded in EPON 812.

Ultrathin sections were cut with an ultramicrotome (EM UC6, Leica Microsystems), collected on uncoated nickel grids (100 mesh) or on formvar coated nickel grids (2x1 mm slot) and counterstained for 30 seconds with UranyLess EM Stain and 30 seconds with lead citrate (Electron Microscopy Sciences). Sections were observed with a JEM1400 Flash transmission electron microscope (JEOL, Tokyo, Japan) or a Tecnai T12 transmission electron microscope (FEI-ThermoFisher), and images were acquired with a high-sensitivity sCMOS camera or a CCD camera (Gatan). ssTEM 3D modelling of cilia was performed with the IMOD software [207].

Epithelial choroid plexus cells (n = 613 in total; 3 P60 mice) were selected such that both apical and basal borders of the cells were visible, and nucleus was at its best fit. The cilia quantification analysis was performed manually with ImageJ (Fiji, NIH) [206]. Micrographs alignment and segmentation of basal bodies, basal feet, distal appendages and axonemes was performed manually with IMOD.

5.2.13. Luciferase reporter assay

Cells were seeded in 96-well plate in triplicate with the quantity per well ensures 80%-100% confluent after 4 days in culture. On the second day after seeding, a plasmid mix of 30 ng Firefly luciferase (TOPFlash), 20 ng Renilla luciferase and 50 ng pcDNA3 were transfected into cells using Lipofectamine and OptiMEM. Where needed, WNT3A or DKK1 conditioned media or control media was added on the third day. On the fourth day, cells were washed with PBS, lysed on the plate using P/Rluc lysis buffer (Table 4). Dual luciferase assay was performed in white, flat-bottom 96-well plates with Firely and Renilla substrate solutions (Table 4) following a previously published protocol [208]. Luminescence signal was measured using Mithras LB940 plate reader. Relative luminescence unit was calculated as Firefly luminescence normalized to Renilla luminescence and averaged across triplicates.

5.2.14. MTT assay

Cells were seeded in 96-well plates. After reaching 40%-60% confluency in 1-2 days, old media was removed and drug-containing media was added. HIBCPP cells were treated with a serial dilution of 0–400 µM WNT974 for 3 days. Z310 *Apc*_KO cells were treated with a serial dilution of 0–100 µM Doxorubicin for 2 days. After that, cells were washed and 100 µl of FBS-free media containing 500 µg/ml MTT was added. After 2.5–3h incubation at 37°C in dark environment, MTT media was removed and DMSO was added. Plates were then put on the shaker at room temperature for 15 mins before the colorimetric signal was read with an OD570 by Tecan Infinite 200 Plate reader.

5.2.15. Clonogenic assay

HIBCPP cells were seeded in 6-cm dish. After cells reach 50%-60% confluency, 3 and 6.5 µM WNT974 were added. DMSO was used for control condition. After three days in culture, cells were detached using Trypsin and counted for viable cells. Subsequently, 7000 cells/well were seeded into 6-well plates. When colonies reached the size of >50 cells/colony (after around four weeks), cells were washed with PBS, fixed in cold MeOH for 5 min and stained with 0.01% Crystal Violet in 10% MeOH for 15 mins. Plates were washed with water and let dry, then scanned using Epson Perfection V370 scanner. Images were contrasted and colonies were quantified using Fiji.

5.2.16. Soft agar colony formation assay

Low-melting agarose was dissolved in normal cell culture media. A 6-well plate was prepared by adding 1.5 ml of 0.6% agarose/media to coat the bottom. Once the layer became solid, 7500 cells were seeded into each well using 0.3% agarose/media to ensure the separation of individual cells. The cells were incubated at 37°C to proliferate in a semi-solid environment, whereby 200 µl of media was added to the top layer every other day to maintain moisture. Following 3-4 weeks, colonies from each single cell emerged, and cold MeOH was added for fixation. The colonies were stained with 0.01% Crystal Violet in 10% MeOH for 15 min, then gently washed with water to avoid damaging the agar layer and cell colonies. Scanning of the plates was performed using an Epson Perfection V370 scanner (Epson). Finally, Fiji was utilized for image contrast and colony quantification.

5.2.17. Spheroid formation and organotypic brain slice invasion assay

The experiment was carried out in accordance with the previously published protocol [124]. In short, a total of 1E+6 cells were stained with DiI dye at a concentration of 1 mg/ml and incubated at 37°C for 30 minutes. Next, 600 cells/well were seeded onto 96-well plates that were coated with 1% low-melting agarose. On day 3, fresh 350 µm-thick coronal sections were obtained from the brains of 6-week-old C57Bl/6 mice and placed onto filters with brain slice media. On the fourth day, spheroids were implanted into the brain slices and maintained at 37°C for 2 days. Subsequently, brain slices were fixed with 4% PFA at 4°C overnight, then serially cleared in 20%-115% D-fructose-based solution at RT. The fluorescence signal of the implanted spheroids was captured in z-stack mode at x10 magnification using a Zeiss LSM780 confocal microscope. The normalized invasion area was calculated as the total area of protrusions over the spheroid size.

5.2.18. Flow cytometry analysis of cell death and cell cycle progression

HIBCPP cells were seeded so that they reach 50%-60% confluent after 2 days, 6.5 µM WNT974 or DMSO was then added to culture media. Cells treated with 1.5 µM Doxorubicin was used as positive control. After 3 days incubation, cells were detached using TrypLE and counted for viable cells.

For apoptosis analysis, cells were first washed with cold Cell Staining Buffer, then stained for Annexin V and Propidiumiodide using FITC Annexin V Apoptosis Detection Kit with PI following manufacturer's protocol.

For cell cycle progression analysis, cells were first washed with PBS, then cold 70% Ethanol was added drop-wise while vortexing for fixation. Cells were then incubated at -20°C for 1h, washed and re-suspended in PBS at the concentration 1E+6 cells/ml. 50 µg/ml RNase A was then added and cells were incubated at 37°C for 30 min. Next, 50 µg/ml Propidiumiodide (PI) was added and cells were incubated at RT for 5 min.

Flow cytometry analyses were performed using BD FACSCanto II. Fluorescence signal of FITC and PI were collected using 530/30 and 585/42 nm filters, respectively. 20000-22000 events were recorded for apoptosis experiments. 10000-12000 events were

recorded for cell cycle experiments. FlowJo software was used for data analysis. The proportions of cells in each cell cycle phase were determined by Dean-Jett-Fox model.

5.2.19. Immunohistochemistry

Hematoxylin and Eosin (H&E) staining: 20 µm organoid sections were dehydrated in an ascending ethanol series (50%-100%). Staining procedure was carried out with H&E Fast Staining Kit following manufacturer's protocol. Slides were mounted with Eukitt mounting solution; images were acquired using Zeiss Axioscan 7 at x20 magnification and analyzed with Fiji.

β-catenin staining: 3 µm sections of formalin-fixed paraffin-embedded (FFPE) human tissues were stained for mouse anti-β-catenin on the automated stainer BenchMark ULTRA Autostainer. In brief, the staining procedure started with heat-induced epitope retrieval pretreatment using CC1 buffer (95 °C; 24 min), then samples were incubated with primary antibody for 32 min. Signal detection was carried out using the OptiView DAB IHC Detection Kit following the manufacturer's instructions. Images were analyzed using Fiji. The numbers of cells positive for β-catenin within each cellular compartment were quantified with Cell Counter plug-in. The intensity of β-catenin signal was pseudo-quantified by 2 independent evaluators blinded of sample types. A random field of ChP stained with β-catenin was selected as standard, 5-8 fields per sample were scored for β-catenin intensity as compared to the standard: -2: much weaker, -1: weaker, 0: similar, 1: stronger, 2: much stronger. Presented data are averaged scores.

5.2.20. Microarray and WGS data analyses

Published microarray data GSE14098 was downloaded from the repository NCBI GEO (Gene Expression Omnibus). Differentially expressed genes (DEGs) were analyzed using limma package. Statistics significance was adjusted with Benjamini – Hochberg's method and Cut-off value for DEGs filtering was $|logFC| \geq 1$. DEG data of genes with $|logFC| \geq 1.5$ was then used as input for pathway analysis with Ingenuity Pathway Analysis (IPA) (Qiagen).

Children's Brain Tumor Tissue Consortium (CBTTC). Sample information could be found in Table 13. The data were converted back to fastq files of unaligned reads, then re-alignment and downstream analyses were conducted using in-house workflows

integrated in the Roddy framework, which has been developed by the Omics IT and Data Management Core Facility (ODCF) at the DKFZ [103]. Detailed workflows and documentation could be found at https://github.com/TheRoddyWMS/Roddy. SNV and Indel output data was filtered so that variants with allele frequency (AF) ≥ 1% (with reference to the 1000 Genomes Project) were eliminated. The Wnt2GOs gene list is combined from GO:0060070 Canonical Wnt signaling pathway, GO:0060828 Regulation of canonical Wnt signaling pathway. For SNVs and Indels analyses, Wnt2GOs list was used to subset genes involved in Wnt/β-catenin pathway from the filtered dataset. For SV analyses, Wnt2GOs list was used to subset genes involved in Wnt/β-catenin pathway from the list of genes immediately before and after the breakpoints. Additional Gene Ontologies applied in this study have been restricted to species Homo sapiens and include: GO:0060070 Canonical Wnt signaling pathway, GO:0060828 Regulation of canonical Wnt signaling pathway, GO:0030509 BMP signaling pathway, GO:0030510 Regulation of BMP signaling pathway, GO:0007173 epidermal growth factor receptor signaling pathway, GO:0042058 Regulation of epidermal growth factor receptor signaling pathway, GO:0035329 Hippo signaling, GO:0035330 Regulation of Hippo signaling, GO:0007219 Notch signaling pathway, GO:0008593 Regulation of Notch signaling pathway, GO:0048008 Platelet-derived growth factor receptor signaling pathway, GO:0010640 Regulation of platelet-derived growth factor receptor signaling pathway, GO:0007265 Ras protein signal transduction, GO:0046578 Regulation of Ras protein signal transduction, GO:0007224 Smoothened signaling pathway, GO:0008589 Regulation of smoothened signaling pathway. Variants' effects were predicted using Ensembl VEP tool [209].

All data interpretation and visualization were performed in R 4.1.0

5.2.21. snRNA sequencing analyses

For snRNA sequencing data analysis, the matrix, features and barcodes files were downloaded from NCBI GEO (GSE168704) [6] and reconstructed into a SingleCellExperiment object using DropletUtils. SingleCellExperiment package was used for storing and retrieving data from the S4 object. Data quality control, dimensionality reduction and visualization was performed using package scater. Data normalization and modeling gene variance by expression was performed with scran, the top 2000 most variable genes were selected to perform Principal Component Analysis (PCA). As

suggested in the original paper, X inactivation and Y chromosome genes were removed. The top 10 PCA were used for UMAP dimension reduction with n-neighbors = 15. Cell annotations were retained from the original analysis in Cell Metadata. All epithelial cells were subtracted and used for subsequent analyses. DESeq2 package with shrinkage method *lfcShrink type = ashr* was applied to analyze differentially expressed genes (DEG) of epithelial cells. The gene list of GO term Cilium Organization (GO: 0044782) was expanded by adding selected genes, including cilia PTMs and cilia disassembly (p-value < 0.05). The same DEG analysis pipeline was performed for 3 ventricles, collectively and separately.

5.2.22. DNA Methylation analysis

DNA isolation was performed on FFPE samples using Maxwell 16 Tissue DNA Purification Kit (Promega, #AS1030). Purification and bisulfite conversion were performed using standard protocols provided by the manufacturer. Samples were analyzed using the MethylationEPIC BeadChip array.

5.2.23. Data and software availability

Several macros were created using the ImageJ and Python language to segment 3D nucleus and compute staining colocalization. Scripts in Python using the SET library (available from https://github.com/biocompibens/cellmodelling) were used to perform the alignment and morphing of the EdU density maps.

5.2.24. Statistical analysis

Statistical analysis was performed using GraphPad Prism. Appropriate statistical tests were selected based on the distribution of data and sample size. Parametric tests (One- and Two-Way ANOVA) were used only if data were normally distributed. Otherwise, nonparametric alternatives were chosen (Mann-Whitney and Kruskal-Wallis). Data are presented as mean ± standard error of the mean (SEM). P values in the manuscript present the following star code: ns: $p > 0.05$ (non-significant), *$p<0.05$, **$p<0.01$, ***$p<0.001$. The specific statistical test used is indicated in each figure legend.

6. Supplementary information

Table 13: Information of human samples used for whole genome sequencing in CBTTC database

ID_this study	Gender	Race	Ethnicity	Kids First Participant ID	Disease_type	Sample_id	Tumor Descriptor	Sample_ type	Kids First Biospecimen ID_Tumor	Kids First Biospecimen ID_Matched blood control	Primary_site	Age_at_ diagnosis_day
CPC1	Female	White	Not Hispanic or Latino	PT_7TRGHZBK	Choroid plexus carcinoma	7316-431	Initial CNS Tumor	Tumor	BS_XEVMEYFS	BS_HNWNZFHA	Parietal Lobe	1098
CPC2	Female	White	Not Hispanic or Latino	PT_YZ8A8A36	Choroid plexus carcinoma	7316-723	Initial CNS Tumor	Tumor	BS_59FR1NC2	BS_7XEH55CB	Frontal Lobe;Other locations NOS;Parietal Lobe;Temporal Lobe;Ventricles	643
CPC3	Female	White	Not Hispanic or Latino	PT_3WA7SBQ6	Choroid plexus carcinoma	7316-2248	Recurrence	Tumor	BS_HN8DE43A	BS_VJ7200DX	Parietal Lobe	698
CPP3	Male	White	Not Hispanic or Latino	PT_ZZ8SBJJ5	Choroid plexus papilloma	7316-725	Progressive	Tumor	BS_CPZZR2R7	BS_D3VQDD5A	Temporal Lobe;Ventricles	881
CPP4	Female	White	Not Hispanic or Latino	PT_YBJYA2CD	Choroid plexus papilloma	7316-2244	Initial CNS Tumor	Tumor	BS_KFRBXXV7	BS_N2TDDQ9Y	Ventricles	5456
CPP5	Male	Reported Unknown	Not Reported	PT_GKSABESN	Choroid plexus papilloma	7316-3485	Initial CNS Tumor	Tumor	BS_GRECE8Q9	BS_D64Q07W9	Ventricles	108
CPP6	Female	White	Not Hispanic or Latino	PT_ZS2YDFBE	Choroid plexus papilloma	7316-2860	Initial CNS Tumor	Tumor	BS_P6NWC51S	BS_EE7684YB	Ventricles	5917
CPP8	Female	White	Not Hispanic or Latino	PT_PHKSYE6Q	Choroid plexus papilloma	7316-220	Initial CNS Tumor	Tumor	BS_Y9GHDZKS	BS_BE3DW3RB	Ventricles	4957
CPP9	Female	Reported Unknown	Hispanic or Latino	PT_QJ3144WH	Choroid plexus papilloma	7316-3204	Initial CNS Tumor	Tumor	BS_8BS10XE2	BS_KGG1WDT8	Ventricles	6330
CPP10	Female	White	Not Hispanic or Latino	PT_AYZA2WCW	Choroid plexus papilloma	7316-197	Initial CNS Tumor	Tumor	BS_0Q8G4N8H	BS_T20VY3XN	Ventricles	3206
CPP12	Female	White	Not Hispanic or Latino	PT_JN3S17B3	Choroid plexus papilloma	7316-1693	Initial CNS Tumor	Tumor	BS_1EYKDS0Z	BS_1MMZN94J	Ventricles	4308

CPP13	Male	Reported Unknown	Not Reported	PT_GY99ZJHV	Choroid plexus papilloma	7316-1654	Unavailable	Tumor	BS_17FVWMNV	BS_61AK2H2N	Ventricles	670
CPP14	Female	Reported Unknown	Not Reported	PT_HN0AXSZ0	Choroid plexus papilloma	7316-1103	Initial CNS Tumor	Tumor	BS_Z34PQDYT	BS_SSVBWYPN	Cerebellum/Posterior Fossa	7197
CPP15	Male	White	Not Hispanic or Latino	PT_13MKXR8G	Choroid plexus papilloma	7316-2251	Initial CNS Tumor	Tumor	BS_CXCKHP3Z	BS_YXPWKF92	Ventricles	3470
CPP16	Male	White	Not Hispanic or Latino	PT_90W4HCNR	Choroid plexus papilloma	7316-2672	Initial CNS Tumor	Tumor	BS_M1TDS9CT	BS_GAFJBRM5	Ventricles	360

Bibliography

[1] S. A. Liddelow, "Fluids and barriers of the CNS: A historical viewpoint," *Fluids and Barriers of the CNS*, vol. 8, no. 1. Jan. 18, 2011. doi: 10.1186/2045-8118-8-2.

[2] N. R. Saunders, K. M. Dziegielewska, R. M. Fame, M. K. Lehtinen, and S. A. Liddelow, "THE CHOROID PLEXUS: A MISSING LINK IN OUR UNDERSTANDING OF BRAIN DEVELOPMENT AND FUNCTION," *Physiological Reviews*, vol. 103, no. 1. American Physiological Society, pp. 919–956, 2023. doi: 10.1152/physrev.00060.2021.

[3] F. Lamanna *et al.*, "A lamprey neural cell type atlas illuminates the origins of the vertebrate brain," *Nat Ecol Evol*, vol. 7, no. 10, pp. 1714–1728, Sep. 2023, doi: 10.1038/s41559-023-02170-1.

[4] M. P. Lun, E. S. Monuki, and M. K. Lehtinen, "Development and functions of the choroid plexus-cerebrospinal fluid system," *Nature Reviews Neuroscience*, vol. 16, no. 8. Nature Publishing Group, pp. 445–457, Jul. 20, 2015. doi: 10.1038/nrn3921.

[5] W. Brooks Quay, "Regional differences in metabolism and composition of choroid plexuses," *Brain Res*, vol. 2, no. 4, pp. 378–389, Oct. 1966, doi: 10.1016/0006-8993(66)90007-2.

[6] N. Dani *et al.*, "A cellular and spatial map of the choroid plexus across brain ventricles and ages.," *Cell*, vol. 184, no. 11, pp. 3056-3074.e21, May 2021, doi: 10.1016/j.cell.2021.04.003.

[7] J. Praetorius and H. H. Damkier, "Transport across the choroid plexus epithelium," *American Journal of Physiology-Cell Physiology*, vol. 312, no. 6, pp. C673–C686, Jun. 2017, doi: 10.1152/ajpcell.00041.2017.

[8] K. H. Ho *et al.*, "Choroid plexuses carry nodal-like cilia that undergo axoneme regression from early adult stage," *Dev Cell*, vol. 58, no. 23, pp. 2641-2651.e6, Dec. 2023, doi: 10.1016/j.devcel.2023.10.003.

[9] T. Thomas and M. Dziadek, "Capacity to form choroid plexus-like cells in vitro is restricted to specific regions of the mouse neural ectoderm.," *Development*, vol. 117, no. 1, pp. 253–62, Jan. 1993, doi: 10.1242/dev.117.1.253.

[10] J. Wilting and B. Christ, "An experimental and ultrastructural study on the development of the avian choroid plexus.," *Cell Tissue Res*, vol. 255, no. 3, pp. 487–94, Mar. 1989, doi: 10.1007/BF00218783.

[11] D. S. Currle, X. Cheng, C.-M. Hsu, and E. S. Monuki, “Direct and indirect roles of CNS dorsal midline cells in choroid plexus epithelia formation.,” *Development*, vol. 132, no. 15, pp. 3549–59, Aug. 2005, doi: 10.1242/dev.01915.

[12] M. G. ’ ’Netsky and S. Shuangshoti, *The Choroid Plexus in Health and Disease*. University Press of Virginia, 1975.

[13] S. A. Liddelow, K. M. Dziegielewska, J. L. VandeBerg, and N. R. Saunders, “Development of the lateral ventricular choroid plexus in a marsupial, Monodelphis domestica,” *Cerebrospinal Fluid Res*, vol. 7, no. 1, p. 16, Dec. 2010, doi: 10.1186/1743-8454-7-16.

[14] Y. Furuta, D. W. Piston, and B. L. Hogan, “Bone morphogenetic proteins (BMPs) as regulators of dorsal forebrain development.,” *Development*, vol. 124, no. 11, pp. 2203–12, Jun. 1997, doi: 10.1242/dev.124.11.2203.

[15] E. A. Grove, S. Tole, J. Limon, L. Yip, and C. W. Ragsdale, “The hem of the embryonic cerebral cortex is defined by the expression of multiple Wnt genes and is compromised in Gli3-deficient mice.,” *Development*, vol. 125, no. 12, pp. 2315–25, Jun. 1998, doi: 10.1242/dev.125.12.2315.

[16] S. M. Lee, S. Tole, E. Grove, and A. P. McMahon, “A local Wnt-3a signal is required for development of the mammalian hippocampus.,” *Development*, vol. 127, no. 3, pp. 457–67, Feb. 2000, doi: 10.1242/dev.127.3.457.

[17] P. Kompaníková and V. Bryja, “Regulation of choroid plexus development and its functions.,” *Cell Mol Life Sci*, vol. 79, no. 6, p. 304, May 2022, doi: 10.1007/s00018-022-04314-1.

[18] F. Casoni *et al.*, “ZFP423 regulates early patterning and multiciliogenesis in the hindbrain choroid plexus.,” *Development*, vol. 147, no. 22, Nov. 2020, doi: 10.1242/dev.190173.

[19] M. B. Langford, C. J. O’Leary, L. Veeraval, A. White, V. Lanoue, and H. M. Cooper, “WNT5a Regulates Epithelial Morphogenesis in the Developing Choroid Plexus,” *Cerebral Cortex*, vol. 30, no. 6, pp. 3617–3631, May 2020, doi: 10.1093/cercor/bhz330.

[20] K. Kaiser *et al.*, “MEIS-WNT5A axis regulates development of fourth ventricle choroid plexus.,” *Development*, vol. 148, no. 10, May 2021, doi: 10.1242/dev.192054.

[21] A. Parichha *et al.*, “Constitutive activation of canonical Wnt signaling disrupts choroid plexus epithelial fate.,” *Nat Commun*, vol. 13, no. 1, p. 633, Feb. 2022, doi: 10.1038/s41467-021-27602-z.

[22] R. C. Rubin, E. S. Henderson, A. K. Ommaya, M. D. Walker, and D. P. Rall, "The production of cerebrospinal fluid in man and its modification by acetazolamide.," *J Neurosurg*, vol. 25, no. 4, pp. 430–6, Oct. 1966, doi: 10.3171/jns.1966.25.4.0430.

[23] R. W. Cutler, L. Page, J. Galicich, and G. V Watters, "Formation and absorption of cerebrospinal fluid in man.," *Brain*, vol. 91, no. 4, pp. 707–20, 1968, doi: 10.1093/brain/91.4.707.

[24] E. M. Wright, "Transport processes in the formation of the cerebrospinal fluid.," *Rev Physiol Biochem Pharmacol*, vol. 83, pp. 3–34, 1978.

[25] Z. B. Redzic, J. E. Preston, J. A. Duncan, A. Chodobski, and J. Szmydynger-Chodobska, "The choroid plexus-cerebrospinal fluid system: from development to aging.," *Curr Top Dev Biol*, vol. 71, pp. 1–52, 2005, doi: 10.1016/S0070-2153(05)71001-2.

[26] P. D. Brown, S. L. Davies, T. Speake, and I. D. Millar, "Molecular mechanisms of cerebrospinal fluid production.," *Neuroscience*, vol. 129, no. 4, pp. 957–70, 2004, doi: 10.1016/j.neuroscience.2004.07.003.

[27] A. B. Steffensen *et al.*, "Cotransporter-mediated water transport underlying cerebrospinal fluid formation.," *Nat Commun*, vol. 9, no. 1, p. 2167, Jun. 2018, doi: 10.1038/s41467-018-04677-9.

[28] E. Kokovay *et al.*, "VCAM1 is essential to maintain the structure of the SVZ niche and acts as an environmental sensor to regulate SVZ lineage progression.," *Cell Stem Cell*, vol. 11, no. 2, pp. 220–30, Aug. 2012, doi: 10.1016/j.stem.2012.06.016.

[29] A. C. Delgado *et al.*, "Endothelial NT-3 delivered by vasculature and CSF promotes quiescence of subependymal neural stem cells through nitric oxide induction.," *Neuron*, vol. 83, no. 3, pp. 572–85, Aug. 2014, doi: 10.1016/j.neuron.2014.06.015.

[30] K. Sawamoto *et al.*, "New neurons follow the flow of cerebrospinal fluid in the adult brain.," *Science*, vol. 311, no. 5761, pp. 629–32, Feb. 2006, doi: 10.1126/science.1119133.

[31] K. Baruch *et al.*, "Aging. Aging-induced type I interferon response at the choroid plexus negatively affects brain function.," *Science*, vol. 346, no. 6205, pp. 89–93, Oct. 2014, doi: 10.1126/science.1252945.

[32] V. Silva-Vargas, A. R. Maldonado-Soto, D. Mizrak, P. Codega, and F. Doetsch, "Age-Dependent Niche Signals from the Choroid Plexus Regulate Adult Neural Stem Cells.," *Cell Stem Cell*, vol. 19, no. 5, pp. 643–652, Nov. 2016, doi: 10.1016/j.stem.2016.06.013.

[33] S. Sugiyama *et al.*, “Experience-dependent transfer of Otx2 homeoprotein into the visual cortex activates postnatal plasticity.,” *Cell*, vol. 134, no. 3, pp. 508–20, Aug. 2008, doi: 10.1016/j.cell.2008.05.054.

[34] T. Toda *et al.*, “Birth regulates the initiation of sensory map formation through serotonin signaling.,” *Dev Cell*, vol. 27, no. 1, pp. 32–46, Oct. 2013, doi: 10.1016/j.devcel.2013.09.002.

[35] J. R. Pappenheimer, T. B. Miller, and C. A. Goodrich, “Sleep-promoting effects of cerebrospinal fluid from sleep-deprived goats.,” *Proc Natl Acad Sci U S A*, vol. 58, no. 2, pp. 513–7, Aug. 1967, doi: 10.1073/pnas.58.2.513.

[36] F. H. Martin, J. R. Seoane, and C. A. Baile, “Feeding in satiated sheep elicited by intraventricular injections of CSF from fasted sheep.,” *Life Sci*, vol. 13, no. 2, pp. 177–84, Jul. 1973, doi: 10.1016/0024-3205(73)90193-8.

[37] E. S. Maywood, J. E. Chesham, J. A. O’Brien, and M. H. Hastings, “A diversity of paracrine signals sustains molecular circadian cycling in suprachiasmatic nucleus circuits.,” *Proc Natl Acad Sci U S A*, vol. 108, no. 34, pp. 14306–11, Aug. 2011, doi: 10.1073/pnas.1101767108.

[38] C. R. A. Santos, A. C. Duarte, A. R. Costa, J. Tomás, T. Quintela, and I. Gonçalves, “The senses of the choroid plexus.,” *Prog Neurobiol*, vol. 182, p. 101680, Nov. 2019, doi: 10.1016/j.pneurobio.2019.101680.

[39] P. Solár, A. Zamani, L. Kubíčková, P. Dubový, and M. Joukal, “Choroid plexus and the blood-cerebrospinal fluid barrier in disease.,” *Fluids Barriers CNS*, vol. 17, no. 1, p. 35, May 2020, doi: 10.1186/s12987-020-00196-2.

[40] R. F. Keep and H. C. Jones, “A morphometric study on the development of the lateral ventricle choroid plexus, choroid plexus capillaries and ventricular ependyma in the rat.,” *Brain Res Dev Brain Res*, vol. 56, no. 1, pp. 47–53, Oct. 1990, doi: 10.1016/0165-3806(90)90163-s.

[41] J.-F. Ghersi-Egea, N. Strazielle, M. Catala, V. Silva-Vargas, F. Doetsch, and B. Engelhardt, “Molecular anatomy and functions of the choroidal blood-cerebrospinal fluid barrier in health and disease.,” *Acta Neuropathol*, vol. 135, no. 3, pp. 337–361, Mar. 2018, doi: 10.1007/s00401-018-1807-1.

[42] H. Xu *et al.*, “Choroid plexus NKCC1 mediates cerebrospinal fluid clearance during mouse early postnatal development.,” *Nat Commun*, vol. 12, no. 1, p. 447, Jan. 2021, doi: 10.1038/s41467-020-20666-3.

[43] C. Sadegh *et al.*, "Choroid plexus-targeted NKCC1 overexpression to treat post-hemorrhagic hydrocephalus.," *Neuron*, vol. 111, no. 10, pp. 1591-1608.e4, May 2023, doi: 10.1016/j.neuron.2023.02.020.

[44] J. Praetorius and S. Nielsen, "Distribution of sodium transporters and aquaporin-1 in the human choroid plexus.," *Am J Physiol Cell Physiol*, vol. 291, no. 1, pp. C59-67, Jul. 2006, doi: 10.1152/ajpcell.00433.2005.

[45] K. Oshio, H. Watanabe, Y. Song, A. S. Verkman, and G. T. Manley, "Reduced cerebrospinal fluid production and intracranial pressure in mice lacking choroid plexus water channel Aquaporin-1.," *FASEB J*, vol. 19, no. 1, pp. 76–8, Jan. 2005, doi: 10.1096/fj.04-1711fje.

[46] J. Wijnholds *et al.*, "Multidrug resistance protein 1 protects the choroid plexus epithelium and contributes to the blood-cerebrospinal fluid barrier.," *J Clin Invest*, vol. 105, no. 3, pp. 279–85, Feb. 2000, doi: 10.1172/JCI8267.

[47] R. B. Meeker, K. Williams, D. A. Killebrew, and L. C. Hudson, "Cell trafficking through the choroid plexus.," *Cell Adh Migr*, vol. 6, no. 5, pp. 390–6, 2012, doi: 10.4161/cam.21054.

[48] T. M. Liszczak, P. M. Black, A. Tzouras, L. Foley, and N. T. Zervas, "Morphological changes of the basilar artery, ventricles, and choroid plexus after experimental SAH.," *J Neurosurg*, vol. 61, no. 3, pp. 486–93, Sep. 1984, doi: 10.3171/jns.1984.61.3.0486.

[49] P. Zeni, E. Doepker, U. Schulze-Topphoff, S. Huewel, T. Tenenbaum, and H.-J. Galla, "MMPs contribute to TNF-alpha-induced alteration of the blood-cerebrospinal fluid barrier in vitro.," *Am J Physiol Cell Physiol*, vol. 293, no. 3, pp. C855-64, Sep. 2007, doi: 10.1152/ajpcell.00470.2006.

[50] J. K. Karimy *et al.*, "Inflammation-dependent cerebrospinal fluid hypersecretion by the choroid plexus epithelium in posthemorrhagic hydrocephalus.," *Nat Med*, vol. 23, no. 8, pp. 997–1003, Aug. 2017, doi: 10.1038/nm.4361.

[51] S. M. Robert *et al.*, "The choroid plexus links innate immunity to CSF dysregulation in hydrocephalus.," *Cell*, vol. 186, no. 4, pp. 764-785.e21, Feb. 2023, doi: 10.1016/j.cell.2023.01.017.

[52] Y. Béjot *et al.*, "Time-dependent contribution of non neuronal cells to BDNF production after ischemic stroke in rats.," *Neurochem Int*, vol. 58, no. 1, pp. 102–11, Jan. 2011, doi: 10.1016/j.neuint.2010.10.019.

[53] M. Ferrand-Drake, "Cell death in the choroid plexus following transient forebrain global ischemia in the rat.," *Microsc Res Tech*, vol. 52, no. 1, pp. 130–6, Jan. 2001, doi: 10.1002/1097-0029(20010101)52:1<130::AID-JEMT14>3.0.CO;2-6.

[54] N. Matsumoto *et al.*, "Transplantation of cultured choroid plexus epithelial cells via cerebrospinal fluid shows prominent neuroprotective effects against acute ischemic brain injury in the rat.," *Neurosci Lett*, vol. 469, no. 3, pp. 283–8, Jan. 2010, doi: 10.1016/j.neulet.2009.09.060.

[55] J. W. Prineas, J. D. E. Parratt, and P. D. Kirwan, "Fibrosis of the Choroid Plexus Filtration Membrane.," *J Neuropathol Exp Neurol*, vol. 75, no. 9, pp. 855–67, Sep. 2016, doi: 10.1093/jnen/nlw061.

[56] S. D. Mesquita *et al.*, "The choroid plexus transcriptome reveals changes in type I and II interferon responses in a mouse model of Alzheimer's disease.," *Brain Behav Immun*, vol. 49, pp. 280–92, Oct. 2015, doi: 10.1016/j.bbi.2015.06.008.

[57] M. Brkic *et al.*, "Amyloid β Oligomers Disrupt Blood-CSF Barrier Integrity by Activating Matrix Metalloproteinases.," *J Neurosci*, vol. 35, no. 37, pp. 12766–78, Sep. 2015, doi: 10.1523/JNEUROSCI.0006-15.2015.

[58] X. Alvira-Botero and E. M. Carro, "Clearance of amyloid-β peptide across the choroid plexus in Alzheimer's disease.," *Curr Aging Sci*, vol. 3, no. 3, pp. 219–29, Dec. 2010, doi: 10.2174/1874609811003030219.

[59] M. Bolos, D. Antequera, J. Aldudo, H. Kristen, M. J. Bullido, and E. Carro, "Choroid plexus implants rescue Alzheimer's disease-like pathologies by modulating amyloid-β degradation.," *Cell Mol Life Sci*, vol. 71, no. 15, pp. 2947–55, Aug. 2014, doi: 10.1007/s00018-013-1529-4.

[60] A. Junker, R. Hohlfeld, and E. Meinl, "The emerging role of microRNAs in multiple sclerosis.," *Nat Rev Neurol*, vol. 7, no. 1, pp. 56–9, Jan. 2011, doi: 10.1038/nrneurol.2010.179.

[61] L. Lafay-Cousin *et al.*, "Choroid plexus tumors in children less than 36 months: the Canadian Pediatric Brain Tumor Consortium (CPBTC) experience.," *Childs Nerv Syst*, vol. 27, no. 2, pp. 259–64, Feb. 2011, doi: 10.1007/s00381-010-1269-9.

[62] D. N. Louis *et al.*, "The 2007 WHO classification of tumours of the central nervous system.," *Acta Neuropathol*, vol. 114, no. 2, pp. 97–109, Aug. 2007, doi: 10.1007/s00401-007-0243-4.

[63] P. Gopal, J. R. Parker, R. Debski, and J. C. Parker, "Choroid plexus carcinoma.," *Arch Pathol Lab Med*, vol. 132, no. 8, pp. 1350–4, Aug. 2008, doi: 10.5858/2008-132-1350-CPC.

[64] International Society for Paediatric Neurosurgery, “Pathology of Supratentorial Choroid Plexus Tumors in Children,” Pathology of Supratentorial Choroid Plexus Tumors in Children.

[65] D. M. Cannon, P. Mohindra, V. Gondi, T. J. Kruser, and K. R. Kozak, “Choroid plexus tumor epidemiology and outcomes: implications for surgical and radiotherapeutic management.,” *J Neurooncol*, vol. 121, no. 1, pp. 151–7, Jan. 2015, doi: 10.1007/s11060-014-1616-x.

[66] A. Hosmann *et al.*, “Management of choroid plexus tumors—an institutional experience,” *Acta Neurochir (Wien)*, vol. 161, no. 4, pp. 745–754, Apr. 2019, doi: 10.1007/s00701-019-03832-5.

[67] J. E. Wolff *et al.*, “Final results of the Choroid Plexus Tumor study CPT-SIOP-2000.,” *J Neurooncol*, vol. 156, no. 3, pp. 599–613, Feb. 2022, doi: 10.1007/s11060-021-03942-0.

[68] M. J. Donovan, E. J. Yunis, U. DeGirolami, J. A. Fletcher, and D. E. Schofield, “Chromosome aberrations in choroid plexus papillomas.,” *Genes Chromosomes Cancer*, vol. 11, no. 4, pp. 267–70, Dec. 1994, doi: 10.1002/gcc.2870110410.

[69] Y. S. Li, Y.-S. Fan, and R. F. Armstrong, “Endoreduplication and telomeric association in a choroid plexus carcinoma,” *Cancer Genet Cytogenet*, vol. 87, no. 1, pp. 7–10, Mar. 1996, doi: 10.1016/0165-4608(95)00234-0.

[70] C. H. Rickert, O. D. Wiestler, and W. Paulus, “Chromosomal imbalances in choroid plexus tumors.,” *Am J Pathol*, vol. 160, no. 3, pp. 1105–13, Mar. 2002, doi: 10.1016/S0002-9440(10)64931-0.

[71] D. M. Merino *et al.*, “Molecular characterization of choroid plexus tumors reveals novel clinically relevant subgroups.,” *Clin Cancer Res*, vol. 21, no. 1, pp. 184–92, Jan. 2015, doi: 10.1158/1078-0432.CCR-14-1324.

[72] C. Thomas *et al.*, “The genetic landscape of choroid plexus tumors in children and adults.,” *Neuro Oncol*, vol. 23, no. 4, pp. 650–660, Apr. 2021, doi: 10.1093/neuonc/noaa267.

[73] U. Tabori *et al.*, “TP53 alterations determine clinical subgroups and survival of patients with choroid plexus tumors.,” *J Clin Oncol*, vol. 28, no. 12, pp. 1995–2001, Apr. 2010, doi: 10.1200/JCO.2009.26.8169.

[74] Y. Tong *et al.*, “Cross-Species Genomics Identifies TAF12, NFYC, and RAD54L as Choroid Plexus Carcinoma Oncogenes.,” *Cancer Cell*, vol. 27, no. 5, pp. 712–27, May 2015, doi: 10.1016/j.ccell.2015.04.005.

[75] L. Li *et al.*, "Sonic Hedgehog promotes proliferation of Notch-dependent monociliated choroid plexus tumour cells.," *Nat Cell Biol*, vol. 18, no. 4, pp. 418–30, Apr. 2016, doi: 10.1038/ncb3327.

[76] S. El Nagar *et al.*, "A new genetically engineered mouse model of choroid plexus carcinoma.," *Biochem Biophys Res Commun*, vol. 496, no. 2, pp. 568–574, Feb. 2018, doi: 10.1016/j.bbrc.2017.11.192.

[77] A. Merve *et al.*, "c-MYC overexpression induces choroid plexus papillomas through a T-cell mediated inflammatory mechanism," *Acta Neuropathol Commun*, vol. 7, no. 1, p. 95, Dec. 2019, doi: 10.1186/s40478-019-0739-x.

[78] M. L. Shannon *et al.*, "Mice Expressing Myc in Neural Precursors Develop Choroid Plexus and Ciliary Body Tumors.," *Am J Pathol*, vol. 188, no. 6, pp. 1334–1344, Jun. 2018, doi: 10.1016/j.ajpath.2018.02.009.

[79] J. Wang *et al.*, "Myc and Loss of p53 Cooperate to Drive Formation of Choroid Plexus Carcinoma.," *Cancer Res*, vol. 79, no. 9, pp. 2208–2219, May 2019, doi: 10.1158/0008-5472.CAN-18-2565.

[80] N. Spassky and A. Meunier, "The development and functions of multiciliated epithelia.," *Nat Rev Mol Cell Biol*, vol. 18, no. 7, pp. 423–436, Jul. 2017, doi: 10.1038/nrm.2017.21.

[81] J. F. Reiter and M. R. Leroux, "Genes and molecular pathways underpinning ciliopathies.," *Nat Rev Mol Cell Biol*, vol. 18, no. 9, pp. 533–547, Sep. 2017, doi: 10.1038/nrm.2017.60.

[82] K. Praveen, E. E. Davis, and N. Katsanis, "Unique among ciliopathies: primary ciliary dyskinesia, a motile cilia disorder.," *F1000Prime Rep*, vol. 7, p. 36, 2015, doi: 10.12703/P7-36.

[83] B. Banizs *et al.*, "Dysfunctional cilia lead to altered ependyma and choroid plexus function, and result in the formation of hydrocephalus.," *Development*, vol. 132, no. 23, pp. 5329–39, Dec. 2005, doi: 10.1242/dev.02153.

[84] K. Narita, T. Kawate, N. Kakinuma, and S. Takeda, "Multiple primary cilia modulate the fluid transcytosis in choroid plexus epithelium.," *Traffic*, vol. 11, no. 2, pp. 287–301, Feb. 2010, doi: 10.1111/j.1600-0854.2009.01016.x.

[85] C. Kyrousi *et al.*, "Mcidas and GemC1 are key regulators for the generation of multiciliated ependymal cells in the adult neurogenic niche.," *Development*, vol. 142, no. 21, pp. 3661–74, Nov. 2015, doi: 10.1242/dev.126342.

[86] L. Ma, I. Quigley, H. Omran, and C. Kintner, "Multicilin drives centriole biogenesis via E2f proteins.," *Genes Dev*, vol. 28, no. 13, pp. 1461–71, Jul. 2014, doi: 10.1101/gad.243832.114.

[87] C. B. Marshall *et al.*, "p73 Is Required for Multiciliogenesis and Regulates the Foxj1-Associated Gene Network.," *Cell Rep*, vol. 14, no. 10, pp. 2289–300, Mar. 2016, doi: 10.1016/j.celrep.2016.02.035.

[88] A. Al Jord, A.-I. Lemaître, N. Delgehyr, M. Faucourt, N. Spassky, and A. Meunier, "Centriole amplification by mother and daughter centrioles differs in multiciliated cells.," *Nature*, vol. 516, no. 7529, pp. 104–7, Dec. 2014, doi: 10.1038/nature13770.

[89] G. J. Dohrmann and P. C. Bucy, "Human choroid plexus: a light and electron microscopic study.," *J Neurosurg*, vol. 33, no. 5, pp. 506–16, Nov. 1970, doi: 10.3171/jns.1970.33.5.0506.

[90] D. A. Davis, B. J. Lloyd, and T. H. Milhorat, "A comparative ultrastructural study of the choroid plexuses of the immature pig.," *Anat Rec*, vol. 176, no. 4, pp. 443–54, Aug. 1973, doi: 10.1002/ar.1091760407.

[91] P. P. D'Gama *et al.*, "Diversity and function of motile ciliated cell types within ependymal lineages of the zebrafish brain.," *Cell Rep*, vol. 37, no. 1, p. 109775, Oct. 2021, doi: 10.1016/j.celrep.2021.109775.

[92] K. Narita *et al.*, "Proteomic analysis of multiple primary cilia reveals a novel mode of ciliary development in mammals.," *Biol Open*, vol. 1, no. 8, pp. 815–25, Aug. 2012, doi: 10.1242/bio.20121081.

[93] Y. Nonami, K. Narita, H. Nakamura, T. Inoue, and S. Takeda, "Developmental changes in ciliary motility on choroid plexus epithelial cells during the perinatal period.," *Cytoskeleton (Hoboken)*, vol. 70, no. 12, pp. 797–803, Dec. 2013, doi: 10.1002/cm.21132.

[94] J. R. Crawford and H. Isaacs, "Perinatal (fetal and neonatal) choroid plexus tumors: a review.," *Childs Nerv Syst*, vol. 35, no. 6, pp. 937–944, Jun. 2019, doi: 10.1007/s00381-019-04135-x.

[95] M. Filbin and M. Monje, "Developmental origins and emerging therapeutic opportunities for childhood cancer.," *Nat Med*, vol. 25, no. 3, pp. 367–376, Mar. 2019, doi: 10.1038/s41591-019-0383-9.

[96] Q. Li *et al.*, "Disruption of GMNC-MCIDAS multiciliogenesis program is critical in choroid plexus carcinoma development.," *Cell Death Differ*, vol. 29, no. 8, pp. 1596–1610, Aug. 2022, doi: 10.1038/s41418-022-00950-z.

[97] S. A. Basindwah, B. S. Alzahrani, A. M. Ajlan, and H. Alkhalidi, "Persistence of communicating hydrocephalus post choroid plexus tumor resection: Case reports and review of literature.," *Surg Neurol Int*, vol. 12, p. 483, 2021, doi: 10.25259/SNI_681_2021.

[98] Y. Li *et al.*, "Choroid plexus mast cells drive tumor-associated hydrocephalus.," *Cell*, vol. 186, no. 26, pp. 5719-5738.e28, Dec. 2023, doi: 10.1016/j.cell.2023.11.001.

[99] M. Hasselblatt *et al.*, "TWIST-1 is overexpressed in neoplastic choroid plexus epithelial cells and promotes proliferation and invasion.," *Cancer Res*, vol. 69, no. 6, pp. 2219–23, Mar. 2009, doi: 10.1158/0008-5472.CAN-08-3176.

[100] S. H. Tan and N. Barker, "Wnt Signaling in Adult Epithelial Stem Cells and Cancer.," *Prog Mol Biol Transl Sci*, vol. 153, pp. 21–79, Jan. 2018, doi: 10.1016/bs.pmbts.2017.11.017.

[101] L. Zhang, R. Ren, X. Yang, Y. Ge, X. Zhang, and H. Yuan, "Oncogenic role of early growth response-1 in liver cancer through the regulation of the microRNA-675/sestrin 3 and the Wnt/β-catenin signaling pathway.," *Bioengineered*, vol. 12, no. 1, pp. 5305–5322, Dec. 2021, doi: 10.1080/21655979.2021.1964889.

[102] L. Poggi, S. Casarosa, and M. Carl, "An Eye on the Wnt Inhibitory Factor Wif1.," *Front Cell Dev Biol*, vol. 6, p. 167, 2018, doi: 10.3389/fcell.2018.00167.

[103] ICGC/TCGA Pan-Cancer Analysis of Whole Genomes Consortium, "Pan-cancer analysis of whole genomes.," *Nature*, vol. 578, no. 7793, pp. 82–93, Feb. 2020, doi: 10.1038/s41586-020-1969-6.

[104] O. Symmons *et al.*, "Functional and topological characteristics of mammalian regulatory domains.," *Genome Res*, vol. 24, no. 3, pp. 390–400, Mar. 2014, doi: 10.1101/gr.163519.113.

[105] E. H. Z. Chua, S. Yasar, and N. Harmston, "The importance of considering regulatory domains in genome-wide analyses - the nearest gene is often wrong!," *Biol Open*, vol. 11, no. 4, Apr. 2022, doi: 10.1242/bio.059091.

[106] Y. Matsuno *et al.*, "Replication-stress-associated DSBs induced by ionizing radiation risk genomic destabilization and associated clonal evolution.," *iScience*, vol. 24, no. 4, p. 102313, Apr. 2021, doi: 10.1016/j.isci.2021.102313.

[107] Y. Matsuno, R. Kusumoto-Matsuo, Y. Manaka, H. Asai, and K. Yoshioka, "Echoed induction of nucleotide variants and chromosomal structural variants in cancer cells," *Sci Rep*, vol. 12, no. 1, p. 20964, Dec. 2022, doi: 10.1038/s41598-022-25479-6.

[108] S. Richards *et al.*, "Standards and guidelines for the interpretation of sequence variants: a joint consensus recommendation of the American College of Medical Genetics and Genomics and the Association for Molecular Pathology," *Genetics in Medicine*, vol. 17, no. 5, pp. 405–424, May 2015, doi: 10.1038/gim.2015.30.

[109] P. Horak *et al.*, "Standards for the classification of pathogenicity of somatic variants in cancer (oncogenicity): Joint recommendations of Clinical Genome Resource (ClinGen), Cancer Genomics Consortium (CGC), and Variant Interpretation for Cancer Consortium (VICC)," *Genetics in Medicine*, vol. 24, no. 5, pp. 986–998, May 2022, doi: 10.1016/j.gim.2022.01.001.

[110] S. Diederichs *et al.*, "The dark matter of the cancer genome: aberrations in regulatory elements, untranslated regions, splice sites, non-coding RNA and synonymous mutations.," *EMBO Mol Med*, vol. 8, no. 5, pp. 442–57, May 2016, doi: 10.15252/emmm.201506055.

[111] H. Jung, K. S. Lee, and J. K. Choi, "Comprehensive characterisation of intronic mis-splicing mutations in human cancers.," *Oncogene*, vol. 40, no. 7, pp. 1347–1361, Feb. 2021, doi: 10.1038/s41388-020-01614-3.

[112] Z. Zhao *et al.*, "Cancer-associated dynamics and potential regulators of intronic polyadenylation revealed by IPAFinder using standard RNA-seq data.," *Genome Res*, vol. 31, no. 11, pp. 2095–2106, Nov. 2021, doi: 10.1101/gr.271627.120.

[113] F. Chen, Y. Zhang, and C. J. Creighton, "Systematic identification of non-coding somatic single nucleotide variants associated with altered transcription and DNA methylation in adult and pediatric cancers.," *NAR Cancer*, vol. 3, no. 1, p. zcab001, Mar. 2021, doi: 10.1093/narcan/zcab001.

[114] S. N. Gröbner *et al.*, "The landscape of genomic alterations across childhood cancers.," *Nature*, vol. 555, no. 7696, pp. 321–327, Mar. 2018, doi: 10.1038/nature25480.

[115] K. J. Karczewski *et al.*, "The mutational constraint spectrum quantified from variation in 141,456 humans," *Nature*, vol. 581, no. 7809, pp. 434–443, May 2020, doi: 10.1038/s41586-020-2308-7.

[116] P. Rentzsch, D. Witten, G. M. Cooper, J. Shendure, and M. Kircher, "CADD: predicting the deleteriousness of variants throughout the human genome.," *Nucleic Acids Res*, vol. 47, no. D1, pp. D886–D894, Jan. 2019, doi: 10.1093/nar/gky1016.

[117] R. Nusse and H. Clevers, "Wnt/β-Catenin Signaling, Disease, and Emerging Therapeutic Modalities," *Cell*, vol. 169, no. 6, pp. 985–999, Jun. 2017, doi: 10.1016/j.cell.2017.05.016.

[118] M. Tomm *et al.*, "Role of Wnt inhibitory factor-1 and Wnt/wingless signaling in choroid plexus tumors.," *Pediatr Blood Cancer*, vol. 53, no. 6, pp. 1152–5, Dec. 2009, doi: 10.1002/pbc.22201.

[119] A. Nentwig, R. J. Higgins, T. Francey, M. Doherr, A. Zurbriggen, and A. Oevermann, "Aberrant E-cadherin, β-catenin, and glial fibrillary acidic protein (GFAP) expression in canine choroid plexus tumors.," *J Vet Diagn Invest*, vol. 24, no. 1, pp. 14–22, Jan. 2012, doi: 10.1177/1040638711425940.

[120] Y.-S. Jung and J.-I. Park, "Wnt signaling in cancer: therapeutic targeting of Wnt signaling beyond β-catenin and the destruction complex.," *Exp Mol Med*, vol. 52, no. 2, pp. 183–191, Feb. 2020, doi: 10.1038/s12276-020-0380-6.

[121] Y. Zhang, X. Liu, A. Li, and X. Tang, "A pan-cancer analysis on the carcinogenic effect of human adenomatous polyposis coli.," *PLoS One*, vol. 17, no. 3, p. e0265655, 2022, doi: 10.1371/journal.pone.0265655.

[122] W. Zheng and Q. Zhao, "Establishment and characterization of an immortalized Z310 choroidal epithelial cell line from murine choroid plexus.," *Brain Res*, vol. 958, no. 2, pp. 371–80, Dec. 2002, doi: 10.1016/s0006-8993(02)03683-1.

[123] S. Borowicz *et al.*, "The soft agar colony formation assay.," *J Vis Exp*, no. 92, p. e51998, Oct. 2014, doi: 10.3791/51998.

[124] T. Eisemann, B. Costa, J. Strelau, M. Mittelbronn, P. Angel, and H. Peterziel, "An advanced glioma cell invasion assay based on organotypic brain slice cultures," *BMC Cancer*, vol. 18, no. 1, p. 103, Dec. 2018, doi: 10.1186/s12885-018-4007-4.

[125] L. Pellegrini, C. Bonfio, J. Chadwick, F. Begum, M. Skehel, and M. A. Lancaster, "Human CNS barrier-forming organoids with cerebrospinal fluid production," *Science (1979)*, vol. 369, no. 6500, Jul. 2020, doi: 10.1126/science.aaz5626.

[126] S. M. Law and J. J. Zheng, "Premise and peril of Wnt signaling activation through GSK-3β inhibition.," *iScience*, vol. 25, no. 4, p. 104159, Apr. 2022, doi: 10.1016/j.isci.2022.104159.

[127] L. He, J. Wen, and Q. Dai, "PRDM16 functions as a co-repressor in the BMP pathway to suppress neural stem cell proliferation," *bioRxiv*, 2023.

[128] E. J. Choi, E. A. Sloma, and A. D. Miller, "Kir7.1 immunoreactivity in canine choroid plexus tumors.," *J Vet Diagn Invest*, vol. 28, no. 4, pp. 464–8, Jul. 2016, doi: 10.1177/1040638716650239.

[129] K. Tong *et al.*, "Degree of Tissue Differentiation Dictates Susceptibility to BRAF-Driven Colorectal Cancer," *Cell Rep*, vol. 21, no. 13, pp. 3833–3845, Dec. 2017, doi: 10.1016/j.celrep.2017.11.104.

[130] A. Jögi, M. Vaapil, M. Johansson, and S. Påhlman, "Cancer cell differentiation heterogeneity and aggressive behavior in solid tumors.," *Ups J Med Sci*, vol. 117, no. 2, pp. 217–24, May 2012, doi: 10.3109/03009734.2012.659294.

[131] S. Albrecht, E. Rouah, L. E. Becker, and J. Bruner, "Transthyretin immunoreactivity in choroid plexus neoplasms and brain metastases.," *Mod Pathol*, vol. 4, no. 5, pp. 610–4, Sep. 1991.

[132] M. Pienkowska *et al.*, "DNA methylation signature is prognostic of choroid plexus tumor aggressiveness.," *Clin Epigenetics*, vol. 11, no. 1, p. 117, Aug. 2019, doi: 10.1186/s13148-019-0708-z.

[133] M. V Hadjihannas, M. Brückner, B. Jerchow, W. Birchmeier, W. Dietmaier, and J. Behrens, "Aberrant Wnt/beta-catenin signaling can induce chromosomal instability in colon cancer.," *Proc Natl Acad Sci U S A*, vol. 103, no. 28, pp. 10747–52, Jul. 2006, doi: 10.1073/pnas.0604206103.

[134] R. Fodde *et al.*, "Mutations in the APC tumour suppressor gene cause chromosomal instability.," *Nat Cell Biol*, vol. 3, no. 4, pp. 433–8, Apr. 2001, doi: 10.1038/35070129.

[135] K. B. Kaplan, A. A. Burds, J. R. Swedlow, S. S. Bekir, P. K. Sorger, and I. S. Näthke, "A role for the Adenomatous Polyposis Coli protein in chromosome segregation.," *Nat Cell Biol*, vol. 3, no. 4, pp. 429–32, Apr. 2001, doi: 10.1038/35070123.

[136] W. Kim, M. Kim, and E. Jho, "Wnt/β-catenin signalling: from plasma membrane to nucleus.," *Biochem J*, vol. 450, no. 1, pp. 9–21, Feb. 2013, doi: 10.1042/BJ20121284.

[137] J. Chen *et al.*, "Fine Tuning of Canonical Wnt Stimulation Enhances Differentiation of Pluripotent Stem Cells Independent of β-Catenin-Mediated T-Cell Factor Signaling.," *Stem Cells*, vol. 36, no. 6, pp. 822–833, Jun. 2018, doi: 10.1002/stem.2794.

[138] M. Zhao, Y. Tang, Y. Zhou, and J. Zhang, "Deciphering Role of Wnt Signalling in Cardiac Mesoderm and Cardiomyocyte Differentiation from Human iPSCs: Four-dimensional control of Wnt pathway for hiPSC-CMs differentiation.," *Sci Rep*, vol. 9, no. 1, p. 19389, Dec. 2019, doi: 10.1038/s41598-019-55620-x.

[139] Z. Steinhart *et al.*, "Genome-wide CRISPR screens reveal a Wnt-FZD5 signaling circuit as a druggable vulnerability of RNF43-mutant pancreatic tumors.," *Nat Med*, vol. 23, no. 1, pp. 60–68, Jan. 2017, doi: 10.1038/nm.4219.

[140] R. Chidiac *et al.*, "A Norrin/Wnt surrogate antibody stimulates endothelial cell barrier function and rescues retinopathy.," *EMBO Mol Med*, vol. 13, no. 7, p. e13977, Jul. 2021, doi: 10.15252/emmm.202113977.

[141] M. Martin *et al.*, "Engineered Wnt ligands enable blood-brain barrier repair in neurological disorders.," *Science*, vol. 375, no. 6582, p. eabm4459, Feb. 2022, doi: 10.1126/science.abm4459.

[142] I. Ishiwata *et al.*, "Establishment and characterization of a human malignant choroids plexus papilloma cell line (HIBCPP).," *Hum Cell*, vol. 18, no. 1, pp. 67–72, Mar. 2005, doi: 10.1111/j.1749-0774.2005.tb00059.x.

[143] H. Yang, Y. Wang, P. Wang, N. Zhang, and P. Wang, "Tumor organoids for cancer research and personalized medicine.," *Cancer Biol Med*, vol. 19, no. 3, pp. 319–32, Sep. 2021, doi: 10.20892/j.issn.2095-3941.2021.0335.

[144] R. R. Sturrock, "A morphological study of the development of the mouse choroid plexus.," *J Anat*, vol. 129, no. Pt 4, pp. 777–93, Dec. 1979.

[145] I. Miller *et al.*, "Ki67 is a Graded Rather than a Binary Marker of Proliferation versus Quiescence.," *Cell Rep*, vol. 24, no. 5, pp. 1105-1112.e5, Jul. 2018, doi: 10.1016/j.celrep.2018.06.110.

[146] N. Delgehyr *et al.*, "Ependymal cell differentiation, from monociliated to multiciliated cells.," *Methods Cell Biol*, vol. 127, pp. 19–35, 2015, doi: 10.1016/bs.mcb.2015.01.004.

[147] Z. Mirzadeh, Y.-G. Han, M. Soriano-Navarro, J. M. García-Verdugo, and A. Alvarez-Buylla, "Cilia organize ependymal planar polarity.," *J Neurosci*, vol. 30, no. 7, pp. 2600–10, Feb. 2010, doi: 10.1523/JNEUROSCI.3744-09.2010.

[148] C. O'Callaghan, K. Sikand, and A. Rutman, "Respiratory and brain ependymal ciliary function.," *Pediatr Res*, vol. 46, no. 6, pp. 704–7, Dec. 1999, doi: 10.1203/00006450-199912000-00005.

[149] H. Ryu *et al.*, "The molecular dynamics of subdistal appendages in multi-ciliated cells," *Nat Commun*, vol. 12, no. 1, p. 612, Jan. 2021, doi: 10.1038/s41467-021-20902-4.

[150] V. B. Bystrevskaya, V. V Lichkun, A. S. Antonov, and N. A. Perov, "An ultrastructural study of centriolar complexes in adult and embryonic human aortic endothelial cells.," *Tissue Cell*, vol. 20, no. 4, pp. 493–503, 1988, doi: 10.1016/0040-8166(88)90052-3.

[151] M. Bosch Grau *et al.*, "Tubulin glycylases and glutamylases have distinct functions in stabilization and motility of ependymal cilia.," *J Cell Biol*, vol. 202, no. 3, pp. 441–51, Aug. 2013, doi: 10.1083/jcb.201305041.

[152] S. Gadadhar *et al.*, "Tubulin glycylation controls primary cilia length.," *J Cell Biol*, vol. 216, no. 9, pp. 2701–2713, Sep. 2017, doi: 10.1083/jcb.201612050.

[153] H. Olbrich *et al.*, "Loss-of-Function GAS8 Mutations Cause Primary Ciliary Dyskinesia and Disrupt the Nexin-Dynein Regulatory Complex.," *Am J Hum Genet*, vol. 97, no. 4, pp. 546–54, Oct. 2015, doi: 10.1016/j.ajhg.2015.08.012.

[154] T. Ide *et al.*, "CFAP53 regulates mammalian cilia-type motility patterns through differential localization and recruitment of axonemal dynein components.," *PLoS Genet*, vol. 16, no. 12, p. e1009232, Dec. 2020, doi: 10.1371/journal.pgen.1009232.

[155] B. Kurtulmus *et al.*, "LRRC45 contributes to early steps of axoneme extension.," *J Cell Sci*, vol. 131, no. 18, Sep. 2018, doi: 10.1242/jcs.223594.

[156] L. Wang and B. D. Dynlacht, "The regulation of cilium assembly and disassembly in development and disease.," *Development*, vol. 145, no. 18, Sep. 2018, doi: 10.1242/dev.151407.

[157] C. Janke and J. C. Bulinski, "Post-translational regulation of the microtubule cytoskeleton: mechanisms and functions.," *Nat Rev Mol Cell Biol*, vol. 12, no. 12, pp. 773–86, Nov. 2011, doi: 10.1038/nrm3227.

[158] C. Janke and M. Kneussel, "Tubulin post-translational modifications: encoding functions on the neuronal microtubule cytoskeleton.," *Trends Neurosci*, vol. 33, no. 8, pp. 362–72, Aug. 2010, doi: 10.1016/j.tins.2010.05.001.

[159] A. Wolff *et al.*, "Distribution of glutamylated alpha and beta-tubulin in mouse tissues using a specific monoclonal antibody, GT335.," *Eur J Cell Biol*, vol. 59, no. 2, pp. 425–32, Dec. 1992.

[160] K. Rogowski *et al.*, "A Family of Protein-Deglutamylating Enzymes Associated with Neurodegeneration," *Cell*, vol. 143, no. 4, pp. 564–578, Nov. 2010, doi: 10.1016/j.cell.2010.10.014.

[161] B. Lacroix *et al.*, "Tubulin polyglutamylation stimulates spastin-mediated microtubule severing.," *J Cell Biol*, vol. 189, no. 6, pp. 945–54, Jun. 2010, doi: 10.1083/jcb.201001024.

[162] M. L. Valenstein and A. Roll-Mecak, "Graded Control of Microtubule Severing by Tubulin Glutamylation.," *Cell*, vol. 164, no. 5, pp. 911–21, Feb. 2016, doi: 10.1016/j.cell.2016.01.019.

[163] M. S. Brill *et al.*, “Branch-Specific Microtubule Destabilization Mediates Axon Branch Loss during Neuromuscular Synapse Elimination.,” *Neuron*, vol. 92, no. 4, pp. 845–856, Nov. 2016, doi: 10.1016/j.neuron.2016.09.049.

[164] M. M. Magiera *et al.*, “Excessive tubulin polyglutamylation causes neurodegeneration and perturbs neuronal transport.,” *EMBO J*, vol. 37, no. 23, Dec. 2018, doi: 10.15252/embj.2018100440.

[165] K. Kunimoto *et al.*, “Coordinated ciliary beating requires Odf2-mediated polarization of basal bodies via basal feet.,” *Cell*, vol. 148, no. 1–2, pp. 189–200, Jan. 2012, doi: 10.1016/j.cell.2011.10.052.

[166] E. Herawati, D. Taniguchi, H. Kanoh, K. Tateishi, S. Ishihara, and S. Tsukita, “Multiciliated cell basal bodies align in stereotypical patterns coordinated by the apical cytoskeleton.,” *J Cell Biol*, vol. 214, no. 5, pp. 571–86, Aug. 2016, doi: 10.1083/jcb.201601023.

[167] D. F. Galati, B. J. Mitchell, and C. G. Pearson, “Subdistal Appendages Stabilize the Ups and Downs of Ciliary Life.,” *Dev Cell*, vol. 39, no. 4, pp. 387–389, Nov. 2016, doi: 10.1016/j.devcel.2016.11.006.

[168] G. Mazo, N. Soplop, W.-J. Wang, K. Uryu, and M. F. B. Tsou, “Spatial Control of Primary Ciliogenesis by Subdistal Appendages Alters Sensation-Associated Properties of Cilia.,” *Dev Cell*, vol. 39, no. 4, pp. 424–437, Nov. 2016, doi: 10.1016/j.devcel.2016.10.006.

[169] M. Mönnich *et al.*, “CEP128 Localizes to the Subdistal Appendages of the Mother Centriole and Regulates TGF-β/BMP Signaling at the Primary Cilium.,” *Cell Rep*, vol. 22, no. 10, pp. 2584–2592, Mar. 2018, doi: 10.1016/j.celrep.2018.02.043.

[170] Z. Liu *et al.*, “Super-Resolution Microscopy and FIB-SEM Imaging Reveal Parental Centriole-Derived, Hybrid Cilium in Mammalian Multiciliated Cells.,” *Dev Cell*, vol. 55, no. 2, pp. 224-236.e6, Oct. 2020, doi: 10.1016/j.devcel.2020.09.016.

[171] T. M. Vinogradova, E. E. Balashova, V. N. Smirnov, and V. B. Bystrevskaya, “Detection of the centriole tyr- or acet-tubulin changes in endothelial cells treated with thrombin using microscopic immunocytochemistry.,” *Cell Motil Cytoskeleton*, vol. 62, no. 1, pp. 1–12, Sep. 2005, doi: 10.1002/cm.20079.

[172] Q. Liu, G. Zhang, Z. Ji, and H. Lin, “Molecular and cellular mechanisms of spastin in neural development and disease (Review).,” *Int J Mol Med*, vol. 48, no. 6, Dec. 2021, doi: 10.3892/ijmm.2021.5051.

[173] R. Nanjundappa *et al.*, “Regulation of cilia abundance in multiciliated cells.,” *Elife*, vol. 8, Apr. 2019, doi: 10.7554/eLife.44039.

[174] S. Nonaka *et al.*, "Randomization of left-right asymmetry due to loss of nodal cilia generating leftward flow of extraembryonic fluid in mice lacking KIF3B motor protein.," *Cell*, vol. 95, no. 6, pp. 829–37, Dec. 1998, doi: 10.1016/s0092-8674(00)81705-5.

[175] Y. Okada, S. Takeda, Y. Tanaka, J.-C. I. Belmonte, and N. Hirokawa, "Mechanism of nodal flow: a conserved symmetry breaking event in left-right axis determination.," *Cell*, vol. 121, no. 4, pp. 633–644, May 2005, doi: 10.1016/j.cell.2005.04.008.

[176] M. C. Corballis, "Early signs of brain asymmetry.," *Trends Cogn Sci*, vol. 17, no. 11, pp. 554–5, Nov. 2013, doi: 10.1016/j.tics.2013.09.008.

[177] C. G. F. de Kovel, S. N. Lisgo, S. E. Fisher, and C. Francks, "Subtle left-right asymmetry of gene expression profiles in embryonic and foetal human brains," *Sci Rep*, vol. 8, no. 1, p. 12606, Sep. 2018, doi: 10.1038/s41598-018-29496-2.

[178] J. Schmitz, O. Güntürkün, and S. Ocklenburg, "Building an Asymmetrical Brain: The Molecular Perspective.," *Front Psychol*, vol. 10, p. 982, 2019, doi: 10.3389/fpsyg.2019.00982.

[179] G. Wheway, L. Nazlamova, and J. T. Hancock, "Signaling through the Primary Cilium," *Front Cell Dev Biol*, vol. 6, Feb. 2018, doi: 10.3389/fcell.2018.00008.

[180] K. H. Lee, "Involvement of Wnt signaling in primary cilia assembly and disassembly," *FEBS J*, vol. 287, no. 23, pp. 5027–5038, Dec. 2020, doi: 10.1111/febs.15579.

[181] M.-L. Kyun *et al.*, "Wnt3a Stimulation Promotes Primary Ciliogenesis through β-Catenin Phosphorylation-Induced Reorganization of Centriolar Satellites," *Cell Rep*, vol. 30, no. 5, pp. 1447-1462.e5, Feb. 2020, doi: 10.1016/j.celrep.2020.01.019.

[182] O. Bernatik, P. Paclikova, A. Kotrbova, V. Bryja, and L. Cajanek, "Primary Cilia Formation Does Not Rely on WNT/β-Catenin Signaling.," *Front Cell Dev Biol*, vol. 9, p. 623753, 2021, doi: 10.3389/fcell.2021.623753.

[183] L. T. Vuong and M. Mlodzik, "The complex relationship of Wnt-signaling pathways and cilia," 2023, pp. 95–125. doi: 10.1016/bs.ctdb.2023.09.002.

[184] S. K. Ghosh, S. P. Perrine, R. M. Williams, and D. V Faller, "Histone deacetylase inhibitors are potent inducers of gene expression in latent EBV and sensitize lymphoma cells to nucleoside antiviral agents.," *Blood*, vol. 119, no. 4, pp. 1008–17, Jan. 2012, doi: 10.1182/blood-2011-06-362434.

[185] M. Zhang, J. Shi, Y. Huang, and L. Lai, "Expression of canonical WNT/β-CATENIN signaling components in the developing human lung.," *BMC Dev Biol*, vol. 12, p. 21, Jul. 2012, doi: 10.1186/1471-213X-12-21.

[186] M. Haneda *et al.*, "Depletion of aquaporin 1 decreased ADAMTS-4 expression in human chondrocytes.," *Mol Med Rep*, vol. 17, no. 4, pp. 4874–4882, Apr. 2018, doi: 10.3892/mmr.2018.8545.

[187] D. Kusumoto *et al.*, "Automated Deep Learning-Based System to Identify Endothelial Cells Derived from Induced Pluripotent Stem Cells.," *Stem Cell Reports*, vol. 10, no. 6, pp. 1687–1695, Jun. 2018, doi: 10.1016/j.stemcr.2018.04.007.

[188] X. Wang, A. Spandidos, H. Wang, and B. Seed, "PrimerBank: a PCR primer database for quantitative gene expression analysis, 2012 update.," *Nucleic Acids Res*, vol. 40, no. Database issue, pp. D1144-9, Jan. 2012, doi: 10.1093/nar/gkr1013.

[189] L. C. Biggs *et al.*, "Hair follicle dermal condensation forms via Fgf20 primed cell cycle exit, cell motility, and aggregation.," *Elife*, vol. 7, Jul. 2018, doi: 10.7554/eLife.36468.

[190] K. Lu *et al.*, "Depressive patient-derived GABA interneurons reveal abnormal neural activity associated with HTR2C.," *EMBO Mol Med*, vol. 15, no. 1, p. e16364, Jan. 2023, doi: 10.15252/emmm.202216364.

[191] N. Kumar, R. Basundra, and S. Maiti, "Elevated polyamines induce c-MYC overexpression by perturbing quadruplex-WC duplex equilibrium.," *Nucleic Acids Res*, vol. 37, no. 10, pp. 3321–31, Jun. 2009, doi: 10.1093/nar/gkp196.

[192] J. Tratwal, B. Follin, A. Ekblond, J. Kastrup, and M. Haack-Sørensen, "Identification of a common reference gene pair for qPCR in human mesenchymal stromal cells from different tissue sources treated with VEGF.," *BMC Mol Biol*, vol. 15, p. 11, May 2014, doi: 10.1186/1471-2199-15-11.

[193] K. H. Ho and A. Patrizi, "Assessment of common housekeeping genes as reference for gene expression studies using RT-qPCR in mouse choroid plexus.," *Sci Rep*, vol. 11, no. 1, p. 3278, Feb. 2021, doi: 10.1038/s41598-021-82800-5.

[194] C. Valle *et al.*, "Tissue-specific deregulation of selected HDACs characterizes ALS progression in mouse models: pharmacological characterization of SIRT1 and SIRT2 pathways.," *Cell Death Dis*, vol. 5, no. 6, p. e1296, Jun. 2014, doi: 10.1038/cddis.2014.247.

[195] N. Fossat *et al.*, "A new GFP-tagged line reveals unexpected Otx2 protein localization in retinal photoreceptors.," *BMC Dev Biol*, vol. 7, p. 122, Nov. 2007, doi: 10.1186/1471-213X-7-122.

[196] H. Higginbotham, S. Bielas, T. Tanaka, and J. G. Gleeson, "Transgenic Mouse Line with Green-fluorescent Protein-labeled Centrin 2 allows Visualization of the Centrosome in Living Cells," *Transgenic Res*, vol. 13, no. 2, pp. 155–164, Apr. 2004, doi: 10.1023/B:TRAG.0000026071.41735.8e.

[197] O. Podgorny, N. Peunova, J.-H. Park, and G. Enikolopov, "Triple S-Phase Labeling of Dividing Stem Cells.," *Stem Cell Reports*, vol. 10, no. 2, pp. 615–626, Feb. 2018, doi: 10.1016/j.stemcr.2017.12.020.

[198] F. Heigwer, G. Kerr, and M. Boutros, "E-CRISP: fast CRISPR target site identification.," *Nat Methods*, vol. 11, no. 2, pp. 122–3, Feb. 2014, doi: 10.1038/nmeth.2812.

[199] O. Shalem *et al.*, "Genome-scale CRISPR-Cas9 knockout screening in human cells.," *Science*, vol. 343, no. 6166, pp. 84–87, Jan. 2014, doi: 10.1126/science.1247005.

[200] A. Jabali *et al.*, "Human cerebral organoids reveal progenitor pathology in EML1-linked cortical malformation.," *EMBO Rep*, vol. 23, no. 5, p. e54027, May 2022, doi: 10.15252/embr.202154027.

[201] J. M. Ruijter *et al.*, "Amplification efficiency: linking baseline and bias in the analysis of quantitative PCR data.," *Nucleic Acids Res*, vol. 37, no. 6, p. e45, Apr. 2009, doi: 10.1093/nar/gkp045.

[202] M. W. Pfaffl, "A new mathematical model for relative quantification in real-time RT-PCR.," *Nucleic Acids Res*, vol. 29, no. 9, p. e45, May 2001, doi: 10.1093/nar/29.9.e45.

[203] G. Ortiz-Álvarez *et al.*, "Adult Neural Stem Cells and Multiciliated Ependymal Cells Share a Common Lineage Regulated by the Geminin Family Members.," *Neuron*, vol. 102, no. 1, pp. 159-172.e7, Apr. 2019, doi: 10.1016/j.neuron.2019.01.051.

[204] D. Sage, F. R. Neumann, F. Hediger, S. M. Gasser, and M. Unser, "Automatic tracking of individual fluorescence particles: application to the study of chromosome dynamics.," *IEEE Trans Image Process*, vol. 14, no. 9, pp. 1372–83, Sep. 2005, doi: 10.1109/tip.2005.852787.

[205] E. Laruelle, N. Spassky, and A. Genovesio, "Unraveling spatial cellular pattern by computational tissue shuffling," *Commun Biol*, vol. 3, no. 1, p. 605, Oct. 2020, doi: 10.1038/s42003-020-01323-3.

[206] J. Schindelin *et al.*, "Fiji: an open-source platform for biological-image analysis.," *Nat Methods*, vol. 9, no. 7, pp. 676–82, Jun. 2012, doi: 10.1038/nmeth.2019.

[207] J. R. Kremer, D. N. Mastronarde, and J. R. McIntosh, “Computer visualization of three-dimensional image data using IMOD.,” *J Struct Biol*, vol. 116, no. 1, pp. 71–6, 1996, doi: 10.1006/jsbi.1996.0013.

[208] M. Hampf and M. Gossen, “A protocol for combined Photinus and Renilla luciferase quantification compatible with protein assays.,” *Anal Biochem*, vol. 356, no. 1, pp. 94–9, Sep. 2006, doi: 10.1016/j.ab.2006.04.046.

[209] W. McLaren *et al.*, “The Ensembl Variant Effect Predictor,” *Genome Biol*, vol. 17, no. 1, p. 122, Dec. 2016, doi: 10.1186/s13059-016-0974-4.

Oral and poster presentations

ORAL PRESENTATIONS

- **Ho, K.H.,** Jabali, A., …, Patrizi, A., The constitutive activation of Wnt/β-catenin initiates Choroid plexus tumors. *Interdisciplinary Center for Neurosciences IZN seminar series*; Feb 2023; Heidelberg, Germany

- **Ho, K.H.,** Salio, C., D'Este, E., ..., Patrizi, A. The biogenesis and maintenance of Choroid plexus' atypical cilia. *EMBO Workshop Cilia*; October 2022; Cologne, Germany

- **Ho, K.H.,** Anna-Lena Schramm, Patrizi, A., Mapping Choroid plexus development and its ciliogenesis. *Interdisciplinary Center for Neurosciences IZN seminar series*; Nov 2020; Heidelberg, Germany

POSTERS

- **Ho, K.H.,** Jabali, A., …, Patrizi, A., The constitutive activation of Wnt/β-catenin initiates Choroid plexus tumors. *PostdoCaRe Europe conference: Shaping the cancer research of tomorrow*; Oct 2023; Heidelberg, Germany

- **Ho, K.H.,** Jabali, A., …, Patrizi, A., The constitutive activation of Wnt/β-catenin initiates Choroid plexus tumors. *FSP-A Retreat*; Apr 2023; Kloster Schöntal, Germany

- **Ho, K.H.,** Scarpetta, V, ..., Patrizi, A. The atypical cilia of choroid plexus through developmental lenses. *Federation of European Neuroscience Societies (FENS) Conference*; July 2022; Paris, France

- **Ho, K.H.,** Hill, A., Silva, F., Schramm, A., Huber, J., …, Schwerk, C., Patrizi, A. Canonical Wnt signaling in the pathogenesis and treatment of Choroid plexus tumor. *DKFZ PhD Poster presentation round*; Nov 2021; Heidelberg, Germany

Upcoming conference

- **Ho, K.H.,** Jabali, A., …, Patrizi, A., The constitutive activation of Wnt/β-catenin initiates Choroid plexus tumors. *Brain Tumor Meeting 2024*; May 2024; Berlin, Germany

List of publications

The following manuscripts/publications are generated during my PhD studies

Ho, K. H., Trapp, M., Guida, C., Ivanova, E., Jabali, A., Thomas, C., Salasova, A., Bernatik, O., Salio, C., Horschitz, S., Hasselblatt, M., Sassoe-Pognetto, M., Cajanek, L., Ishikawa, H., Schroten, H., Schwerk, C., Acebron, S., Angel, P., Koch, P., Patrizi, A. (2023) Activation of Wnt/β-catenin signaling is critical for the oncogenesis of choroid plexus tumors. *Under revision at Neuro-Oncology.*

Ho, K. H., Candat, A., Scarpetta, V., Faucourt, M., Weill, S., Salio, C., D'Este, E., Meschkat, M., Wurm, C. A., Kneussel, M., Janke, C., Magiera, M. M., Genovesio, A., Meunier, A., Sassoè-Pognetto, M., Brill, M. S., Spassky, N., & Patrizi, A. (2023). Choroid plexuses carry nodal-like cilia that undergo axoneme regression from early adult stage*. Developmental Cell*, 58(23), 2641-2651.e6. https://doi.org/10.1016/j.devcel.2023.10.003

Ho, K. H., & Patrizi, A. (2021). Assessment of common housekeeping genes as reference for gene expression studies using RT-qPCR in mouse choroid plexus. *Scientific Reports*, 11(1). https://doi.org/10.1038/s41598-021-82800-5

Acknowledgement

I would like to express my deepest gratitude to everyone who has accompanied and supported me along the path of my PhD journey.

First and foremost, I would like to thank Dr. Annarita Patrizi for providing me with the opportunity to be part of the group and to contribute to these projects. Thank you for engaging in scientific discussions, offering advice and guidance, and providing prompt and earnest support for both my scientific and career development. I also appreciate your trust in my decisions and ability and give me the freedom to learn and develop, both myself and the projects, into the directions I am interested in.

I would also like to thank my TAC members, Prof. Dr. Gudrun Rappold and Prof. Dr. Oliver Stegle for your constructive feedbacks in the TAC meetings along my PhD. I would additionally like to thank Prof. Dr. Sergio P. Acebrón for chairing my defense committee.

I would like to thank many of the lab's collaborators for their valuable work and feedback into my projects: Dr. Nathalie Spassky, Dr. Nathalie Jurisch-Yaksi, Dr. Christian Thomas, Dr. Monika S. Brill, Dr. Sergio P. Acebrón, Dr. Chiara Salio, Dr. Ekaterina Ivanova, Dr. Maria M. Magiera, Dr. Rene Jackstadt, Dr. Ammar Jabali and Guida Catello.

I thank the Chica and Heinz Schaller Foundation and the Cancer-TRAX PhD-to-Postdoc Program at the German Cancer Research Center (DKFZ) – Weizmann Institute of Science for the much-needed financial support to the projects.

I thank the Core Facility and their staff for the great service and support: the Light Microscopy Core facility at DKFZ, particularly Dr. Krunic Damir; the Interdisciplinary Neurobehavioral Core (INBC) at Heidelberg University and the DKFZ animal facility; the DKFZ Genomics and Proteomics Core Facility; the Omics IT and Data Management core facility at the DKFZ; the Flow Cytometry core facility at the DKFZ and at Medical Faculty Mannheim, Heidelberg University, especially Stefanie Uhlig.

A huge thank to all the current and former members of the Patrizi lab for all your helps, support and company, both inside and outside the lab. A special thank to: Marleen Trapp, Valentina Scarpetta, Anna-Lena Schramm, Johanna Huber, Franziska Hertel, Alina Rißberger and Nico Burmistrak for your direct support to the projects; thank Dr. Anthony Hill for your advice on data analysis and your feedback on many of my writings; thank

Katrin Hakenesch for all your administrative support and, together with Nada Abdelgawad, for being the best office companions.

Beyond the lab, I would like to thank Barbara Lasut-Syszka, Chloe Tang, Gordon Haltenhof, Sylvia Mahara, Vien Quang Tri Ho, Bao Tram Tran and Thanh Hoa Nguyen for being the most supportive friends I could have during my PhD. Thank you for all your help and advice, all the trips, venting sessions, fun gatherings and good laughs together.

Thank you, Patrick, for walking with me the last part of this journey. Thank you for being so understanding and supportive and for brightening some of the dark days during this crazy time. Look forward to many more journeys with you in the future.

I would also like to thank countless numbers of scientists and colleagues who kindly provided small but valuable help and support throughout my PhD: sharing some missing reagents, recognition and input at posters/presentations, advice on troubleshooting experiments, feedback on CV and cover letter, debugging codes, etc. Thank you for offering help despite being strangers and not receiving anything back. It is wonderful to be surrounded by such community.

Finally, I would like to thank my Mom and my sister for always believing in and supporting me and my decisions. Thank you for all your hard work so that I can pursue my dreams. You are one of the biggest motivations for all my effort.